Grid-Connected Photovoltaic with Supercapacitor Energy Storage System Emulation and Reactive Power Allocation based on Transactive Energy Approach

A Dissertation Presented for the

Doctor of Philosophy

Degree

The University of Tennessee, Knoxville

Paychuda Kritprajun

December 2024

Copyright © 2024 by Paychuda Kritprajun
All rights reserved.

Acknowledgments

I would like to express my deepest gratitude to my advisor Dr. Leon M. Tolbert, for his support, guidance, and encouragement throughout my Ph.D. journey. I have received a lot of advice not only on technical parts but also on personal and professional development. His kindness has motivated me to help others whenever possible.

I would like to express my sincere gratitude to Dr. Yunting Liu for her support and suggestions, both in research and personal life. I am very grateful for her willingness to offer guidance throughout my Ph.D. studies and assistance with any challenges I encounter.

I would like to thank Dr. Hua (Kevin) Bai and Dr. Fangxing (Fran) Li for their kind suggestions regarding my research and their willingness to serve on my Ph.D. committees.

I also would like to thank my undergraduate advisors, Dr. Surin Khomfoi and Dr. Warachart Suwan-ngam. Without their support, my journey at UTK might not have been possible.

I am very grateful to all my colleagues at UTK for their assistance and support, both technically and emotionally. I would like to give special thanks to Dr. Nattapat Praisuwanna, Ms. Elizabeth Sutton, Ms. Niu Jia, Dr. Shiyuan Fan, Dr. Dingrui Li, Dr. Jiaojiao (Jenny) Dong, Ms. Mariana Espinola, Dr. Joshua Hambrick, Dr. Jingjing Sun, Dr. Shuyao Wang, Dr. Le (Emma) Kong, Mr. Ben Dean, Mr. Peter Pham, and Dr. Venkata Raghavendra. Also Thanks to all the colleges, staff, and alumni at UTK, including but not limited to Dr. Yang Huang, Dr. Yu Yan, Dr. Liang Qiao, Dr. Liyan Zhu, Dr. Yiwei Ma, Dr. Lin Zhu, Ms. Taylor Short, Mr. Xingxuan Tian, Ms. Sadia Sohid, Dr. Maximiliano Ferrari, Mr. Mohamed Al-Sager, Mr. Yousef Alamri, Ms. Min Lin, Mr. Haoyuan Sun, Ms. Rui Zhou, Dr. Jingxin Wang, Mr. Tino Liu, and Mr. Jimmy Yang.

I also would like to thank all Thai friends for their friendships and support, including Dr. Pattarawan Miller, Dr. Phattananawee Nalaoh, Ms. Sarita Rattanakunuprakarn, and Ms. Varissara Tanakom. I also would like to give my special thanks to all my best friends in Thailand who have consistently supported me throughout my time in the US, including Dr. Thapanan Janyalikit, Mr. Suravut Aonjaiaow, Mr. Jukkrit Jiraprasertwong, Mr. Burin Sapsiri, Mr. Danai Ponchalee Mr. Pitipol Autravisittikul, Ms. Rinlita Thanasutthijirapong, Ms. Nopparat Apichatsiritham, and Mr. Auttapol Wattanasakornkul.

Finally, I would like to express my gratitude to my family: my mom, Tanomsri Kritprajun; my sister, Kanyanan Kritprajun; and my dad, Naris Kritprajun. Thank you for always believing in me and supporting me in everything I do. I also would like to thank my husband, Mr. Daniel Merced, for his kindness, unlimited support, and encouragement throughout my Ph.D. journey. Thank you for always being there for me through thick and thin.

This dissertation made use of the Engineering Research Center Shared Facilities supported by the Engineering Research Center Program of the National Science Foundation and the Department of Energy under NSF Award Number EEC-1041877 and the CURENT Industry Partnership Program.

Abstract

The penetration of photovoltaic (PV) generations has rapidly increased in today's power systems. The high integration of PV systems into power grids has brought challenges in terms of grid resiliency and reliability.

One solution to enable the high integration of PV systems in power grids is the use of energy storage systems (ESSs). The ESSs act as energy buffers of PV systems by storing excess energy and later using it to maintain power balance in the power systems. Supercapacitors (SCs) are one promising energy storage technology for grid applications. SCs can be employed with PV systems to smooth power fluctuations generated by PV systems, thereby, reducing voltage fluctuations on power grids.

Studying SC dynamics in power systems can be challenging due to the difficulty in maintaining the consistency of physical SCs during tests. Therefore, this dissertation investigates SC dynamics in PV systems by developing a grid-connected PV with SC system (PVSS) emulator, which serves power system studies on a hardware testbed (HTB) platform. The PVSS emulator's accuracy is verified by comparing it to MATLAB/Simulink simulation results.

The PVSS emulator incorporates grid support functions, including voltage support, frequency support and inertia emulation, and fault ride-through operations (FRT). During FRT operation, when the PVSS stability is most vulnerable, a state of charge (SOC) reservation concept is proposed to ensure the SC's availability to provide FRT operations that comply with grid code requirements. Additionally, a SOC management control strategy is proposed to quickly restore the SC's SOC to its working region after FRT operations while ensuring the safe operations of both grid and PVSS. The performances of the proposed control strategies are validated on the HTB.

Finally, this dissertation investigates reactive power support from PV systems to improve voltage in power grids based on a transactive energy (TE) approach. The concept of considering the location of PV systems as reactive power suppliers is proposed for the TE approach to reduce losses in the power system caused by supplying reactive power over long distances. The proposed modified reactive power supply curve is validated to demonstrate its efficiency using an IEEE standard test feeder.

Table of Contents

Chapter 1 Introduction 1

1.1 Background and Motivation 1

1.2 Objectives 6

1.3 Dissertation Outline 6

Chapter 2 Literature Review 8

2.1 Overview of Supercapacitors (SCs) 8

2.1.1 SC Technologies 8

2.1.2 SC Applications in PV Systems 9

2.1.3 Modelling of SCs in Power System Study 12

2.2 Grid Ancillary Services 15

2.2.1 Frequency Support and Inertia Emulation 16

2.2.2 Voltage Support 18

2.2.3 Fault Ride-Through (FRT) Operation 18

2.3 Hardware Testbed Platform for Power System Study 21

2.4 State of Charge (SOC) 26

2.4.1 SOC Management for Grid Ancillary Services 26

2.4.2 Power Reference during SOC Management 28

2.5 Transactive Energy (TE) Approach 29

2.5.1 Reactive Power Support Based on the TE Approach 29

2.5.2 Reactive Power Supply Curve 30

2.5.3 Market Mechanism based on TE Approach 33

2.6 Summary 33

Chapter 3 Power Emulator of a Grid-Connected PV with SC System (PVSS) on HTB Platform 36

3.1 PVSS Average Model and Control 36

3.1.1 SC Subsystem 36

3.1.2 PV Subsystem 42

3.1.3 Grid-Connected Inverter Subsystem 44

3.2 PVSS Emulator 48
3.2.1 Discrete Model of PVSS Emulator 49
3.3 Experimental Verification 51
3.3.1 PVSS Emulator Setup on HTB 51
3.3.2 Experimental Results 54
3.4 Conclusions 68
Chapter 4 State of Charge Management for Grid-Connected PV with SC System Considering LVRT Operation 69
4.1 SOC Management Considering LVRT Operation 69
4.1.1 SOC Reservation Concept for LVRT Operation 70
4.1.2 SOC Management Considering Grid Conditions 71
4.1.3 Current Adjustment Based on SC Temperature 73
4.2 Experiments of SOC Management Considering LVRT Operation 80
4.2.1 SC Thermal Model of the PVSS Emulator 80
4.2.2 Experimental Results of SOC Reservation Concept 82
4.2.3 Experimental Results of SC Current Adjustment Based on SC Thermal Model ..87
4.2.4 Experimental Results of Adjusting Power during SOC Management based on Grid Conditions 87
4.3 Conclusions 89
Chapter 5 Reactive Power Allocation of Distributed Energy Resources (DERs) for Voltage Support Based on Transactive Energy (TE) Approach 92
5.1 Engaging Transactive Energy (TE) Approach to Reactive Power Support 92
5.2 Voltage Sensitivity Analysis for Reactive Power Support 95
5.3 Transactive Energy Approach Considering DER's Location 96
5.3.1 Impact of DER's Location on TE 97
5.3.2 Impact of DER's Reactive Power Capacity on TE 97
5.4 Simulation Verification 99
5.4.1 15-Node Test Feeder 99
5.4.2 IEEE-123 Test Feeder 102
5.4.3 Comparison of Reactive Power Dispatch Methods 109
5.5 Conclusions 117

Chapter 6 Linear Quadratic Regulator-based Controller for Control Mode Switching Under Fault Operation of PVSS 118
6.1 Control Mode Switching of PVSS when SC is Unavailable 120
6.2 Linear Quadratic Regulator (LQR) for Control Switching 120
6.2.1 Requirement of LQR Compensator 121
6.2.2 LQR-Based DC-LINK Voltage Control of PVSS 123
6.2.3 Design of LQR-based Controller 123
6.2.4 Selection of LQR Control Parameter by Optimization 125
6.3 Experiment of LQR Control of PVSS in HTB 126
6.3.1 PVSS Dynamics during the LVRT Event 126
6.3.2 Performance Evaluation of LQR-Based DC-Link Voltage Control 128
6.4 Conclusion 133
Chapter 7 Fast Frequency Support and Fast Frequency Recovery provided by PVSS 135
7.1 Impact of High Inertia Coefficient 135
7.2 Proposed Control for Fast Frequency Support including Fast Frequency Recovery .. 136
7.3 Experimental Results 137
7.3.1 Experimental Results of Adjustment of Inertia Coefficient on HTB 137
7.3.2 Experimental Results of Improvement of Frequency Recovery Service on HTB 145
7.3.3 Impact of SC's SOC on Fast Frequency Support provided by PVSS 152
7.4 Conclusion 155
Chapter 8 Conclusion and Future Work 156
8.1 Summary 156
8.2 Contributions 158
8.3 Future Works 159
8.3.1 Development of Hybrid SC Model on HTB 159
8.3.2 Grid Support Services Considering SC's SOC 159
References 161
Vita 173

List of Tables

Table 2.1: Performance Comparison of Different Types of SCs [25]. 10
Table 3.1: Zubieta SC model Parameters [46]. 39
Table 3.2: PVSS's Emulator Parameters. 53
Table 3.3: RC series SC model Parameters [46]. 63
Table 4.1: SC Thermal Parameters [93], [94], [96]. 79
Table 5.1: Parameters of 15-Node Test Feeder. 101
Table 5.2: Reactive Power Dispatch on 15-node Test Feeder. 103
Table 5.3: Parameters of DERs based on Scenarios. 106
Table 5.4: Power Losses in the IEEE-123 Node Test Feeder based on Reactive Power Dispatch Methods. 116
Table 6.1: DC-link Overvoltage during the Control Mode Transition at Different PV Operations. 131
Table 6.2: DC-link Overvoltage during the Control Mode Transition at Different Levels of Voltage Sag. 134

List of Figures

Figure 1.1: Total installed capacity in gigawatts (GW) of all generation in 2022 and the projected capacity for the year 2050 [2]. 2
Figure 1.2: Power grid's status of current synchronous generators dominant power grid (left) and IBRs dominant power grid (right) [1]. 2
Figure 1.3: Research publications related to SCs based on their applications [6]. 4
Figure 1.4: Qualitative comparison between energy storage technologies [11]. 4
Figure 2.1: Typical SC configuration for PV applications. (a) The SC system is connected at the DC-link of the PV system [8], [13] and (b) The SC system is connected to the PCC [29], [30], [34]..... 13
Figure 2.2: Common RC circuits used to represent the models of a supercapacitor cell [16], [17], [46]. (a) RC model, (b) Stern model, (c)Transmission line model, and (d) Zubieta model..... 14
Figure 2.3: Frequency control time frames [49], [50]. 17
Figure 2.4: Typical active power-frequency droop curve [18]. 17
Figure 2.5: Reactive power capability curve of ES DERs [50]. 19
Figure 2.6: Typical reactive power-voltage droop curve [50]. 19
Figure 2.7: Voltage ride-through requirement based on Category II of IEEE 1547-2018 standard [50]. 20
Figure 2.8: FRT requirement for consecutive disturbances based on Category II of IEEE 1547-2018 requirement [50]..... 22
Figure 2.9: Communication structure of CURENT HTB [54]. 24
Figure 2.10: Converter configuration on CURENT HTB platform [55]. 25
Figure 2.11: Type of power emulator on CURENT HTB [55]..... 25
Figure 2.12: Reactive power supply curve based on the operation of DERs at (a) full load (b) no load (c) partial load [21]. 32
Figure 2.13: Market clearing mechanism based on double auction [21]. 34
Figure 3.1: Schematic of the grid-connected PV with SC system (PVSS)..... 37
Figure 3.2: The equivalent circuit of the Zubieta SC model [16], [47]. 39

Figure 3.3: An average current mode control of the SC's DC-DC converter [10]. 41
Figure 3.4: MPP control of the PV's DC-DC converter [86]. 45
Figure 3.5: Cascade control loop of the grid-connected inverter [87]. 47
Figure 3.6: Setup of the PVSS emulator on the HTB. (a) The configuration of the PVSS on the HTB and (b) Experimental test setup of the PVSS on the HTB. 52
Figure 3.7: SC waveforms under constant power charge and discharge profiles. 55
Figure 3.8: Grid voltage support scenarios emulated on HTB. (a) Undervoltage test scneario and (b) Overvoltage test scenario. 57
Figure 3.9: Low-voltage ride-through (LVRT) scenario. 58
Figure 3.10: Grid under frequency support scenarios. (a) Emulation and simulation results during under-frequency support scenario and (b) Emulation results when providing frequency support compared to the case without frequency support. 61
Figure 3.11: RC series SC model. 63
Figure 3.12: Dynamics of SC models based on the constant current charge and discharge profile. (a) Comparison results from [90] and (b) Comparison results from the HTB emulation. 64
Figure 3.13: Comparison of the dynamics of SC models under LVRT operations. (a) SC dynamics under 3 consecutive LVRT operations and (b) Zoom in the SC dynamics at the end of the 3rd LVRT operation. 66
Figure 3.14: Comparison of the dynamics of SC models under grid frequency event (a) under-frequency (b) over-frequency. 67
Figure 4.1: SOC reservation concept. 72
Figure 4.2: Active power-voltage curve for SOC management. 74
Figure 4.3: SC string thermal model [93]–[95]. 76
Figure 4.4: Experimental results of PVSS operation under LVRT event. 81
Figure 4.5: The SC thermal model in Simulink. (a) A single cell SC thermal model in the SC cell subsystem and (b) SC thermal network based on the inline arrangement. 83
Figure 4.6: Comparison results of the SC thermal model in simulation and emulation. 84
Figure 4.7: LVRT performance of the SOC reservation concept compared to the traditional control [20]. (a) Experimental results of the SOC reservation concept and (b) Experimental results of the traditional method [20]. 86

Figure 4.8: Experimental results of the SOC management based on constant current (blue) and current depending on the SC temperature (red). 88
Figure 4.9: Experimental results of SOC management when considering the grid voltage condition. 88
Figure 4.10: Experimental results of SOC management based on the benchmark method (blue) and the proposed method (red). 90
Figure 5.1: DER Supply curves of 5, 10, and 15 kVA in partial load condition. 94
Figure 5.2: Modified DER's supply curves of DERs with similar reactive power capacities in different locations. 98
Figure 5.3: Modified DER's supply curves of DERs with different reactive power capacities in the same location. 100
Figure 5.4: Aggregate DER's supply curve. 100
Figure 5.5: 15-Node test feeder with line parameters from the 8500-node test feeder. 101
Figure 5.6: Aggregate DER's supply curve of participant DERs on the test feeder. 101
Figure 5.7: Voltage profile of the 15-node test feeder before and after reactive power dispatch. 103
Figure 5.8: Modified IEEE-123 node test feeder with connected DERs. 104
Figure 5.9: Voltage sensitivity of DERs with respect to node 114 in the IEEE-123 node test feeder. 104
Figure 5.10: Modified DERs' supply curves of all participating DERs based on Scenario 1. 107
Figure 5.11: Aggregate modified DER's supply curve based on Scenario 1. 107
Figure 5.12: Reactive power dispatch of all DERs with similar reactive power capacities based on Scenario 1. 108
Figure 5.13: Voltage profile after the DERs provide reactive power support based on Scenario 1. 108
Figure 5.14: Reactive power dispatch of DERs with reactive power capacities at 8 kvar (black bar) and 4 kvar (red bar) based on scenario 2. 110
Figure 5.15: Voltage profile after the DERs provide reactive power support based on the scenario 2. 110

Figure 5.16: Reactive power dispatch of DERs with reactive power capacities at 8 kvar (black bar) and 4 kvar (red bar) based on the optimization approach by minimizing voltage deviation at the target location. 112
Figure 5.17: DER's supply curves without considering DER's location. (a) DERs at 5 kVA (orange curve) and 10 kVA rating (blue curve) and (b) Aggregate curve. 113
Figure 5.18: Reactive power dispatch of DERs with reactive power capacities at 8 kvar (black bar) and 4 kvar (red bar) based on the transactive energy approach when not considering the location of the DERs. 114
Figure 5.19: Voltage profile before (■) and after reactive power dispatch of the DERs based on the modified DERs' supply curves approach (●), optimization approach by minimizing the voltage deviation at the target location (▲), and non-location-based reactive power dispatch (×). 116
Figure 6.1: Voltage ride-through requirements for consecutive faults based on different categories [50]. 119
Figure 6.2: Control mode switching of PVSS when SC reaches its voltage limit during LVRT operation. 122
Figure 6.3: PVSS dynamic during LVRT event when SC is unavailable (Base case in blue) and when SC is available (SC in red). 127
Figure 6.4: Comparison of the compensators during LVRT operation at PV operations of (a) 12.5 kW, (b) 25 kW, and (c) 50 kW. 129
Figure 6.5: Comparison of the compensators at voltage sag levels of (a) 0.9 pu, (b) 0.8 pu, (c) 0.65 pu, and (d) 0.5 pu during LVRT operation. 132
Figure 7.1: Concept of the benchmark control [117], [118] and the proposed modified inertia emulation control. 138
Figure 7.2: Frequency dynamics based on different static values of $kiner$ under the under-frequency event. 139
Figure 7.3: PVSS dynamics when adjusting $kiner$ during the under-frequency event. 140
Figure 7.4: PVSS dynamics when adjusting $kiner$ during the over-frequency event. 142
Figure 7.5: PVSS dynamics under different severities of under-frequency events. (a) Constant $kiner$ at 8 and (b) Adjusting $kiner$ from 8 to 2. 143

Figure 7.6: PVSS dynamics under different severities of over-frequency events. (a) Constant $kiner$ at 8 and (b) Adjusting $kiner$ from 8 to 2. 144
Figure 7.7: PVSS dynamics during the frequency recovery period of the under-frequency event based on the bang-bang control compared to the traditional inertia emulation control. 146
Figure 7.8: PVSS dynamics during frequency recovery of the under-frequency event based on bang-bang control without and with inertia deactivation. 147
Figure 7.9: PVSS dynamics during frequency recovery of the over-frequency event based on bang-bang control without and with inertia deactivation. 148
Figure 7.10: The frequency recovery time of the under-frequency event based on the benchmark control [118] and the proposed control at different PV operations (a) 12.5 kW and (b) 25 kW. 150
Figure 7.11: The frequency recovery time of the over-frequency event based on the benchmark control [118] and the proposed control at different PV operations (a) 12.5 kW and (b) 50 kW. 151
Figure 7.12: Impact of the SC's SOC on the performance of fast frequency support during the under-frequency event at (a) the beginning of the event and (b) the recovery period. 153
Figure 7.13: Impact of the SC's SOC on the performance of fast frequency support during the over-frequency event at (a) the beginning of the event and (b) the recovery period. 154

Chapter 1
Introduction

1.1 Background and Motivation

A rapid transition is occurring in today's electric grids from traditional synchronous sources toward inverter-based renewable energy sources (IBRs) such as wind, solar, and energy storage systems [1]. As depicted in Figure 1.1, the installed power capacity from IBRs in 2050 is projected to nearly double compared to the total installed capacity in 2022 across all regions of the U.S. [2]. According to the forecast presented in Figure 1.1, photovoltaic (PV) generation is anticipated to attain the largest installed capacity of 920 GW in 2050 among other types of the IBRs.

Considering that the installed capacities of PV systems are smaller than traditional synchronous generation and have penetrated throughout today's electric grids, future power grids will become more decentralized as illustrated in Figure 1.2. PV systems are considered non-dispatchable resources because their inputs depend solely on solar irradiation, which varies throughout the day. Due to their incapability to generate on-demand power, they can raise stability and reliability concerns for power grids [3]. A primary issue of the PV systems integration on power grids is reported to be PV output fluctuations due to their intermittent nature [3]. As a result of the high penetration of PV systems, several issues have been raised [3], [4] concerning grid performance in terms of voltage and frequency regulations, power quality, reliability, etc.

One solution to enable more integration of PV systems to power grids is by employing energy storage systems (ESSs) [3]. The power generation from PV systems can be stored in the ESSs and later used to meet the load demand and maintain the power balance in the systems. The ESS solution can provide a spinning reserve capability similar to synchronous generators, compensating for the inability of on-demand production of active and reactive power [3]. The limiting wide adoption of ESS solutions for PV applications is because of the present high cost of ESS technologies. However, the Department of Energy (DOE) launched the Long-Duration Storage Shot in 2021, expecting to reduce the cost of grid-scale ESSs by 90%, to 0.05$/kWh by 2030 [5]; thus, the ESS technologies will eventually become more affordable for PV applications.

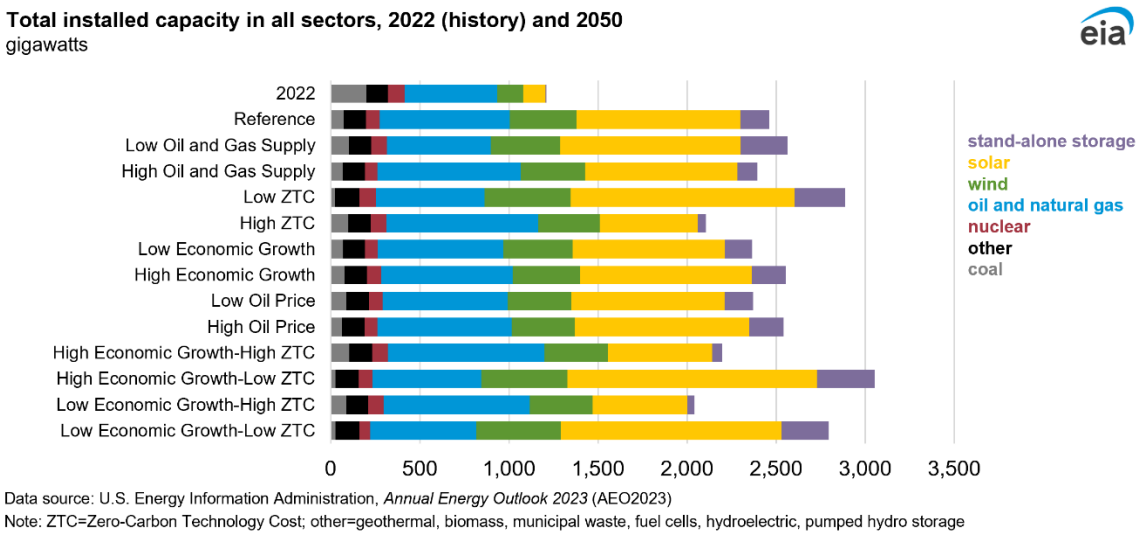

Figure 1.1: Total installed capacity in gigawatts (GW) of all generation in 2022 and the projected capacity for the year 2050 [2].

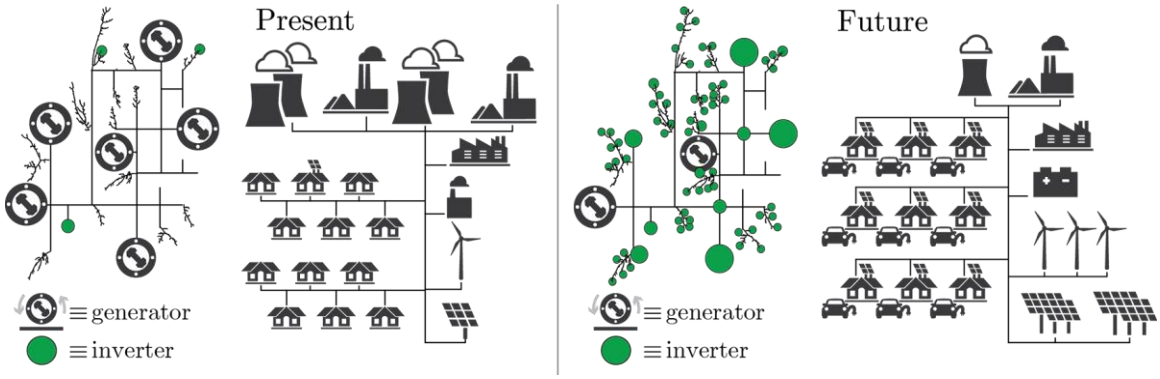

Figure 1.2: Power grid's status of current synchronous generators dominant power grid (left) and IBRs dominant power grid (right) [1].

Supercapacitors (SCs), also known as electric double-layer capacitors or ultracapacitors, are one promising energy storage technology for several applications such as transportation applications (electric traction, ship, and aircraft) and power grid applications [6], [7]. Based on the research publications related to SCs, the utilization of the SCs in power system applications closely follows the transportation applications as can be seen in Figure 1.3 [6]. SCs have gained more attention in PV applications [8]–[10] due to their superior characteristics, including high-power density, ability to undergo numerous charge and discharge cycles, and long service life as shown in Figure 1.4 [11]. SC technology is also part of the focused ESS technologies in the DOE program mentioned previously, intending to reduce the cost of SCs and make them affordable by 2030. In addition, the DOE program aims to enable the potential for long-duration applications of SC technology [12], which implies an expected improvement in SC energy density as part of the program. As a result, the adoption of SCs in grid applications, including PV, is anticipated to increase as costs decrease and energy density improves. SCs are employed as short-term energy storage to smooth the power output from PV systems [10], [13], thereby reducing voltage fluctuations in power grids. SCs also help support PV systems during grid ancillary services [9], including grid frequency regulation and inertia emulation [14], grid voltage regulation [10], and fault ride-through operation [8] to ensure the reliable operation of the power system with high PV integrations. PV systems can efficiently provide these grid services by incorporating SCs as energy buffers that can quickly manage the power balance between the DC and AC sides of grid-connected PV systems [15]. Thus, the PV system can remain connected to the grid and provide support according to the grid's requirements.

It can be challenging to study the behavior of SCs in power systems using physical SCs, because it is difficult to maintain consistent testing conditions of the physical SC under numerous tests [15]. One potential approach to investigate SC behaviors in power system scenarios is to develop its model in a simulator/emulator enabling the study of SC dynamics regarding the test scenarios and the validation of SC control performance. It is important to accurately represent the SC voltage dynamics in both short-term and long-term time durations to serve power system studies [16], [17]. Therefore, selecting the appropriate SC model and implementing it for PV applications is essential to address power system studies in the simulator/emulator environments. Particularly in emulator platforms, where model complexity can be a concern due to the limited computational resources of the emulator's microprocessor. The validation of the SC model in

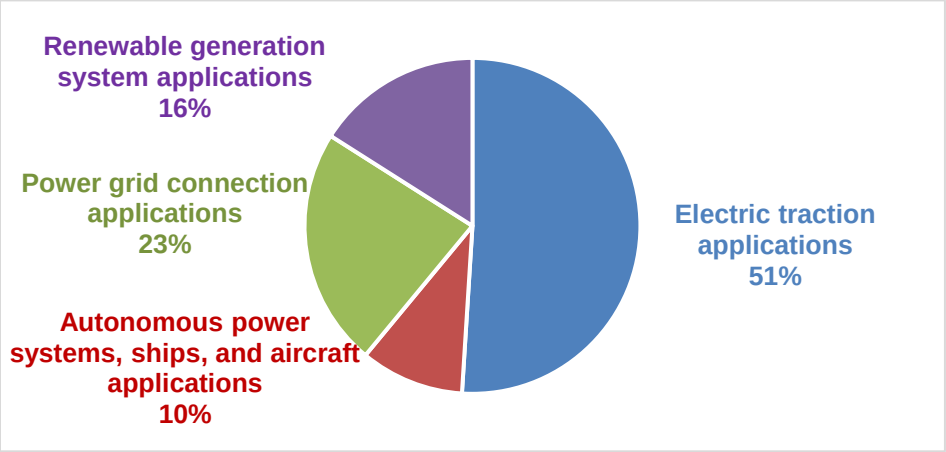

Figure 1.3: Research publications related to SCs based on their applications [6].

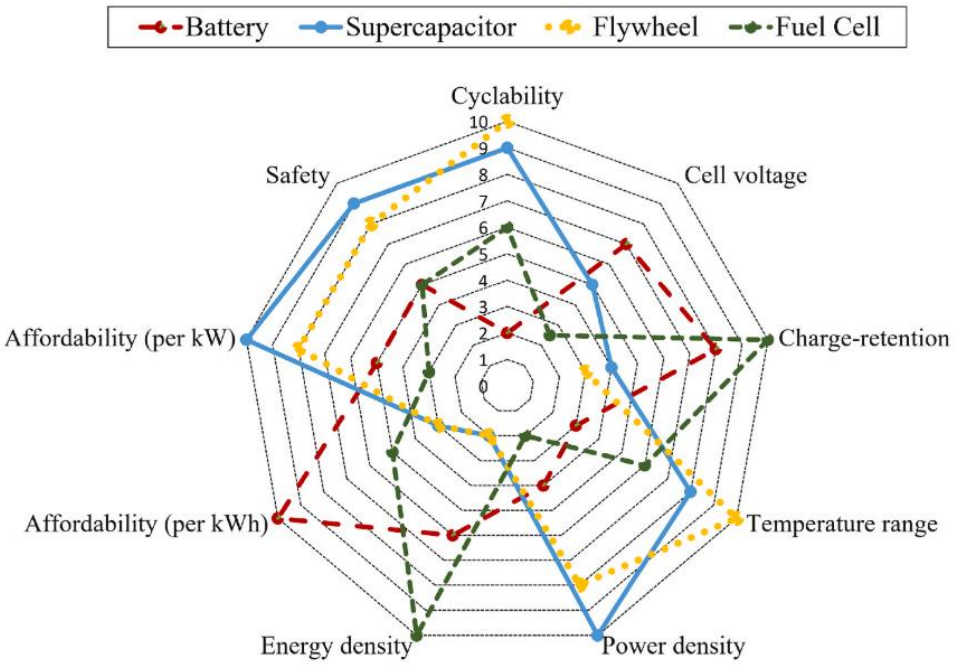

Figure 1.4: Qualitative comparison between energy storage technologies [11].

simulator/emulator is also necessary to ensure the model accuracy under different power system scenarios in both normal operation and grid support operation.

During grid ancillary services, a grid-connected PV with SC system (PVSS) simultaneously provides active power and/or reactive power support in accordance with grid requirements. The setpoints of active and/or reactive power vary depending on the grid support mode, frequency support mode or voltage support mode during normal operation or fault operation. The maximum setpoints during the support can vary up to 100% of the PVSS capacity depending on the categories or agreement established with grid operators, as defined in IEEE-1547 standard for interconnection and interoperability of distributed energy resources with associated electric power systems interfaces [18].

In order to investigate the performance of the PVSS during grid ancillary services, the grid support functions should be adopted in the PV system model with the appropriate SC model in the simulator/emulator in order to capture its dynamics under the power system scenarios accurately [16], [17]. State of charge (SOC) management is used to maintain the availability of SC operations by controlling the SOC of the SC within the working region. The SC availability is a main concern, especially during severe grid disturbances when the SC is used to maintain the PV system's stability [19]. However, previous literature [10], [20] has assumed unlimited SC capacity during grid support, which might not always be the case. Therefore, it is a challenge to develop control strategies for the SC with limited capacity to account for 1) the SC availability during severe fault operations and 2) quickly restoring the SC's SOC within the working range after fault operations so that the SC can be ready for the next operations.

Transactive energy (TE) concept is introduced as part of grid ancillary services, which involves economic and control mechanisms to balance supply and demand in power systems [21]. The TE approach uses incentive signals [22] to engage IBRs to provide support based on their available capacities to systems when needed. The TE approach utilizes a market mechanism, where supply and demand curves are bid into the market in order to determine the market clearing price and amount of support provided to the system [23]. In the context of the TE concept for grid ancillary services, the system operators take on the role of customers, while IBRs serve as service suppliers. The use cases of TE have been carried out in terms of voltage management by incentivizing the IBRs including PV systems to provide reactive power support in [21], [23]. Supplying reactive power over long distances in power systems will result in additional losses in

power lines and increase transmission congestion [24]. Regarding the limitation of the location factor that has not been considered in [21], [23], the reactive power support from very distant locations will not be efficient in improving voltage in the systems. Therefore, the location of the participating IBRs should also be considered when determining their reactive power supply curves. This locational consideration can limit the efficient participation of reactive power suppliers in the market.

1.2 Objectives

This dissertation addresses these research gaps discussed in the introduction and challenges presented above. The objectives are listed as follows:

1) Develop a SC model for PV applications that corresponds to a simulator/emulator to test its control and investigate its dynamics under power system scenarios, including normal and grid ancillary services operations.
2) Develop a state of charge (SOC) reservation control strategy to ensure the availability of the SC for controlling the DC-link voltage during severe disturbances, especially when the system's stability is most vulnerable.
3) Develop a SOC management control method to quickly restore the SC's SOC within the operating region while considering grid conditions, SC limitation, and related converters' capacities to adjust the management power to ensure the safe operations of both PVSS and power grid while maximizing the PVSS capacity during the SOC management.
4) Incorporate locations of reactive power suppliers to determine effective supply curves (cost/kvarh) of reactive power suppliers based on their respective source locations.

1.3 Dissertation Outline

The dissertation outline is presented as follows:

Chapter 2 presents a literature review of the PVSS model and control strategies during both normal and grid support operations, as well as SOC management control methods. The concept of

the transactive energy control approach in the reactive power market will be reviewed. Research challenges and objectives will be summarized in this chapter.

Chapter 3 presents a development of PVSS for simulation and emulation environments. The dynamic performance of the PVSS under grid ancillary services is examined for both the simulator and the HTB emulator, and the comparison results between both environments are provided.

Chapter 4 proposes a SOC reservation concept for the PVSS considering fault ride-through operation. The control approach is proposed to ensure the SC availability during severe FRT operations to maintain the PVSS stability and FRT services in accordance with IEEE-1547 requirements. Additionally, a SOC management method is proposed to quickly restore the SC's SOC within the working region while ensuring safe operations of both the PVSS and the power grid. The results based on the proposed controls will be experimentally evaluated on the HTB.

Chapter 5 proposes the reactive power allocation strategy for grid-connected PV systems based on the TE approach. The proposed modified supply curve method is validated in the power system simulator with the IEEE standard test feeder. The comparison results of the proposed method to other reactive power dispatch methods will be discussed.

Chapter 6 presents the design of a linear quadratic regulator (LQR)-based compensator to reduce the transient DC-link overvoltage during the control mode switching when the SC reaches its capacity during a LVRT operation. The proposed LQR-based regulator is validated on the HTB. The performance of the proposed control in reducing the DC-link overvoltage is compared to a feed-forward controller.

Chapter 7 presents fast frequency support focusing on an inertia emulation provided by the PVSS, which extends the work from Chapter 3. The adjustment of inertia coefficient is proposed to effectively provide support to the grid during the frequency events. The fast frequency recovery service provided by the PVSS is also studied. The proposed control provides support so that the frequency can return to its normal operation quickly.

Chapter 8 presents a summary of the dissertation and outlines related future work that can be undertaken.

Chapter 2

Literature Review

This chapter presents a literature review related to supercapacitor energy storage technology for PV applications. The research activities in this field are explored, including SC models applied in power system study, grid support services offered by SCs, and state of charge control techniques for grid support services. Additionally, research activities in reactive power support provided by distributed energy resources through the engagement of a transactive energy approach are also reviewed. The chapter concludes by providing research gaps according to the research areas.

2.1 Overview of Supercapacitors (SCs)

SCs have remarkable capabilities in terms of high power density, quick charging and discharging, numerous cycles of life, long service life, and a wide temperature operating range compared to battery energy storage technology [6], [12], [25]. However, SCs have limitations in terms of low energy density and high costs. As a result, SCs are particularly attractive for some applications that require high power over short time durations. SCs are also often employed with other storage technologies as hybrid systems, such as batteries, where the SCs support high power transients to extend the battery's lifetime [26].

2.1.1 SC Technologies

SCs can be classified into three main technologies based on the charge storing mechanism [12], [25], [27] including electrochemical double-layer capacitors (EDLCs), pseudocapacitors (PCs), and hybrid electrochemical capacitors (HECs). The EDLC type is commonly used in many applications. It is a symmetrical SC that uses similar materials on both electrodes; anode and cathode [27]. EDLCs have fast charge and discharge capabilities, but they have a high self-discharge rate [12]. In addition, EDLCs have relatively low energy densities compared to other types of SCs because they store energy electrostatically without involving chemical reactions at the electrodes [12], [25], [27]. PCs are also considered symmetric SCs. PCs involve redox reactions in which their energy is stored by transferring charge between the electrode and the

electrolyte. PCs can have larger capacitances and energy densities than EDLCs due to the results of the faradic reactions. However, PCs have limited cycling ability and mechanical stability due to the mechanism of the electrodes; expansion and contraction during the charge and discharge of PCs, respectively [25]. In the early stages of technology development and considering the challenges, PCs are not competitive compared to EDLCs [12]. Consequently, HECs have been developed to overcome the limitations of PCs in terms of cycling and stability. HECs are asymmetric type SCs, which utilize different anode and cathode materials to achieve both faradic and non-faradaic processes for storing energy. Due to the asymmetry in the electrode properties, HECs can have higher power density and significantly higher energy density, approximately ten times more, compared to PCs without suffering from cycling and stability issues [12], [25]. However, in comparison to EDLCs, HECs have a lower life cycle, approximately ten to thirty times less, and they have complex designs and higher costs relative to other types of SCs. These challenges make HECs less attractive than the EDLCs type [12]. The main performances regarding the different types of SCs, are summarized in Table 2.1.

2.1.2 SC Applications in PV Systems

SCs are adopted in a variety of applications including power grids, transportation, smartphones and laptops, and wireless charging [25]. For PV applications in the power grid sector, SCs offer several advantages including to function as short-term energy storage to improve energy self-consumption of PV systems [28], smooth PV power outputs to reduce power fluctuations in power grids [13], [29]–[32], and assist PV systems during grid ancillary services. The grid services provided by SCs include fast frequency support [33]–[35], voltage support [10], and fault ride-through operations [8].

PV systems generate power based on solar irradiation, which naturally varies throughout the day. The high variability of irradiance can result in power fluctuations at points of common coupling (PCC), leading to voltage and frequency instabilities in power grids [30], [32], [36]. One effective solution is to have ramp-rate limitation requirements, which have been widely established in many grid codes to decrease power fluctuations and increase stability in power grids from an increase in PV integrations [37], [38]. The ramp-rate requirement is typically defined as a certain percentage of the nominal capacity of PV systems or maximum power per time duration [30].

Table 2.1: Performance Comparison of Different Types of SCs [25].

	EDLCs	PCs	HECs
Storage mechanism	Non-faradic/ electrostatic, electrical charge stored at the metal/electrolyte interface	Faradic, reversible redox reaction	Both faradaic and non-faradic
Maximum specific power (W/kg)	10,000	4,000	5,000
Cycle life	1,000,000	100,000	500,000
Specific energy (Wh/kg)	3-5	10	180
Operating temperature (°C)	−40 to 65	−40 to 65	−40 to 65

Existing solutions to achieve power ramp rate requirements are presented including PV power curtailment, grid reinforcement, and the use of energy storage systems such as batteries and SCs [32]. PV power curtailment is a common approach to meet the power ramp rate requirements since it does not require an additional investment [32]. However, the PV systems will operate at less than the maximum power point (MPP) to meet the ramp rate limits on power grids. In low-inertia power systems, fluctuations in voltage and frequency can occur more aggressively. Thus, addressing these challenges requires the implementation of advanced PV power curtailment controls to quickly respond to meet the power ramp rate limitations rather than using traditional PV power curtailment methods. Grid reinforcement can also be used to account for the power ramp rate issues in the systems [32]. However, this solution requires extensive investment in equipment upgrades and/or building more feeders. Thus, this method is typically considered a final option if necessary. Nowadays, energy storage has become an attractive solution for many applications driven by cost reductions and advancements in storage technology. Energy storage systems offer flexibility to control power ramp rates in the systems by absorbing or injecting active power depending on the grid conditions [32], [37], [39]. Regarding energy storage technology solutions for power ramp rate application, SCs are a more suitable option than battery storage solutions to manage power fluctuations during the power ramp rate control due to their fast response and high power capability [32].

During grid disturbances, PV systems are required to support power grids to maintain voltage and/or frequency close to their nominal values. The support from PV systems can help improve grid conditions, thus PV systems can continue their operations while improving the stability of power grids. During grid support services, such as low-voltage ride-through operations, PV systems often need to curtail their power output. This is done to prevent overvoltage on DC-links and overcurrent in inverters of PV systems during severe low-voltage conditions where the generated PV power cannot be injected into the grids [40]. Consequently, PV systems might experience short-term overvoltage and overcurrent in their systems [41] due to the slow dynamic of PV power curtailment [42]. Adopting SCs with superior capabilities in terms of high power density and fast response enables efficient power management within PV systems. SCs can quickly absorb or provide power to maintain power balance between PV systems and power grids [43]. Adopting SCs ensures safe operations and prevents disconnection of the PV systems from the grid

during disturbances. Power grids also benefit from the continuous support provided by PV with SC systems, thus increasing the stability of both PV systems and power grids.

Two commonly used topologies to incorporate the SC system in PV applications are presented in Figure 2.1. The first topology involves connecting SCs to the DC-link of grid-connected PV systems through a bidirectional DC-DC buck-boost converter, as shown in Figure 2.1(a) [8], [13]. In this configuration, SCs function as short-term energy buffers, maintaining a power balance between the DC-side and AC-side of the grid-connected PV systems. In the second topology, SCs connect to the PCC through an inverter and/or DC-DC converter as shown in Figure 2.1(b) [29], [30], [34]. This second topology allows SCs to directly regulate the grid conditions in terms of voltage and frequency conditions at the PCC. Among these two topologies, connecting the SC system to the DC-link of grid-connected PV systems is more commonly used because of its cost-effectiveness.

2.1.3 Modelling of SCs in Power System Study

It can be challenging to maintain consistent testing conditions of physical SCs under numerous charge and discharge cycles in power system study. Thus, SCs are usually modeled in power system simulation tools such as MATLAB/Simulink [44] and PSCAD [45]. There are several types of SC models presented in literature, including chemical-based SC model, electrical-based SC model, and intelligent-based SC model that are derived from experimental data [17]. The electrical-based SC model is well-suited for real-time energy management perspective in power system applications due to the model's simplicity and accuracy [17].

In order to investigate SC dynamics under different power system test scenarios, the SC model should be selected so that it can accurately represent the short-term and long-term characteristics of the SC voltage [16], [17]. In power system studies, several literature adopt a simplified SC model including the capacitor (C) model and the capacitor with resistance (RC) model as illustrated in Figure 2.2(a) [45]. These models are simple and require few parameters to represent the SC's dynamics, however, they have poor dynamic responses when it comes to a long-term simulation [46] or under some events such as frequency support where the simplified model yields overly optimistic results [47]. Higher-order models such as the Stern model, transmission

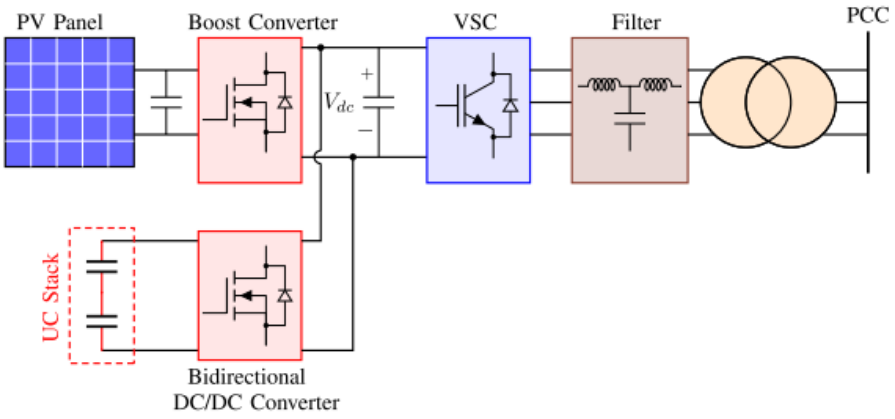

(a)

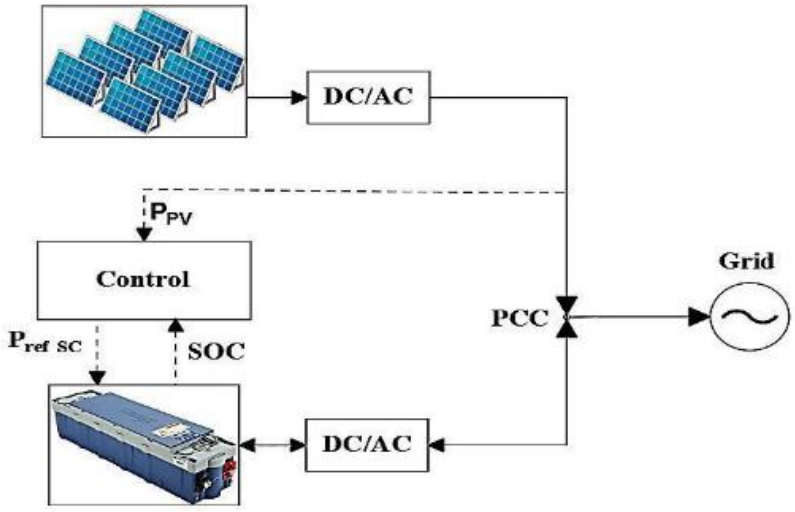

(b)

Figure 2.1: Typical SC configuration for PV applications. (a) The SC system is connected at the DC-link of the PV system [8], [13] and (b) The SC system is connected to the PCC [29], [30], [34].

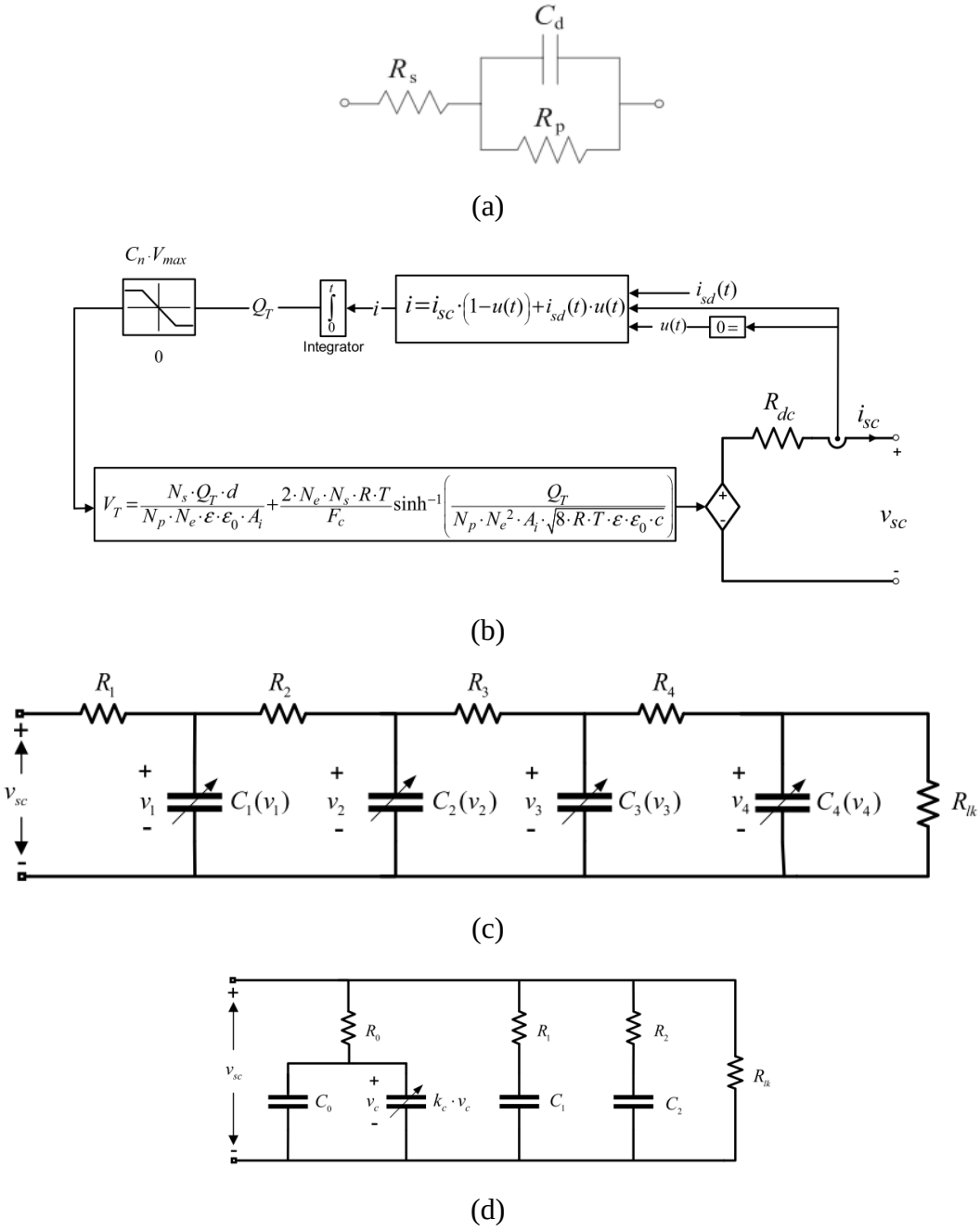

Figure 2.2: Common RC circuits used to represent the models of a supercapacitor cell [16], [17], [46]. (a) RC model, (b) Stern model, (c)Transmission line model, and (d) Zubieta model.

model, and Zubieta model as shown in Figure 2.2(b), (c), and (d) that can accurately represent the SC dynamics in both short-term and long-term might be a better fit.

The Stern model is an electrochemical SC model that represents the nonlinear capacitance of SC related to diffusion dynamics [16]. The Stern model involves knowledge of some physical data of the SC such as the number of electrode layers, molecular radius, the interfacial area between electrodes and electrolyte, etc. Meanwhile, the transmission model consists of several RC branches to represent the SC frequency response between 10 mHz to 1 kHz, making it well-suited for studying the aging process of SCs [16]. The Zubieta model consists of four parallel branches of resistor and/or capacitor elements, each branch representing SC dynamics related to the RC time constant; the first branch represents the fast dynamic in seconds, the second branch represents the SC dynamic in minutes, the third branch represents the SC dynamic in longer than minutes, and the fourth branch represents the leakage current characteristic of the SC [16], [47].

Since the SC model is a critical factor to accurately represent its characteristics for power system studies, the selection of the SC model should consider various factors including model accuracy, time scale of interest, and model complexity [16], [17]. The transmission model requires intensive experiments to obtain the model parameters [17], yet its accuracy compared to other dynamic detailed SC models is similar. Considering these factors, the results from [16] suggest that the Zubieta model provides a good compromise between complexity and model accuracy, thus, it is a good candidate for modeling SCs in power electronic grid interface applications in power system study rather than using oversimplified SC models [17], [48].

2.2 Grid Ancillary Services

Grid ancillary services have been necessary to accommodate the high penetration and integration of IBRs including PV systems in power grids. Traditionally, grid services were accomplished by synchronous generators and grid support devices installed in power systems. Despite the voltage and frequency challenges posed by IBRs, these resources have the capability to provide grid support services. Because IBRs can simultaneously adjust their active and/or reactive power based on grid conditions, they can effectively support the voltage and frequency of power grids.

2.2.1 Frequency Support and Inertia Emulation

The ongoing transition of power systems toward higher penetration of IBRs greatly impacts power system inertia [49]. In traditional power systems with large synchronous generators, the change in frequency during a loss of generation would typically occur gradually due to the inherent inertia capability of synchronous generators [50]. In current power systems where large synchronous generators have been replaced by IBRs distributed over power grids, the systems experience a high rate of change of frequency (ROCOF) because of the decrease in the inertia of systems. Thus, power systems need faster response speed from grid-supporting devices to prevent the operation of under-frequency load shedding protection [49]. Because IBRs have a fast response capability to simultaneously adjust their powers, thus, they can be used to provide frequency and inertia support to power grids with low inertia.

The IEEE 1547-2018 standard requires distributed energy resources (DERs) to adjust their active power according to the deviation of the frequency during grid disturbances from nominal grid frequency to support the frequency stability in power grids. Meanwhile, inertia emulation is optional in the IEEE 1547-2018 standard [18]; however, DERs with energy storage technologies (ES DERs) are recommended to provide inertia emulation in addition to the frequency support based on IEEE 1547.9-2022 standard [50]. This standard serves as the IEEE guide for using IEEE 1547 for the interconnection of energy storage distributed energy resources (ES DERs) with electric power systems. Based on the requirements of the IEEE 1547.9-2022 standard, the term "fast frequency response (FFR)" refers to the frequency support and inertia emulation provided by ES DERs during the arresting period (time before reaching the frequency nadir) as shown in Figure 2.3 [50]. The ES DERs are required to immediately inject or absorb active power in response to changes in grid frequency during FFR operations to improve the frequency nadir or initial ROCOF of frequency [50]. By doing so, the support from ES DERs can prevent the operations of the load shedding relays in the power systems before the actions of other frequency control devices take place to recover the grid frequency to be back within the nominal region.

The typical active power support during FFR can be achieved by using the droop control method as shown in Figure 2.4. The active power support during FFR is a summation of active power calculated from the frequency support loop and inertia emulation loop. The change in the active power of the frequency control loop is based on the frequency support droop coefficient and

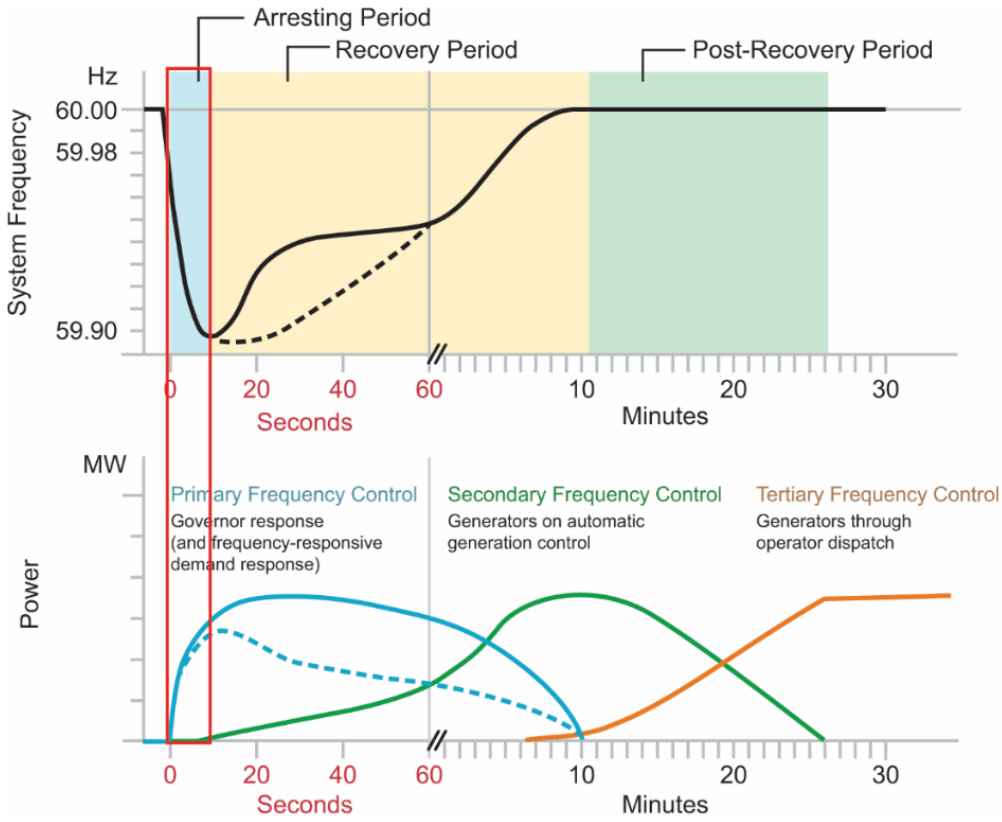

Figure 2.3: Frequency control time frames [49], [50].

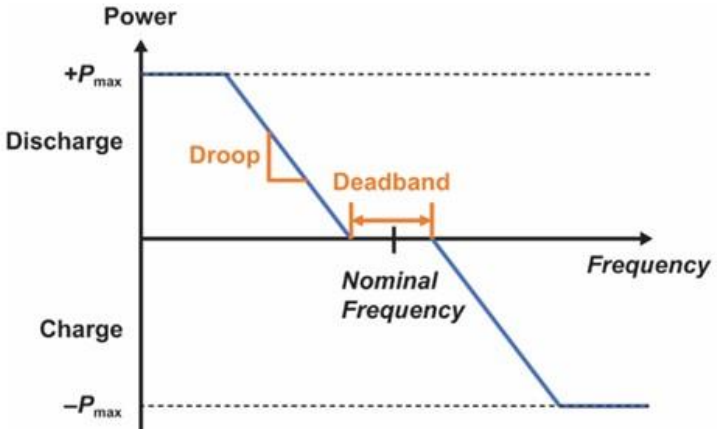

Figure 2.4: Typical active power-frequency droop curve [18].

the deviation of the grid frequency during the event from the frequency deadband during normal operation. Meanwhile, the active power support from the inertia emulation control loop is calculated based on the inertia support droop coefficient and ROCOF of the grid frequency during the disturbance. ES DERs are required to provide FFR for a certain amount of time and severity of the event; ES DERs are required to ride through disturbances only up to 3.0 Hz/second based on Category III requirements in IEEE 1547-2018 standard [18], [50].

2.2.2 Voltage Support

ES DERs can effectively provide voltage support in distribution systems by adjusting their reactive power (absorb/inject) according to the grid voltage conditions. According to the IEEE 1547-2018 standard, the maximum reactive power provided by ES DERs should be at least 44%, and it can be up to 100% of the apparent power rating of ES DERs' inverters [18] as illustrated in Figure 2.5 based on a four-quadrant ES DER capability curve [50]. Even though the ES DERs do not exchange any active power with power grids, i.e., active power is zero, they can adjust reactive power to provide voltage support in power grids [50].

Voltage support from ES DERs can be achieved through a droop control method. The amount of reactive power provided during the voltage support can be calculated based on the droop coefficient of the voltage support function and voltage deviation during the events from the grid voltage deadband during normal operation as shown in Figure 2.6.

2.2.3 Fault Ride-Through (FRT) Operation

During fault ride-through (FRT) operations, ES DERs are required to stay connected to the grid while providing reactive power support to improve voltage conditions in power systems. The amount of reactive power support during FRT operations can be determined according to the grid voltage level, similar to the voltage support operation mentioned in Section 2.2.2. The reactive power support during LVRT operations can be adjusted to contribute more reactive power support i.e., from previously provided at 44% to the full 100% of reactive power capacity, if the grid voltage reaches the low voltage threshold during LVRT operations [51]. The maximum time for providing FRT services depends on voltage conditions during the events as shown in Figure 2.7 for Category II in IEEE 1547-2018 standard. During mandatory operations where the grid voltage

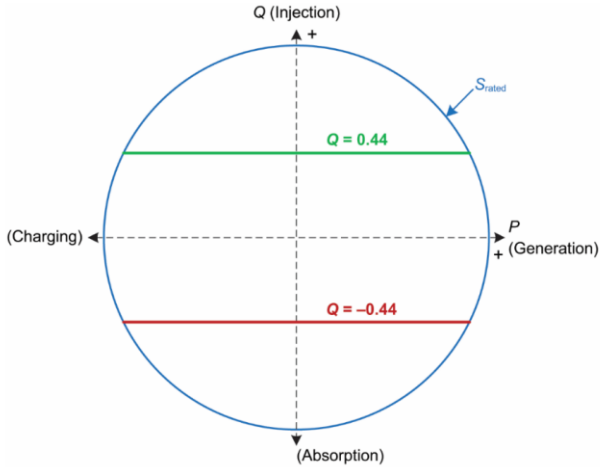

Figure 2.5: Reactive power capability curve of ES DERs [50].

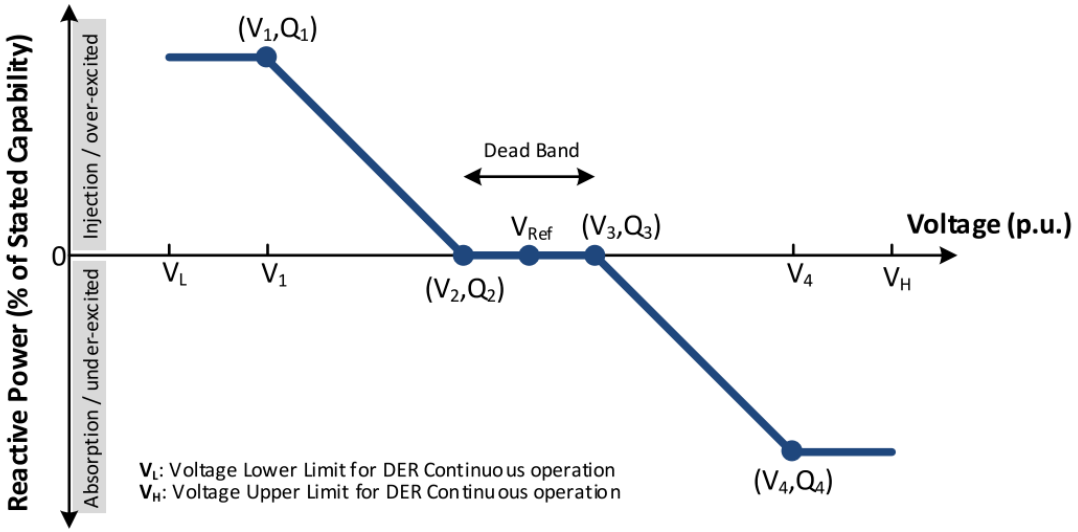

Figure 2.6: Typical reactive power-voltage droop curve [50].

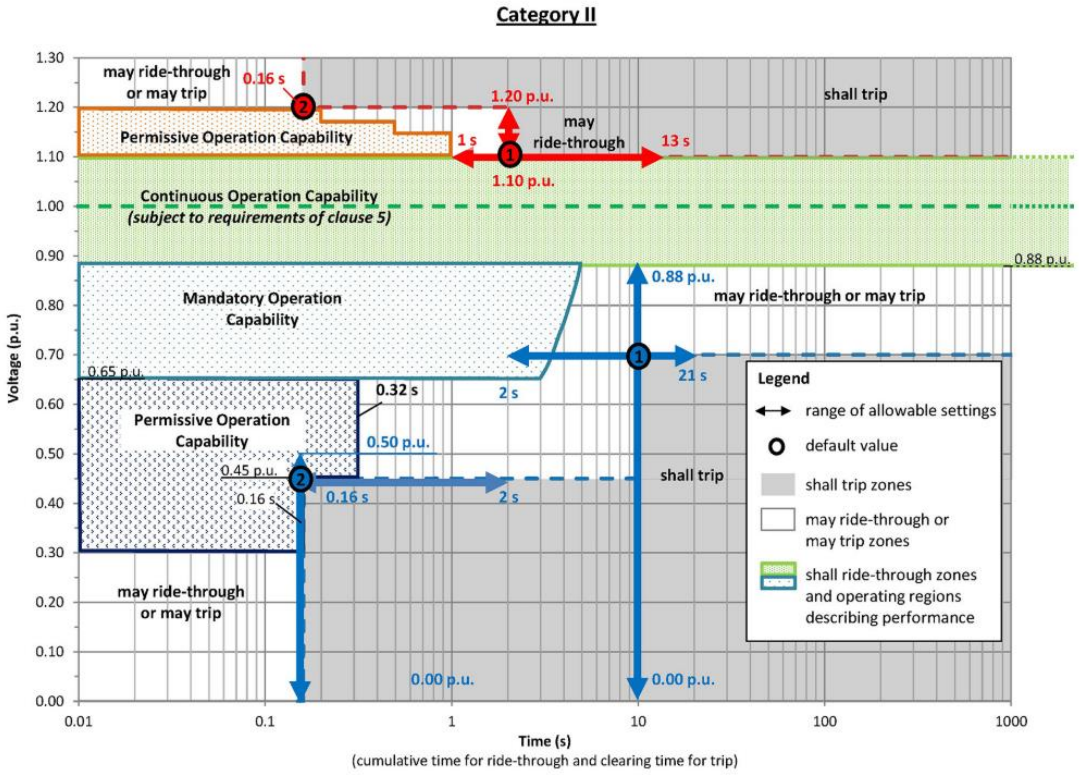

Figure 2.7: Voltage ride-through requirement based on Category II of IEEE 1547-2018 standard [50].

during FRT operation is between 0.65 pu and 0.88 pu, a maximum time of 5 seconds is required for the ES DERs to stay connected to the grid and provide voltage support during the FRT events. The IEEE 1547-2018 standard also requires ES DERs to ride through consecutive faults i.e., ES DERs also need to provide FRT service when the second event happens after the first FRT event is completed for at least 10 seconds based on Category II requirements in Figure 2.8 [50].

Regarding the grid support requirements, the energy capacity of ES DERs is an important factor in determining their performance in providing grid services. Service interruptions may occur if ES DERs run out of capacity or reach their state of charge limits before completing the services. For instance, LVRT operations require ES DERs to support two consecutive faults. After the first LVRT operation is completed, the ES DERs should be able to restore part of their capacity to ensure that they have enough capacity to ride through the second LVRT if needed. Thus, the state of charge control to ensure the ES DERs' availability to provide grid services is required to ensure that the ES DERs can provide grid support complying with grid requirements, especially during severe grid conditions where the stability of both power grids and ES DERs is compromised.

2.3 Hardware Testbed Platform for Power System Study

Grid emulators serve as test platforms for validating novel control strategies and new devices/systems before their actual deployment on power grids [52]. There are two main types of grid emulators including analog-based and digital-based grid emulators.

Analog-based grid emulators involve real hardware configurations to observe the real-time dynamic of the system under test. On the other hand, digital-based grid emulators solely rely on mathematical models and computations within microprocessors. Scaled physical devices are normally used in analog-based grid emulators thus, their results are realistic, yet their limitations are presented in terms of being expensive, bulky, and less flexible [53], [54]. In contrast, digital-based grid emulators offer more flexibility and accessibility than analog-based grid emulators, but they suffer from numerical issues and accuracy from model reductions [52]–[54]. Since some components are absent or simplified in digital-based emulators, such as measurement errors, control, and communication time delays, the results given by digital-based emulators might be unrealistic [52], [53].

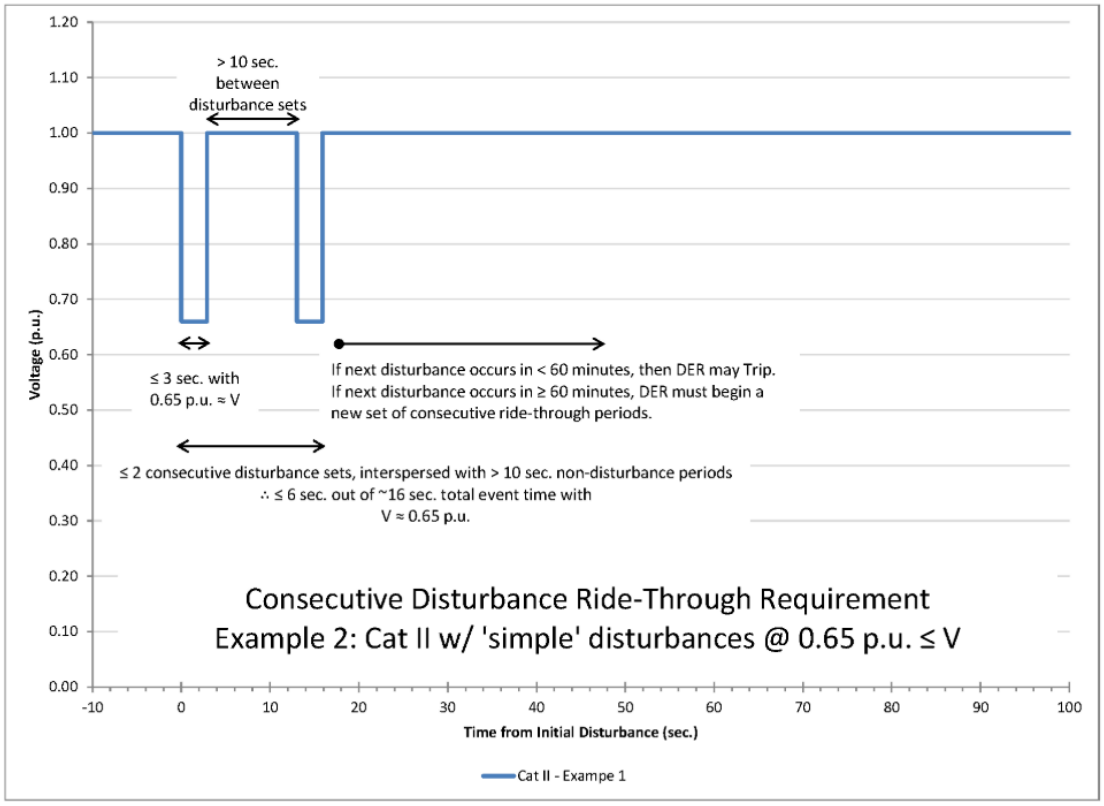

Figure 2.8: FRT requirement for consecutive disturbances based on Category II of IEEE 1547-2018 requirement [50].

Hardware testbed (HTB) is developed by the NSF/DOE Engineering Research Center, CURENT, at the University of Tennessee (UTK) to overcome the limitations of digital-based grid emulators and scaled hardware-based grid emulators [52]. HTB utilizes real-time measurement, control, and communication systems as shown in Figure 2.9, thus, the delays in measurement, control, and actuation are inherent in the HTB platform similar to real systems. Real measurements integrated into the HTB platform include a potential transformer (PT), current transformer (CT), phasor measurement unit (PMU), and frequency disturbance recorder (FDR). The emulators on the HTB can be controlled and monitored remotely through communication established by National Instruments' CompactRIOs using the CAN bus. The control signals from the central control computer (LabVIEW) are sent over to CompactRIOs by ethernet, and the real-time dynamics of the power system under study can be observed through visualization [54].

A parallel converter structure as illustrated in Figure 2.10 is adopted in the HTB where multiple voltage source converters (VSCs) can be configured to emulate different grid components [55] as so-called emulators. All emulators connect to the same DC-link voltage and connect to each other through line inductances on the AC side to form the system under study. This enables the power flow between the emulators on the AC side to be similar to the power flow between grid components in the real power system.

The HTB uses the digital signal processor (DSP) model TMS320F28335 from Texas Instruments as a microprocessor of the HTB emulators. Each emulator uses the real voltage and current measurements on the ac-side as inputs of the emulator's model, depending on the type of the emulator, i.e., voltage source or current source as illustrated in Figure 2.11 [55]. These measurement signals are used as inputs of the power system component model inside of the DSP to generate reference signals for controlling the VSC depending on the operating conditions of the power system component. By doing it this way, the VSC can replicate the behavior of the power system component model without having physical grid components. Thus, the HTB platform is more flexible than the scaled-down analog emulators. However, the HTB can still have numerical issues but less than in digital emulators because the HTB is not solely dependent on the mathematical models [52], [53].

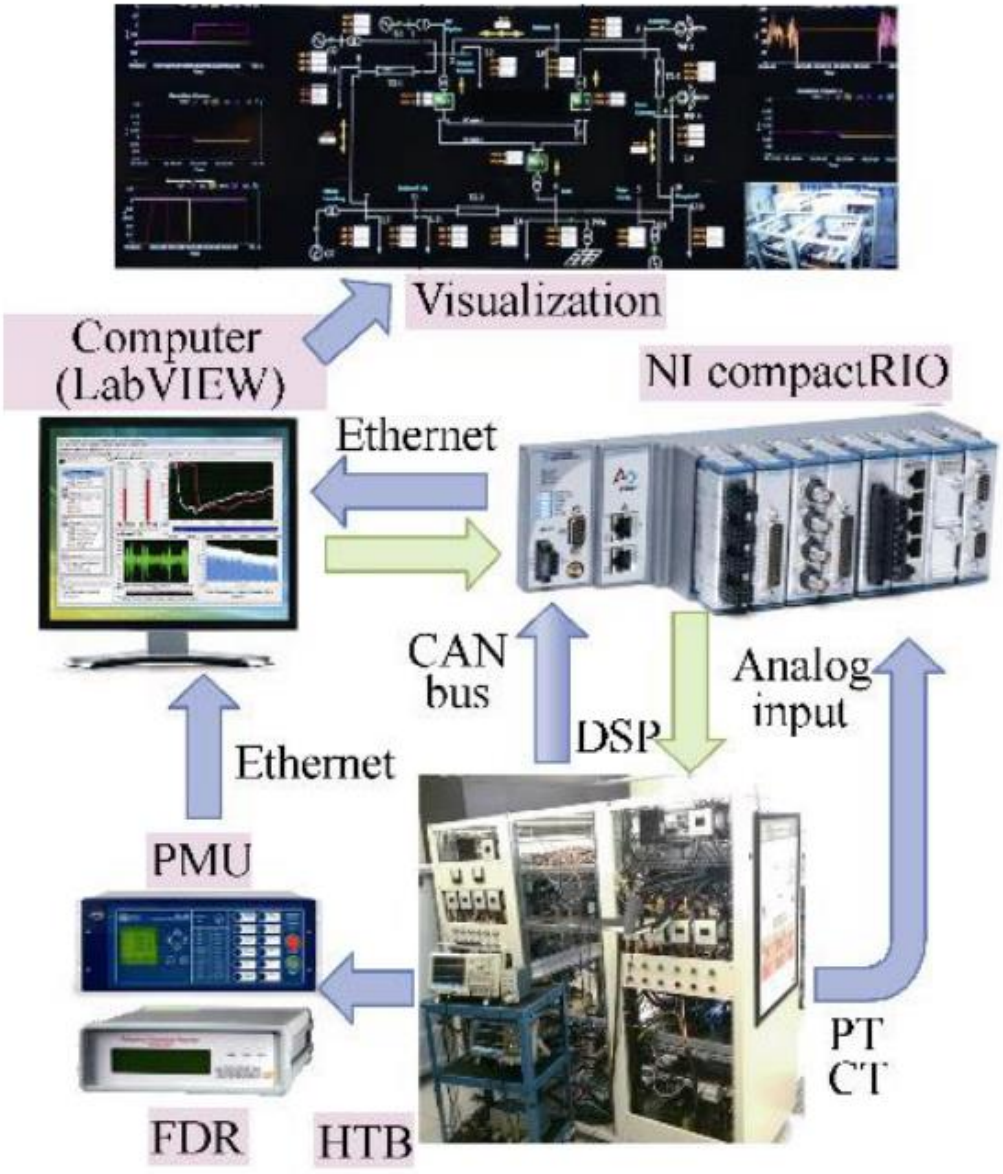

Figure 2.9: Communication structure of CURENT HTB [54].

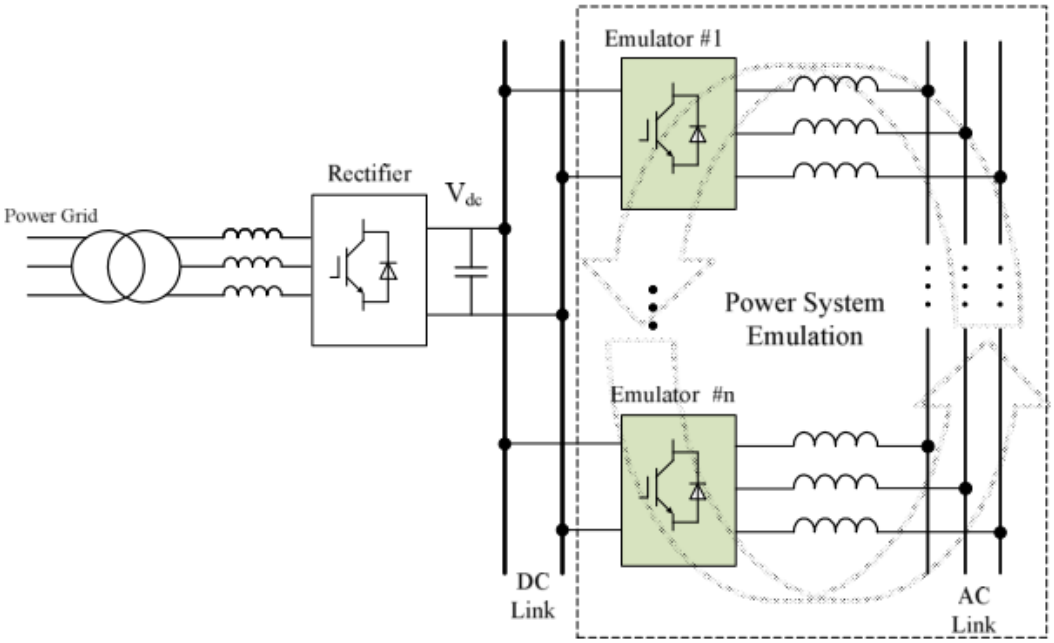

Figure 2.10: Converter configuration on CURENT HTB platform [55].

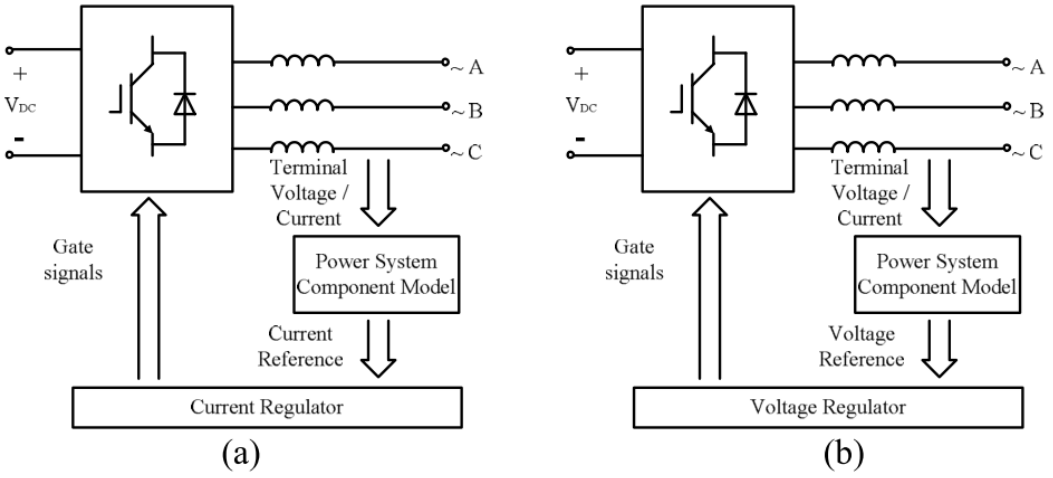

Figure 2.11: Type of power emulator on CURENT HTB [55].

Currently, several grid components can be emulated in the HTB such as synchronous generators [56], energy storage (flywheel, battery [57], [58]), and static and dynamic loads ([59]–[61]) to perform multiple grid scenarios [52]. The emulators in the HTB can be reprogrammed and reconfigured, providing flexibility to represent different power system scenarios [52]. Despite the HTB's extensive capabilities, the HTB currently lacks an SC emulator, which limits the study of grid services offered by ES DERs that have been rapidly increasing in today's systems. The development of the SC emulator will extend the HTB capability to serve more power system studies and represent future grids with a variety of energy storage resources.

2.4 State of Charge (SOC)

State of charge (SOC) serves as an indicator to determine the available capacity of ESSs, typically defined on a scale between 0 to 1 or as a percentage ranging from 0 to 100% of the ESS total capacity. The ESS's SOC is required to be controlled within its working range to prevent overcharging or undercharging the ESS and meet some limitations such as lifetime consideration or voltage requirement of the ESS's interface DC-DC converter.

2.4.1 SOC Management for Grid Ancillary Services

Energy capacity is always a primary concern in the operations of ES DERs. Since ESSs have limited capacities, the operation of an ESS will be interrupted if it runs out of its capacity. To ensure the availability of ESS during operations, SOC management is adopted to restore the ESS's SOC within the working region. Given the focus of this dissertation on grid ancillary service applications, SOC management control methods will be reviewed specifically for grid service applications.

The SOC management controls for grid ancillary services can be mainly categorized into three types based on the activation time of the SOC management; SOC management during normal operation without service provision, SOC management with service provision, and SOC management with service interruption [62]–[64]. For the first case, the SOC management is activated when the ES DER is not in any grid services. Thus, the SOC management will not impact the performance of providing grid ancillary services by ES DERs. In the second SOC management with service provisions, the power supporting the grids will be adjusted by taking the ESS's SOC

into account to maintain the ESS's SOC within the operating region while providing support to power grids. For this type of SOC management, the grid support performance will be impacted by the ESS's SOC since the ESS can support the grid services at full capacity only when its SOC is within a certain region or value, otherwise, the power support will be adjusted according to the available capacity of the ESS. After the grids are back in normal condition, then, the SOC management will be activated to restore the ESS's SOC within the working region. The last case is where the SOC management is activated during the service provisions if the ESS's SOC reaches the limits. This results in the interruption of grid support services and might violate grid code requirements. Moreover, the power during SOC management possibly worsens grid conditions under disturbances in power grids. Therefore, the SOC management methods without service interruption are usually preferred based on the literatures on grid services provision by ESS in [20], [65]–[67] rather than adopting the SOC management with service interruption.

For SC energy storage systems, their SOC also needs to be controlled within the range according to the maximum and minimum of the SC's voltage. The SOC's upper limit is associated with the maximum SC voltage specified in the datasheet to prevent overcharging the SC. The SOC's upper limit can be set lower than its rating to prolong the SC's lifetime [68]. In the case where the SC is connected to a buck-boost DC-DC converter, the minimum SOC is determined by the minimum input voltage requirement of the converter to maintain the converter's ability to regulate the DC-link voltage.

SC availability is the main concern, especially during grid disturbances when the SC is used to maintain the PV system's stability [19]. The SC's SOC will greatly impact the performance of the services. Thus, SOC management plays an important role in regulating the SC's SOC within the operation range where the SC's can be utilized. The SC's SOC is regulated in the middle of the SOC operating region by considering the probability of the SC being charged or discharged equally. Some literature also designs SOC management depending on their applications such as the SOC management in [20], which is designed for grid-connected SC system to provide only FRT services to power systems. Regarding [20], the SOC management will be activated if the SOC reaches its limits (upper limit of 90% or lower limit of 60%), and the SOC will be restored to 80% or 70%, respectively. This SOC management is designed based on the knowledge of the maximum SC's capacity will be used based on the control during the FRT services.

2.4.2 Power Reference during SOC Management

The power reference of SOC management is determined depending on several factors such as power rating, SOC level, and grid condition. A factor of 25% to 30% of the maximum power rating is used as a power reference during SOC management in [20], [62], [69]. Because the full power capacity is not utilized, the time required for SOC management can be longer than it should be. SOC level is considered as a factor to determine the reference current during SOC management in [62], [70]. This method has a disadvantage if the SOC level between its target and the current SOC is low; it will result in a low power reference during SOC management. Thus, a longer time will be required to restore the SOC to the target value. The grid voltage is employed as a function to enable and disable SOC management in most literature [20], [62], [69]. However, this approach can introduce an issue with the constant power during SOC management. This constant power reference can act as a step change, potentially causing oscillation issues in grid voltage when the grid voltage is close to the boundaries that trigger SOC management actions.

According to the SC's high-power capability, it can take a very high current depending on its operating voltage level (v_{sc}) and equivalent series resistance (R_{ESR}) during charging. The maximum charge current ($i_{sc,charge}$) recommended in the application note of the SC's vendor [71] is presented as:

$$i_{sc,charge} = \frac{v_{sc}}{5R_{ESR}} \tag{2.1}$$

The main concern of operating at a high current for a long time is overheating the SC. This can result in an increased R_{ESR}, lifetime degradation, gas generation, and rupture in SC [71]. Thus, there are some thermal limitations specified in the SC's datasheets in terms of the SC operating temperature and its corresponding maximum continuous current [72]. These requirements are used to ensure that the SC temperature can be kept within the recommended temperature operating range during the continuous operation at those current levels.

An application of high SC current operation is presented in [73] for storing regenerative braking of the tram system. The hottest SC cell temperature in the SC module is used to determine the maximum charge and discharge current of the SCs. The study incorporates the electrothermal model of SC cells and their arrangement inside the module to determine the temperature of each

SC cell [73]. The study shows an increase in energy saving by incorporating SC temperature to adjust the SC operations.

Regarding the SC power and temperature capacities, the SC current adjustment based on SC temperature can be a potential solution to achieve SOC management within a short period of time so that the SC can be ready for its next operations while realizing the SC thermal limitation.

2.5 Transactive Energy (TE) Approach

2.5.1 Reactive Power Support Based on the TE Approach

Voltage issues are one of the common challenges that have been reported in systems with high DER penetration levels [74]. Several solutions are available for voltage management in power systems including power system reinforcement and installation of equipment to support reactive power close to the needed locations in the system, such as STATCOM, on-load tap changer, capacitor bank, and inverter [74]–[76]. The reactive power support provided by faraway suppliers can cause high power losses in the power lines, and it limits the power transmission capacity of the feeders. Thus, the installation of reactive power support equipment should consider locations to maximize its performance in improving grid voltages and reducing concerns about the power losses in the system. Nevertheless, incorporating the equipment and systems to address voltage management and improve grid resiliency requires substantial investment and a lengthy timeframe for planning, acquiring, installing, and maintaining these new assets [74]. Consequently, power system operators are leaning towards incorporating the existing devices to support voltage in the systems, avoiding the need for significant investments in new equipment and/or systems.

A transactive approach has been explored in power system voltage management applications by the Pacific Northwest National Laboratory (PNNL) [21]. The use case of this transactive energy concept is engaging non-utility assets to support the voltage in the system by injecting or absorbing reactive power through customer-owned inverters using an incentive signal [21]–[23], [77]. Transactive energy system (TES) sends an incentive signal, which is based on price per kVarh ($/kVarh) to engage the support from non-utility assets for voltage management [21]–[23], [77]. According to this approach, customers can get economic benefits by providing reactive power support from the available capacity of an inverter, and the system operators can get

the reactive power support without installing new equipment and/or systems which would require substantial investment.

Since the specific area of the system was used to demonstrate the use case of transactive energy in voltage management [21], only DERs within the system's area could provide reactive power support to the needed location. For larger power systems where DERs are widely distributed throughout the systems, the DERs' locations can greatly impact voltage support efficiency and power losses in the systems. Thus, this location factor should be considered to determine the amount of reactive power dispatch among the DERs based on the transactive energy approach.

2.5.2 Reactive Power Supply Curve

The concept of engaging transactive energy in voltage management involves leveraging the available capacity of the customer DERs apart from producing active power. These available capacities of the DERs can be used to support the grid by providing reactive power to regulate the grid voltage [78].

The reactive power capacity depends on the rating of the inverter and operated active power, which can be calculated as follows [79], [80]:

$$Q_{capacity} = \sqrt{S_{rated}^2 - P_{inv}^2} \tag{2.2}$$

where $Q_{capacity}$ is the available reactive power capacity of the inverter, S_{rated} is the rated apparent power of the inverter, and P_{inv} is the current active power operating point of the inverter.

Since the transactive energy approach uses an economic concept to balance supply and demand over the system dynamically [21], there are two components involved in this transactive concept including the supply curve and the demand curve. The demand curve represents the required amount of reactive power from the system. Meanwhile, the supply curves are cost curves associated with the cost of inverters to provide reactive power support to the system.

The supply curve can be categorized into two zones based on the operation of the DER's inverter as shown in Figure 2.12. The first zone is when the inverter has the available capacity to provide reactive power without curtailing its active power. This zone is considered a non-curtailment zone as illustrated in Figure 2.12(b). The cost in the non-curtailment zone is related to the cost of the additional power loss in the inverter when providing reactive power support to the

system. The second zone is when the inverter needs to curtail its active power to supply more reactive power into the system. This zone is considered a curtailment zone as illustrated in Figure 2.12(a), (c) where the cost curve is constructed based on two components; the cost of the inverter to curtail its active power and the cost of the additional power loss in order to supply more reactive power into the system.

When operating in the non-curtailment zone, the cost to provide reactive power support comes from the power loss of the inverter, mainly from switching loss, conduction loss, and energy consumption of auxiliary circuits [81]. The power losses can be estimated by using datasheets or test data provided by the inverter's vendors. The power losses of inverters can also be estimated by using inverter efficiency curves [21], [82] from the inverter test reports that include the inverter's efficiency at each power level.

The cost to provide reactive power and corresponding marginal cost while in the non-curtailment zone are given as follows [21], [23]:

$$C_{loss} = ET \times \left[\left(\frac{S_{req}}{\eta_{req}} - S_{req}\right) - \left(\frac{S_0}{\eta_0} - S_0\right)\right] \tag{2.3}$$

$$MP_{loss} = \frac{dC_{loss}}{dQ_{OFR}} \tag{2.4}$$

where C_{loss} represents the cost of power loss of DER for providing reactive power, ET is electricity tariff (\$/kWh), S_{req} and η_{req} are output apparent power of inverter and inverter efficiency while providing reactive power support, respectively. S_0 and η_0 are output apparent power of inverter and inverter efficiency without providing reactive power support, respectively. MP_{loss} is the marginal cost to the DER in the non-curtailment zone. Q_{OFR} is the reactive power offered by the DER.

When operating in the curtailment zone, the cost to provide reactive power and the corresponding marginal cost are given in (2.5)-(2.7) [21], [23], [81].

$$C_{curt} = ET \times \left[\left(\sqrt{S_{inv}^2 - Q_{inv}^2}\right) - \left(\sqrt{S_{inv}^2 - (Q_{inv}^2 + Q_{ofr}^2)}\right)\right] \tag{2.5}$$

$$C_{total} = C_{loss} + C_{curt} \tag{2.6}$$

$$MP_{curt} = \frac{dC_{total}}{dQ_{OFR}} \tag{2.7}$$

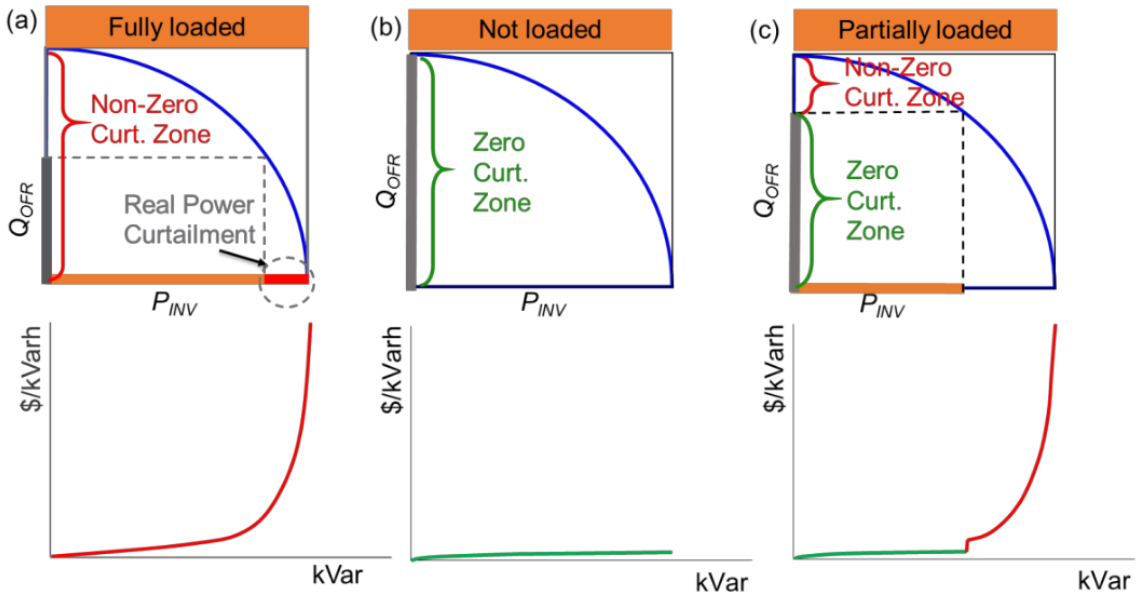

Figure 2.12: Reactive power supply curve based on the operation of DERs at (a) full load (b) no load (c) partial load [21].

where C_{curt} is cost due to loss of revenue (LoR) when the inverter needs to curtail its active power to provide requested reactive power. S_{inv} is the apparent power of the inverter at the operating point. P_{inv}, Q_{inv} are the active and reactive power operating points of the inverter respectively, and Q_{ofr} is the offered reactive power from the DER. MP_{curt} is the marginal curtailment cost to the DER for providing reactive power.

2.5.3 Market Mechanism based on TE Approach

A double-auction mechanism is implemented as a market clearing process between sellers and buyers [21], [23] for reactive power support based on a transactive energy approach. For the reactive power framework, the distribution system operator (DSO) will submit the demand curve as the buyer, and the DERs will submit their demand curves as sellers of reactive power. Regarding the market mechanism, the market is cleared when demand and supply curves intersect as shown in Figure 2.13. At that point, the cost per kVarh ($/kVarh) for the amount of reactive power that the system needs is considered the cleared price for DERs. By integrating the transactive energy approach, both the utility and customers can receive tangible benefits. The customers can earn money based on the available capacity of an inverter for providing reactive power to the system, and the DSO receives system operational benefit from voltage support, which can be done without the need of expensive capital investment.

2.6 Summary

According to the literature review presented in this chapter, the research gaps in the research areas can be summarized as follows:

- There is a lack of an SC emulator that can accurately represent the SC behaviors with appropriate model complexity for power system study on the HTB platform. This limitation affects the investigation of power system scenarios with increased integration of SC energy storage technologies, whether as standalone systems or as part of hybrid energy storage systems with other energy storage technologies.
- Characterization of SCs with grid support controls has not been investigated on the HTB. Implementing grid support controls according to the IEEE 1547-2018 standard

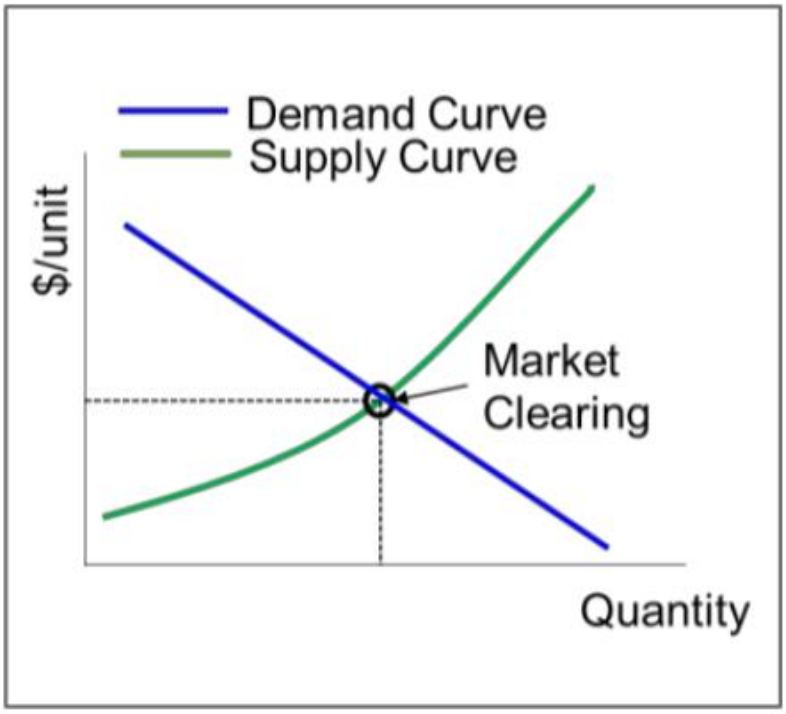

Figure 2.13: Market clearing mechanism based on double auction [21].

and conducting grid support scenarios would allow the observation of SC behaviors under common grid support services.

- A control strategy has yet to be demonstrated that ensures the SC's availability during FRT services to prevent the SC from depleting its capacity during severe FRT services when the stability of both power grids and PV systems are compromised. The control design should be compliant with IEEE 1547-2018 standard requirements during FRT operations.
- The development of a fast SOC management control is necessary to quickly restore the SC's SOC within its operating range. A potential approach to achieve fast SOC management is by incorporating SC thermal capacity to adjust SC power during SOC management. This requires the implementation of an SC thermal model on the HTB platform. In addition, the SOC management control should consider the limitations of devices and/or systems to ensure safe operations of grid, PV, and SC systems.
- The existing study of voltage management based on the transactive energy approach in [21], [23] has not considered the location of DERs when providing reactive power to support voltage in the test system. However, the locations of DERs can significantly impact the performance of voltage improvement if the reactive powers are supplied over long distances in larger test feeders. Thus, the location of DERs should be incorporated into the TE approach to determine the effective reactive power supply curves of DERs for providing voltage management based on the TE concept.
- Validation of the modified TE approach considering the DERs' locations should be performed on a large standard test feeder to ensure the performance of the proposed control.

Chapter 3

Power Emulator of a Grid-Connected PV with SC System (PVSS) on HTB Platform

This chapter presents the development of a grid-connected PV with SC system (PVSS) emulator on the HTB platform. The modeling of a supercapacitor system, PV system, and grid-connected inverter are discussed in detail. The experimental verification of the emulator is presented with the results from the simulation to ensure the accuracy of the developed emulator.

Portions of this chapter have been previously published in the article "Development of a Converter-based Supercapacitor System Emulator for PV Applications" that was presented at the IEEE Energy Conversion Congress and Exposition (ECCE) 2023 meeting.

3.1 PVSS Average Model and Control

In this section, the average model and corresponding control of each system in the PVSS emulator are introduced. As illustrated in Figure 3.1, the PVSS consists of a SC with its bidirectional buck-boost DC-DC converter, a PV with its interface boost DC-DC converter, and a grid-connected inverter. Further details about each subsystem in the emulator are discussed in the following subsections.

3.1.1 SC Subsystem

The SC subsystem in the emulator consists of a SC module and its bidirectional buck-boost DC-DC converter. The DC-DC converter serves as an interface between the SC and DC-link, addressing the wide range of voltage variation during its charge and discharge operations [10].

In power system studies, the SC is typically modeled as a controlled voltage source. The model takes the current going to/from the SC (i_{sc}) as its input, while the terminal voltage of the SC (v_{sc}) serves as the model's output [47], as shown within the red box in Figure 3.1. The HTB emulator adopts the Zubieta SC model due to its capability to provide high accuracy in both short-term and long-term dynamics with moderate complexity, making it suitable for power electronic grid-interfaced applications.

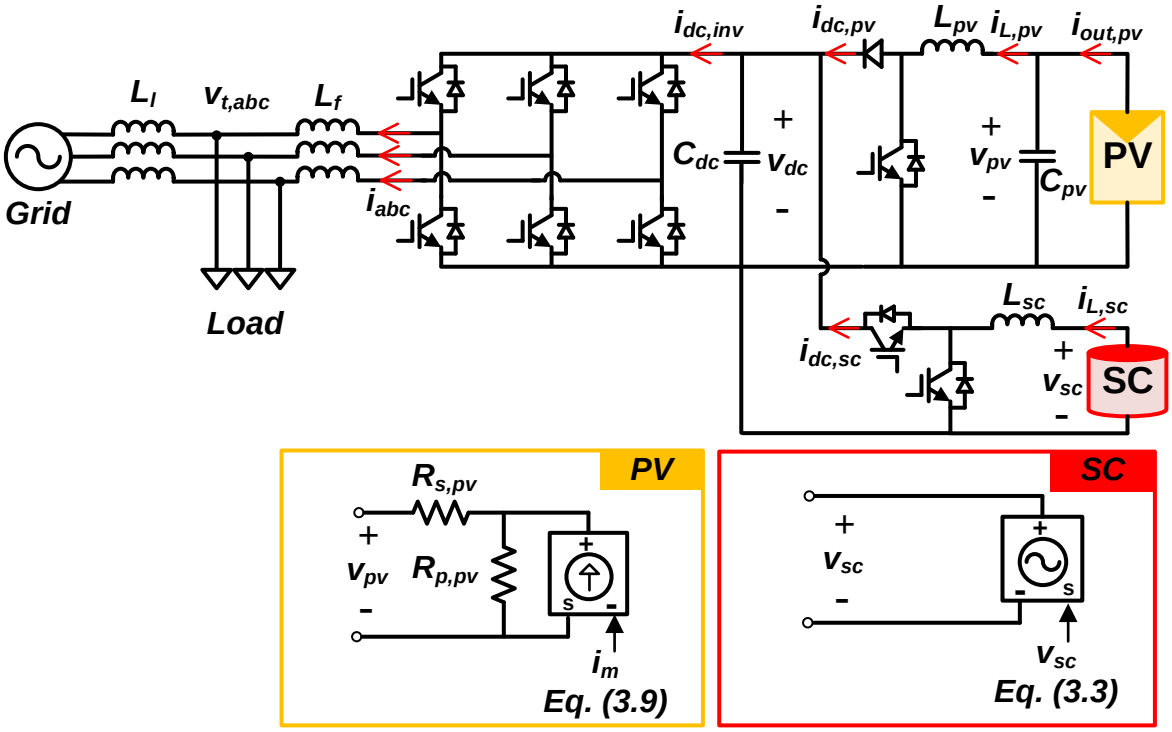

Figure 3.1: Schematic of the grid-connected PV with SC system (PVSS).

According to Figure 3.2, each branch of Zubieta's equivalent circuit model, from the left to the right, represents the SC response in seconds, minutes, longer than minutes, and leakage characteristic, respectively [16], [47]. The internal parameters of the SC used in the HTB emulator are obtained from the experimental tests referred from [46], representing the 3000 F, 2.7 V SC manufactured by Maxwell Technologies (BCAP3000). This cell is designed for high-power and energy applications such as grids, UPS systems, and transportation [72]. The relevant parameters of the SC used in the emulator are presented in Table 3.1.

SC cell voltage ($v_{sc,cell}$) of the Zubieta SC model can be calculated by using its relationship with the first branch capacitor charge (Q_0) [17] and its open circuit voltage ($v_{sc,ocv}$) as a function of its state of charge [83] as:

$$v_{sc,cell} = v_{sc,ocv} + R_0 i_0 + \frac{1}{C_{01}}\left(-C_0 + \sqrt{C_0^2 + 2C_{01}Q_0}\right) \tag{3.1}$$

Other SC parameters in (3.1) can be calculated as follows:

$$\begin{aligned} Q_0 &= \int i_0\, dt \\ i_0 &= \frac{i_{L,sc}}{N_{p,sc}} - i_1 - i_2 - i_{Rlk} \\ i_1 &= \frac{1}{R_1}(v_{sc,cell} - v_{c1}) \\ i_2 &= \frac{1}{R_2}(v_{sc,cell} - v_{c2}) \\ i_{Rlk} &= \frac{1}{R_{lk}}(v_{sc,cell}) \\ v_{c1} &= \frac{1}{C_1}\int i_1\, dt \\ v_{c2} &= \frac{1}{C_2}\int i_2\, dt \end{aligned} \tag{3.2}$$

The parameters in the SC's model equations are associated with their labels in Figure 3.2. Here, i_x, v_{cx}, R_x, C_x represent the current going through each branch of the Zubieta SC model, the capacitor voltage, resistance, and capacitance of the elements in branch x from left to right in the figure. The last branch of the Zubieta model is labeled as R_{lk} because it represents leakage characteristic without having any capacitors in that branch. In the first branch, there are two capacitors C_0 and C_{01}, where the C_{01} is a variable capacitor, and its value is a function of the voltage across C_0 (v_{c0}). The sign of the $i_{L,sc}$ in (3.2) will change based on the SC operating conditions; $+i_{L,sc}$ when charging the SC and $-i_{L,sc}$ when discharging the SC.

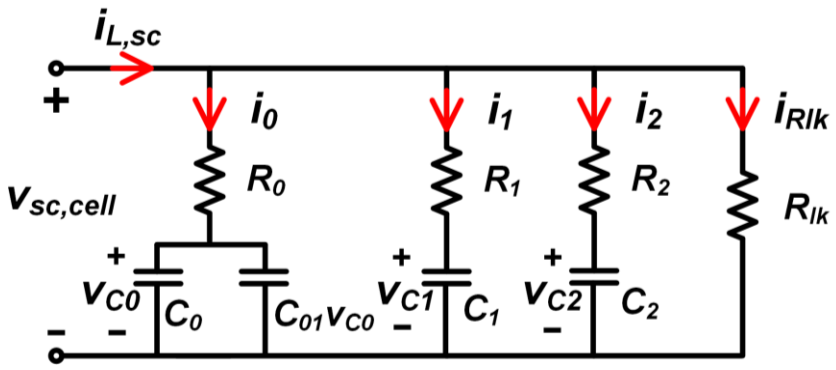

Figure 3.2: The equivalent circuit of the Zubieta SC model [16], [47].

Table 3.1: Zubieta SC model Parameters [46].

Zubieta SC model Parameters	**Values**
R_0	0.322 mΩ
R_1	0.381 Ω
R_2	1.328 Ω
R_{lk}	59.436 kΩ
C_0	2934.7 F
C_{01}	130.8 F
C_1	76.8 F
C_2	1518.8 F

SC cells are typically connected in series and/or parallel to form a SC module to meet the power, energy, and voltage requirements based on the application. The voltage of the SC module (v_{sc}) can be calculated as follows:

$$v_{sc} = N_{s,sc} v_{sc,cell} \tag{3.3}$$

where $N_{s,sc}$ is the number of the SC cells connected in series and $N_{p,sc}$ is the number of the SC strings in parallel.

The state of charge of the SC module (SOC_{sc}) can be calculated by the ratio of the v_{sc} and the rated voltage of the SC module ($v_{sc,rating}$) as:

$$SOC_{sc} = \frac{v_{sc}}{v_{sc,rating}} \times 100 \tag{3.4}$$

A bidirectional buck-boost DC-DC converter serves as an interface between the SC and the DC-link. The converter operates as a boost converter when discharging the SC and as a buck converter when charging the SC [10]. The average model of the buck-boost DC-DC converter of the SC in continuous conduction mode (CCM) can be derived as:

$$\begin{aligned} L_{sc} \frac{di_{L,sc}}{dt} &= v_{sc} - v_{dc}(1 - d_{sc}) \\ i_{dc,sc} &= i_{L,sc}(1 - d_{sc}) \end{aligned} \tag{3.5}$$

where d_{sc} is the duty cycle of the SC's DC-DC converter. $i_{L,sc}$ is the current going through the inductor (L_{sc}), and $i_{dc,sc}$ is the output current of the SC's DC-DC converter injected into the DC-link.

A typical average current mode control is employed to control the operation of the converter as presented in Figure 3.3. This control method has superior stability compared to voltage mode control and peak current mode control [10]. Consequently, it ensures the stability of the converter with a wide range of operations during both buck and boost modes [10]. According to the average current mode control, the outer PI control loop is for controlling the DC-link voltage to its reference value, and this loop will generate the average current reference for the inner PI control loop. The inductor current of the SC's DC-DC converter ($i_{L,sc}$) is controlled by the inner PI control loop to follow its current reference by charging or discharging the SC to regulate the DC-link voltage to be close to its nominal value. The PI compensators used in the SC's DC-DC

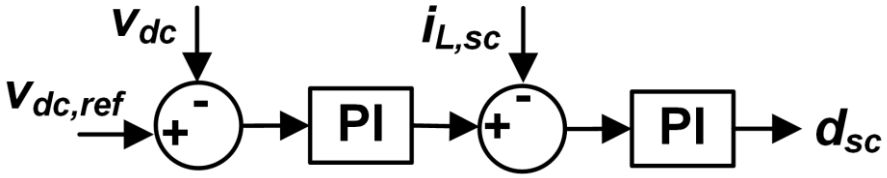

Figure 3.3: An average current mode control of the SC's DC-DC converter [10].

converter for the outer voltage control loop and the inner current control loop are designed by using respective transfer functions $G_{vi}(s)$ and $G_{id}(s)$ as follows [10]:

$$G_{vi}(s) = \frac{(1-d_{sc})\left(1-\frac{sL_{sc}}{R_{dc}(1-d_{sc})^2}\right)}{\left(sC_{dc}+\frac{2}{R_{dc}}\right)} \tag{3.6}$$

$$G_{id}(s) = \frac{v_{dc}\left(sC_{dc}+\frac{2}{R_{dc}}\right)}{s^2L_{sc}C_{dc}+\frac{sL_{sc}}{R_{dc}}+(1-d_{sc})^2} \tag{3.7}$$

where R_{dc} is an equivalent load resistant of the SC's DC-DC converter.

The controller of the DC-link voltage control loop is designed to have a lower bandwidth than the controller for the SC current loop to be less sensitive to noise [10]. Meanwhile, the current control loop's controller is typically designed with a higher bandwidth to have a faster response while maintaining sufficient phase margin for stability. The controller's parameters of the SC's DC-DC converter based on the following design considerations are provided in Section 3.3.1.

3.1.2 PV Subsystem

The PV system adopted in the HTB emulator is based on a double stage topology, where the PV arrays connect to a boost DC-DC converter before connecting to the DC-link. The PV model is adopted from [84] where the PV system is modeled by a controllable current source as illustrated within the yellow box in Figure 3.1. The output current of the PV model ($i_{out,pv}$) can be derived as follows:

$$i_{out,pv} = \frac{R_{p,pv}}{R_{s,pv}+R_{p,pv}}\left(i_m - \frac{v_{pv}N_{p,pv}}{R_{p,pv}N_{s,pv}}\right) \tag{3.8}$$

where $N_{s,pv}$ is the number of series-connected modules per string and $N_{p,pv}$ is the number of parallel strings. $R_{p,pv}$ and $R_{s,pv}$ are equivalent series and parallel resistances of the PV module, and v_{pv} is the output voltage of the PV module.

The current source (i_m) of the PV model in (3.8) can be calculated by using (3.9) as follows:

$$\begin{aligned} i_m &= i_{pv}N_{p,pv} - i_0 N_{p,pv}\left[exp\left(\frac{v_{pv}+\frac{R_{s,pv}N_{s,pv}}{N_{p,pv}}i_{out,pv}}{v_{t,pv}\times a\times N_{s,pv}}\right)-1\right] \\ i_{pv} &= \frac{G}{G_n}\left(i_{pv,n}+K_i\Delta T_{pv}\right) \\ i_0 &= \frac{I_{pv,scn}+K_i\Delta T_{pv}}{exp\left[v_{t,pv}\left(V_{pv,ocn}+K_v\Delta T_{pv}\right)-1\right]} \\ v_{t,pv} &= \frac{k\times N_{s,cell}\times T_{pv}}{q} \\ \Delta T_{pv} &= T_{pv}-T_{pv,n} \end{aligned} \tag{3.9}$$

where i_{pv} and $i_{pv,n}$ are the light-generated current and light-generated current at the nominal condition. G and G_n are the irradiation and nominal irradiation in W/m^2. T_{pv} and $T_{pv,n}$ are PV cell temperature and nominal PV cell temperature in Kelvin. i_0 is the diode saturation current. $v_{t,pv}$ is the thermal voltage of $N_{s,cell}$ series-connected cells. The nominal open circuit voltage and nominal short circuit current are represented by $V_{pv,ocn}$ and $I_{pv,scn}$, respectively. K_v is the coefficient of the open circuit voltage per temperature in V/K, and K_i is the coefficient of the short circuit current per temperature in A/K. a is a diode ideality constant, with a value between $1 \le a \le 1.5$. k is the Boltzmann constant in J/K. Additional details of the PV model can be found in [84].

The nominal PV parameters are typically provided by PV vendors and specified in their PV datasheets. All related PV parameters in the HTB emulator are referenced from the PV array model in Simulink [85], which includes the PV parameters regarding the modeled PV modules. The PV parameters in the HTB emulator are provided in Section 3.3.1.

Since the PV arrays connect to the DC-link through a boost DC-DC converter, v_{pv} in (3.8-3.9) can be calculated by the average model of the PV's DC-DC converter in CCM as:

$$\begin{aligned} C_{pv}\frac{dv_{pv}}{dt} &= i_{out,pv} - i_{L,pv} \\ L_{pv}\frac{di_{L_{pv}}}{dt} &= v_{pv} - v_{dc}\left(1-d_{pv}\right) \\ i_{dc,pv} &= i_{L,pv}\left(1-d_{pv}\right) \end{aligned} \tag{3.10}$$

where d_{pv} is the duty cycle of the PV's boost DC-DC converter. C_{pv} is the output capacitor of the PV arrays before connecting to the PV's DC converter. $i_{L,pv}$ is the current going through the inductor (L_{pv}) and $i_{dc,pv}$ is the output current of the PV's DC converter injected into the DC-link.

The PV system operates in maximum power point (MPP) mode to maximize its power generation. According to Figure 3.4, the MPP control based on the perturb and observe (P&O) method is adopted from [86] in the HTB emulator. The algorithm observes the PV powers before and after the change of the PV's system operation by adjusting the duty cycle of the PV's DC-DC converter. The new duty cycle is determined to move the PV operation towards the maximum power by checking the changes in PV power and PV voltage between the present state and previous operations as shown in Figure 3.4. When there are changes in PV power, a small constant perturbation of the duty cycle (Δd_{pv}) will be added to the previous value of the duty cycle ($d_{pv}(t-1)$) under the following conditions:

- Positive change in PV power ($+\Delta p_{pv}$) with negative change in PV voltage ($-\Delta v_{pv}$).
- Negative change in PV power ($-\Delta p_{pv}$) with positive change in PV voltage ($+\Delta v_{pv}$).

In cases other than the specified conditions, the new duty cycle of the PV's DC converter will be determined by subtracting Δd_{pv} from $d_{pv}(t-1)$.

3.1.3 Grid-Connected Inverter Subsystem

A grid-connected inverter serves as an interface that connects the DC-link to the rest of the power grid via an inductive filter (L_f). It controls the power flow between the power grid and the DC side (PV and SC subsystems) according to the PVSS operations.

The average model of a grid-connected inverter in the direct-quadrature (dq) coordinate system is presented as follows:

$$\begin{aligned} L_f \frac{di_d}{dt} &= v_{dc} d_{inv,d} - v_{t,d} + \omega L_f i_q \\ L_f \frac{di_q}{dt} &= v_{dc} d_{inv,q} - v_{t,q} - \omega L_f i_d \end{aligned} \tag{3.11}$$

where i_d and i_q represent the inverter's current, while $v_{t,d}$ and $v_{t,q}$ represent the terminal voltage of the inverter after the filter in the d-axis and q-axis, respectively. ω is an ac output frequency, $d_{inv,d}$ and $d_{inv,q}$ are the inverter's duty cycle in the dq coordinate system.

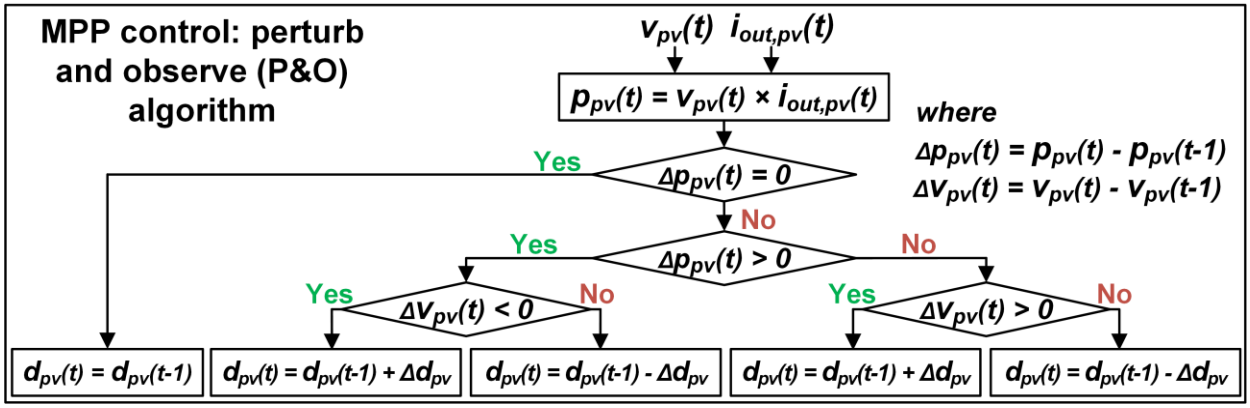

Figure 3.4: MPP control of the PV's DC-DC converter [86].

The dynamic behavior of the DC-link can be expressed by the DC-link voltage (v_{dc}) and the summation of the currents from the DC-side systems ($i_{dc,pv}$, $i_{dc,sc}$) to the grid-side inverter ($i_{dc,inv}$). The DC-link voltage dynamic can be calculated as:

$$C_{dc}\frac{dv_{dc}}{dt} = i_{dc,pv} + i_{dc,sc} - i_{dc,inv} \tag{3.12}$$

where $i_{dc,inv}$ is determined by assuming that the power entering the AC-side is equal to the power leaving the DC-side, as mentioned in [58]. The power on the AC-side can be calculated by using the inverter dq-axis current (i_{dq}) and the voltage before the inverter filter ($v_{inv,dq}$), which can be derived from (3.11). The related equations for calculating $i_{dc,inv}$ are presented as follows [58]:

$$\begin{aligned} i_{dc,inv} &= \frac{1.5}{v_{dc}}\left(v_{inv,d}i_d + v_{inv,q}i_q\right) \\ v_{inv,d} &= v_{t,d} + L_f\frac{di_d}{dt} - \omega L_f i_q \\ v_{inv,q} &= v_{t,q} + L_f\frac{di_q}{dt} + \omega L_f i_d \end{aligned} \tag{3.13}$$

A cascade inverter's control [87] in dq coordinates is adopted in the PVSS model, as shown in Figure 3.5. The outer loop is for controlling the active power (P_{inv}) and reactive power (Q_{inv}) of the inverter to follow their reference signals ($P_{inv,ref}, Q_{inv,ref}$). The inverter powers are calculated using the following equations:

$$\begin{aligned} P_{inv} &= 1.5\left(v_{inv,d}i_d + v_{inv,q}i_q\right) \\ Q_{inv} &= 1.5\left(-v_{inv,d}i_q + v_{inv,q}i_d\right) \end{aligned} \tag{3.14}$$

$P_{inv,ref}$ and $Q_{inv,ref}$ of the inverter can be determined by the PVSS operation modes, i.e. normal operation, or grid support operation. During normal operation, $P_{inv,ref}$ is set equal to the PV power generation to inject the generated power into the grid with zero reactive power output ($Q_{inv,ref} = 0$). If the voltage support mode is enabled due to voltage disturbances on the grid, $Q_{inv,ref}$ is determined according to the grid voltage level ($Q_{inv,ref} = f(v_{grid})$ to provide reactive power to improve the grid voltage condition. In such cases, $P_{inv,ref}$ is adjusted to avoid overloading the inverter during grid voltage support when higher priority is given to the reactive power, ensuring the active and reactive power provided does not exceed the inverter rating. In the case where the grid frequency support mode is enabled, $P_{inv,ref}$ is also adjusted when active power

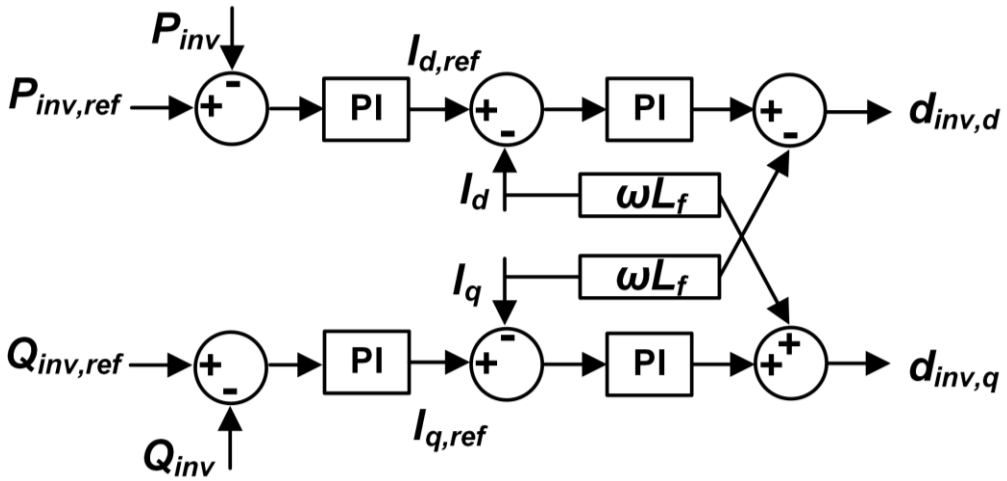

Figure 3.5: Cascade control loop of the grid-connected inverter [87].

is required to improve grid inertia and frequency during grid frequency disturbances. More details of these grid support services will be discussed later in this chapter.

According to the control scheme shown in Figure 3.5, the reference currents of the inner control loop can be calculated as:

$$\begin{aligned} i_{d,ref} &= k_{p,pq}\left(P_{inv,ref} - P_{inv}\right) + k_{i,pq}\int\left(P_{inv,ref} - P_{inv}\right) \\ i_{q,ref} &= k_{p,pq}\left(Q_{inv,ref} - Q_{inv}\right) + k_{i,pq}\int\left(Q_{inv,ref} - Q_{inv}\right) \end{aligned} \tag{3.15}$$

where $k_{p,pq}$ and $k_{i,pq}$ represent the PI control parameters of the power controllers in both d and q-axis.

The inner PI loops control the inverter's currents (i_d, i_q) to track their reference currents $(i_{d,ref}, i_{q,ref})$ generated by the active power control loop and the reactive power control loop, respectively. The outputs of the inner current control loops are compensated to eliminate the voltage cross-coupling terms between each axis [88] before generating $d_{inv,dq}$ to control the operations of the inverter.

The inner current control loop of the inverter is tuned to have a much higher control bandwidth than the outer power control loop to decouple both loop dynamics. The inner current control loop of the HTB emulator is similar to all current source emulators [89]. The duty cycle determined by the inner current control loop will be used to control the physical inverter of the emulator [54], [88], [89]. The controller parameters used in both control loops of the grid-connected inverter are provided in Section 3.3.1.

3.2 PVSS Emulator

To emulate the PVSS on the HTB platform, each model in the system needs to be digitized in order to embed it into an emulator's microprocessor [58], [60], [61]. The HTB uses the digital signal processor (DSP) model TMS320F28335 from Texas Instruments as a microprocessor of the emulator. The sampling time (T_s) used in the discrete equations is based on the DSP sampling time at 0.1 ms, corresponding to a 10 kHz switching frequency of the inverter.

The average models of the PVSS presented in Section 3.1 are converted to discrete formats using the Forward Euler method. In this method, the outputs of the computation cycle $[x + 1]$ are

estimated by the results of the previous cycle $[x]$. The discretized model of the PVSS is presented in the following subsections.

3.2.1 Discrete Model of PVSS Emulator

3.2.1.1. SC Discrete Model

The Zubieta SC model in discrete format can be derived as:

$$v_{sc,cell}[x+1] = v_{sc,ocv} + R_0 i_0[x] + \frac{1}{C_{01}}\left(-C_0 + \sqrt{C_0^2 + 2C_{01}Q_0[x]}\right) \tag{3.16}$$

Other SC parameters used in (3.15) can be calculated as:

$$\begin{aligned} Q_0[x+1] &= Q_0[x] + T_s i_0[x] \\ i_0[x+1] &= \frac{i_{L,sc}[x]}{N_{p,sc}} - i_1[x] - i_2[x] - \frac{v_{sc,cell}[x]}{R_{lk}} \\ i_1[x+1] &= \frac{1}{R_1}(v_{sc,cell}[x] - v_{c1}[x]) \\ i_2[x+1] &= \frac{1}{R_2}(v_{sc,cell}[x] - v_{c2}[x]) \\ v_{c1}[x+1] &= \frac{1}{C_1}(i_{1,int}[x]) \\ v_{c2}[x+1] &= \frac{1}{C_2}(i_{2,int}[x]) \\ i_{1,int}[x+1] &= i_{1,int}[x] + T_s i_1[x] \\ i_{2,int}[x+1] &= i_{2,int}[x] + T_s i_2[x] \end{aligned} \tag{3.17}$$

where $i_{1,int}[x]$ and $i_{2,int}[x]$ in the equations represent the integral of i_1 and i_2 over time, respectively.

The SC module's voltage can be calculated as:

$$v_{sc}[\mathrm{x}+1] = N_{s,sc} v_{sc,cell}[x+1] \tag{3.18}$$

The discretized model of the buck-boost DC-DC converter of the SC can be derived as:

$$\begin{aligned} i_{L,sc}[x+1] &= \frac{T_s}{L_{sc}}\left(v_{sc}[x] - v_{dc}[x](1 - d_{sc}[x])\right) + i_{L,sc}[x] \\ i_{dc,sc}[x+1] &= i_{L,sc}[x](1 - d_{sc}[x]) \end{aligned} \tag{3.19}$$

3.2.1.2. PV Discrete Model

The PV output current in the discrete format is:

$$i_{out,pv}[x+1] = \frac{R_{p,pv}}{R_{s,pv}+R_{p,pv}}\left(i_m[x] - \frac{v_{pv}[x]N_{p,pv}}{R_{p,pv}N_{s,pv}}\right) \tag{3.20}$$

Other related parameters in (3.20) can be calculated as follows:

$$\begin{aligned}
i_m[x+1] &= -i_0[x]N_{p,pv}\left[exp\left(\frac{v_{pv}[x]+\frac{R_{s,pv}N_{s,pv}}{N_{p,pv}}i_{out,pv}[x]}{v_{t,pv}[x]\times a\times N_{s,pv}}\right)-1\right] \\
&\quad + i_{pv}[x]N_{p,pv} \\
i_{pv}[x+1] &= \frac{G[x]}{G_n}\left(I_{pvn} + K_i\Delta T_{pv}[x]\right) \\
i_0[x+1] &= \frac{I_{pv,scn}+K_i\Delta T_{pv}[x]}{exp\left[v_{t,pv}[x]\left(V_{pv,ocn}+K_v\Delta T_{pv}[x]\right)-1\right]} \\
v_{t,pv}[x+1] &= \frac{k\times N_{s,cell}\times T_{pv}[x]}{q} \\
\Delta T_{pv}[x+1] &= T_{pv}[x] - T_{pv,nom}
\end{aligned} \tag{3.21}$$

The discrete model of the PV's DC-DC converter is derived as:

$$\begin{aligned}
v_{pv}[x+1] &= \frac{T_s}{C_{pv}}\left(\, i_{out,pv}[x] - i_{L,pv}[x]\right) + v_{pv}[x] \\
i_{L,pv}[x+1] &= \frac{T_s}{L_{pv}}\left(v_{pv}[x] - v_{dc}[x]\left(1-d_{pv}[x]\right)\right) + i_{L,pv}[x] \\
i_{dc,pv}[x+1] &= i_{L,pv}[x]\left(1-d_{pv}[x]\right)
\end{aligned} \tag{3.22}$$

3.2.1.3. Grid-Connected Inverter Discrete Model

The discrete model of the grid-connected inverter can be presented as:

$$\begin{aligned}
i_d[x+1] &= \frac{T_s}{L_f}\left(v_{dc}[x]d_{inv,d}[x] - v_{t,d}[x] + \omega L_f i_q[x]\right) + \, i_d[x] \\
i_q[x+1] &= \frac{T_s}{L_f}\left(v_{dc}[x]d_{inv,q}[x] - v_{t,q}[x] - \omega L_f i_d[x]\right) + \, i_q[x]
\end{aligned} \tag{3.23}$$

The DC-link voltage dynamic in discrete format is:

$$v_{dc}[x+1] = \frac{T_s}{C_{dc}}\left(i_{dc,pv}[x] + i_{dc,sc}[x] - i_{dc,inv}[x]\right) + \, v_{dc}[x] \tag{3.24}$$

The discrete format of the current from the DC side to the grid-side inverter ($i_{dc,inv}[x]$) can be calculated as follows:

$$
\begin{aligned}
i_{dc,inv}[x+1] &= \frac{1.5}{v_{dc}[x]}\left(v_{inv,d}[x]i_d[x] + v_{inv,q}[x]i_q[x]\right) \\
v_{inv,d}[x+1] &= v_{t,d}[x] + L_f\left(\frac{i_d[x+1]-i_d[x]}{T_s}\right) \\
&\quad - \omega L_f i_q[x] \\
v_{inv,q}[x+1] &= v_{t,q}[x] + L_f\left(\frac{i_q[x+1]-i_q[x]}{T_s}\right) \\
&\quad + \omega L_f i_d[x]
\end{aligned}
\tag{3.25}
$$

3.3 Experimental Verification

3.3.1 PVSS Emulator Setup on HTB

The PVSS emulator is implemented on the HTB platform by using three VSCs including a generator emulator [56], a load emulator [59], and a PV combined with SC emulator as shown in Figure 3.6. All emulators connect to each other through a line inductance (L_l) on the AC side to form the system under study. This configuration enables the power flow between the emulators to be similar to the power flow between grid components in a real power system.

Because the PVSS is considered a current source, the VSC's terminal voltage ($v_{t,abc}$) is measured and used as the input of the emulator. The abc/dq transformation embedded in the DSP calculates the voltage signals in dq coordinates for the synchronous frame phase-lock loop (PLL) to estimate the angle (θ) [60] that will be later used in the PVSS model.

The PVSS model will generate the dq current references based on its operation mode, determined by the system condition received from the PLL block. The PVSS operating modes implemented in the emulator include a normal operation mode (MPP) and abnormal operation modes, where the PVSS will provide support to the grid i.e., voltage support, frequency support, and low-voltage ride-through (LVRT) operation. The inner current control loop will use these reference currents to control the real VSC's current by generating the PWM signals. This approach allows the VSC to replicate the behavior of the PVSS without having physical connections to the real SC and PV systems. The parameters used in the PVSS emulator can be found in Table 3.2.

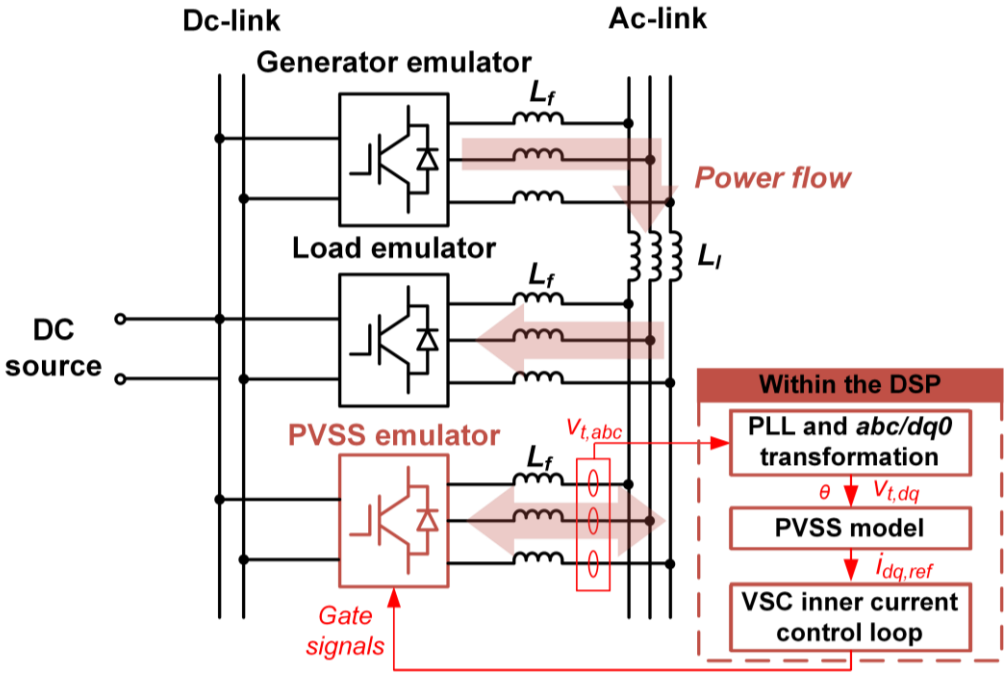

(a)

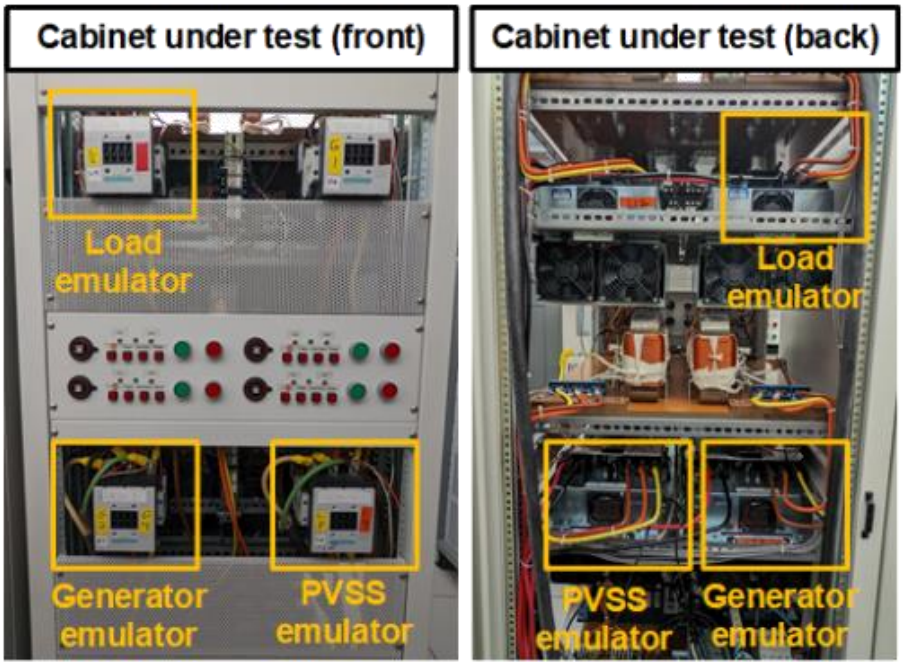

(b)

Figure 3.6: Setup of the PVSS emulator on the HTB. (a) The configuration of the PVSS on the HTB and (b) Experimental test setup of the PVSS on the HTB.

Table 3.2: PVSS's Emulator Parameters.

SC's Parameters	**Values**
Usable energy capacity	0.35 kWh
Usable power capacity	63.18 kW
Number in series ($N_{s,sc}$)	180
Number in parallel ($N_{p,sc}$)	1
Voltage rating ($v_{sc,rating}$)	486 V
Zubieta SC model [14]	R_0= 0.32232 mΩ, R_1= 0.38065 Ω, R_2= 1.3284 Ω, R_{lk}= 59.436 kΩ, C_0= 2934.7 F, C_{01}= 130.8 F, C_1= 76.841 F, C_2= 1518.8 F
DC-DC converter rating	55 kW
DC-DC converter's inductor (L_{sc})	0.4 mH
DC-link voltage PI controller	$k_{p,v}$= 1.579, $k_{i,v}$= 464.4
Current PI controller	$k_{p,i}$= 0.002396, $k_{i,i}$= 8.557
PV's Parameters	**Values**
Power rating	50 kW
Number of series-connected modules per string ($N_{s,pv}$)	10
Number of parallel strings ($N_{p,pv}$)	17
Internal parameters of the PV's module: SunPower SPR-315E-WHT-D [21]	$R_{s,pv}$= 0.43 Ω, $R_{p,pv}$ = 430.07 Ω, G_n= 1000 W/m^2 , I_{pvn}= 6.1461A, $I_{pv,scn}$= 6.14 A, $V_{pv,ocv}$= 64.6 V, $N_{s,cell}$= 96, q = 1.6022e^{-19} C, a = 0.9507, k = 1.38062e^{-23} J/K, $T_{pv,nom}$ = 298.15 K, K_i= 0.061743 $\frac{\%}{^\circ C}$, K_v= -0.2727 $\frac{\%}{^\circ C}$
DC-DC converter's inductor (L_{pv})	5 mH
DC-DC converter's input capacitor (C_{pv})	100 µF
DC-link's Parameters	**Values**
Voltage rating (v_{dc})	900 V
DC-link capacitor (C_{dc})	1500 µF
Inverter's Parameters	**Values**
Power rating	55 kW
Inductor filter (L_f)	0.5 mH
Line inductor (L_l)	2.3 mH
Outer loop active and reactive powers PI controllers	$k_{p,pq}$ = 2.871 , $k_{i,pq}$ = 57419
Inner loop currents PI controllers	$k_{p,i-dq}$ = 0.052 , $k_{i,i-dq}$ = 22.75

3.3.2 Experimental Results

The developed emulator on the HTB is verified by comparing the emulation results to the PVSS model developed in Simulink. The dynamics of the PVSS during the power system scenarios are demonstrated in the following section. Grid support functions in terms of voltage and frequency regulation are implemented in the emulator so that the PVSS dynamics under these grid support events can also be observed.

3.3.2.1. SC Model Verification

The accuracy of the Zubieta SC model adopted in the emulator is verified by comparing it with the Zubieta SC model developed in the Simulink environment.

By using the same current profile based on the discharging and charging of the SC at a constant power of 50 kW, the emulation results in terms of voltage, power, and SOC closely align the simulation results of the Zubieta model as can be seen in Figure 3.7. This ensures the SC model accuracy of the developed emulator.

3.3.2.2. Voltage Support Scenario

A grid voltage support scenario is conducted with the grid support function implemented in the emulator based on the reactive power-voltage (QV) droop curve specified in the IEEE-1547 standard [18], [51].

The PVSS provides reactive power support to the system when the grid voltage is out of its deadband. The change of the reactive power reference during the support (ΔQ_v) can be calculated as follows:

$$\Delta Q_v = k_v \Delta v \tag{3.26}$$

where the coefficient of the voltage control loop (k_v) is 14.7 and Δv is the change in voltage during the disturbance compared to the deadband of the grid voltage. The maximum reactive power for the voltage support function in the emulator is limited to 44% of the inverter's power rating according to Category II requirements in the IEEE 1547 standard [18]. However, the maximum reactive power can be set up to 100% of the inverter's power rating upon agreement with grid operators [18], especially to support severe voltage cases during faults in power grids.

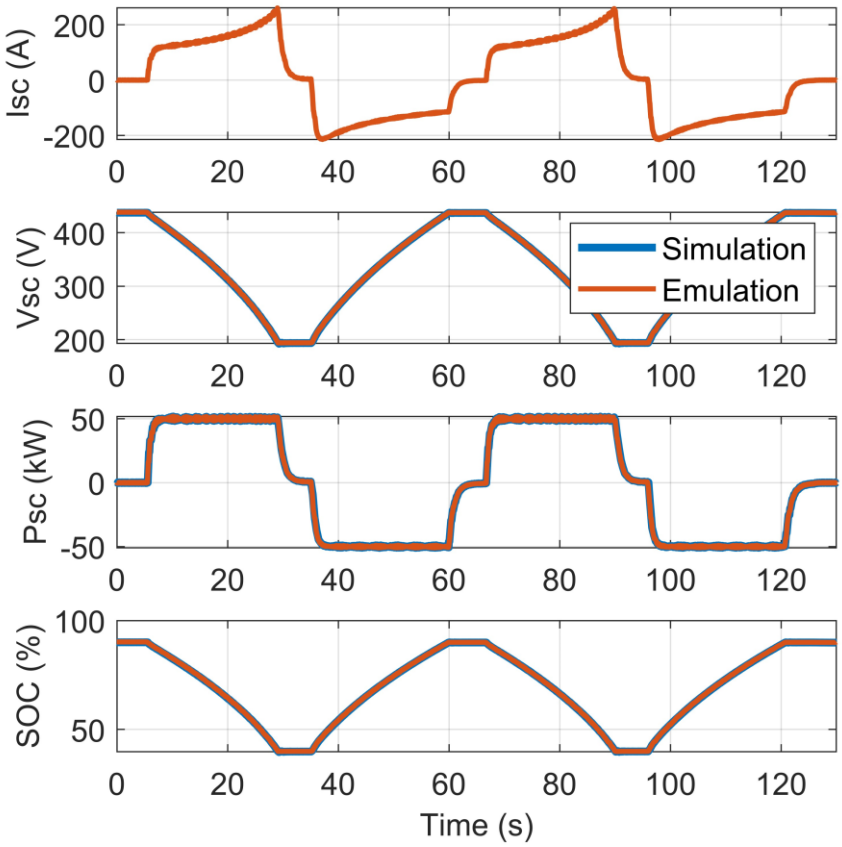

Figure 3.7: SC waveforms under constant power charge and discharge profiles.

Voltage scenarios have been performed with the results of both simulation and emulation shown in Figure 3.8(a) for the undervoltage case and (b) for the overvoltage case. At the beginning of the events, the PVSS's voltage support function is disabled and later enabled to demonstrate the voltage improvement when the PVSS provides support to the system. In both voltage scenarios, the PV operates at 50 kW according to its rating before the voltage disturbances.

For the undervoltage scenario, the voltage support of the PVSS is enabled at t = 17.4 s during the undervoltage of 0.91 pu. The PVSS provides reactive power at 0.44 pu of its rating, while the SC absorbs PV power at 600 W to make room for the inverter to provide reactive power support. The grid voltage increases to 0.94 pu during the support from the PVSS.

For the overvoltage scenario, the PVSS's operation changes from injecting the reactive power to absorbing the reactive power from the grid to reduce the grid voltage level. The grid voltage reduces from 1.08 pu to 1.06 pu during 0.44 pu of reactive power support from the PVSS.

The dynamics of simulation and emulation results for both voltage scenarios are consistent. However, the emulation results have a slower response time than the simulation due to the gradual change in the emulation's grid voltage. While the emulation runs in real-time, there are still some delays in measurement, control, and actuation [56]; making the emulation responses more realistic than the results from the simulation.

3.3.2.3. Low-Voltage Ride-Through (LVRT) Scenario

IEEE 1547 standard [18] requires DERs to stay connected to the grid and provide voltage support by adjusting their reactive power during voltage disturbances. Based on the IEEE 1547.9-2022 revision [50], DERs with storage systems shall be able to provide LVRT services based on Category III, where the voltage of the mandatory operation can be as low as 0.5 pu, and the ride-through time is up to 10 s.

Injecting the PV power during LVRT events can cause overcurrent in the inverter and overvoltage on the DC-link because the power cannot be injected to the grid. PV systems normally need to curtail their power to remain connected to the grid and provide support during the events.

To emulate the low voltage condition for the LVRT scenario on the HTB as shown in Figure 3.9, a step change of the load is applied to the system.

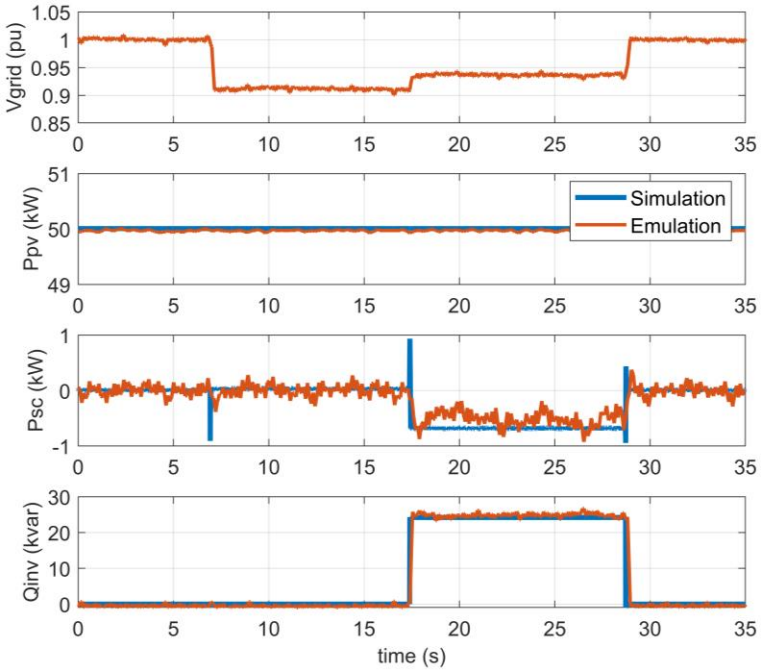

(a)

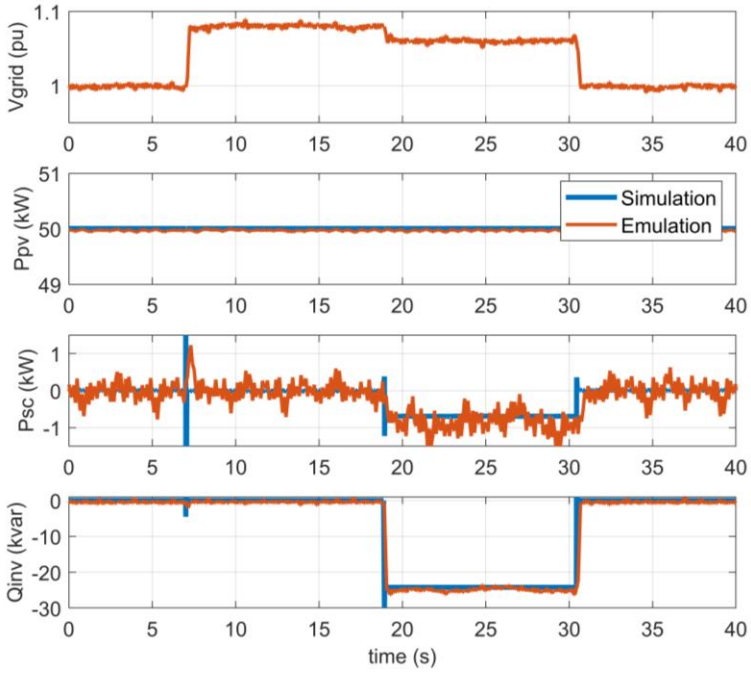

(b)

Figure 3.8: Grid voltage support scenarios emulated on HTB. (a) Undervoltage test scneario and (b) Overvoltage test scenario.

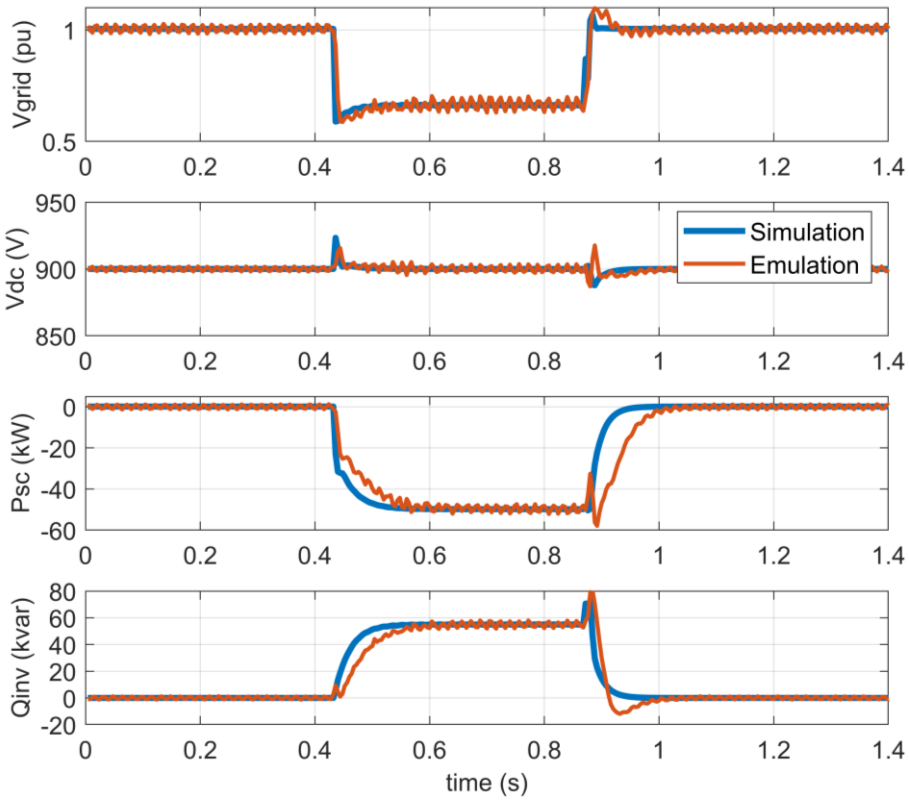

Figure 3.9: Low-voltage ride-through (LVRT) scenario.

The emulation voltage drops to 0.58 pu during the LVRT scenario if the PVSS does not provide reactive power support to the system. In this severe grid voltage scenario, the voltage support function in the PVSS emulator is adjusted to provide the maximum reactive power support at 55 kvar based on its power rating, while the PV system operates at its maximum power of 50 kW.

At the beginning of the LVRT event when the grid voltage suddenly drops to a low value, the PVSS starts ramping up its reactive power to support the grid voltage while reducing its active power injected to the grid. The emulated powers have a slower response time than the simulation due to some delays mentioned earlier, thus, their waveforms are slightly mismatched compared to the simulation. Meanwhile, the SC quickly absorbs the PV power at 50 kW to reduce the unbalanced power on the DC-link while the PV system continues its MPP operation during the event. The spikes of the DC-link voltage happen during the mode transitions between normal mode and LVRT operation; however, the DC-link voltage can be maintained at its nominal value quickly after the oscillations. The grid voltage can be improved to 0.67 pu during the reactive power support, and the PVSS can remain connected to the grid complying with the standard requirements during the LVRT operation.

3.3.2.4. Frequency support scenario

The PVSS adopts a fast frequency support function according to the standard IEEE1547.9-2022 revision [50] to provide both inertia support and frequency support to help the grid during frequency disturbances.

The PVSS needs to adjust its active power to slow down the rate of change of frequency (ROCOF) while simultaneously regulating the grid frequency as close to its nominal value as possible. The change in active power reference (ΔP_{fre}) during grid frequency support can be calculated as follows:

$$\Delta P_{fre} = k_{iner} ROCOF + k_f \Delta f \tag{3.27}$$

where Δf is the change in frequency during the disturbance compared to the deadband of the grid frequency.

The PVSS emulator adopts the moving average method to calculate the ROCOF to avoid amplifying the noise of the frequency measurement, which can occur when using the two-point

method. The moving time window of the ROCOF calculation is set to 0.5 s, which is in the range recommended by North American Electric Reliability Corporation (NERC) [49]. The coefficients of the inertia control loop (k_{iner}) and the frequency control loop (k_f) are 2 and 0.5, respectively. The inertia and frequency supports are activated based on each of their own deadbands at ±0.05 Hz/s and ±36 mHz, respectively [18].

An under-frequency event is emulated by increasing the load as demonstrated in Figure 3.10. During this scenario, the PVSS operates at 25 kW; therefore, the active power support injected to the grid during the event will come from the SC.

The emulation results when the PVSS supports the grid are consistent with the results from the simulation as shown in Figure 3.10(a). At the beginning of the frequency event, there is a sudden change in ROCOF; therefore, the SC immediately injects power to the grid to slow down the change of frequency. Then, the SC continues injecting active power to increase the frequency to be close to its nominal value as the ROCOF approaches zero.

The effectiveness of the frequency support provided by the PVSS based on the emulation is demonstrated in Figure 3.10(b). By comparing it to the case when disabling the frequency support function, the PVSS can effectively provide fast frequency support to the grid by improving the grid frequency and reducing the ROCOF of the frequency event.

On the other hand, the PV system without energy storage cannot contribute to the under-frequency event since the PV power output mainly depends on solar irradiation. Some PV systems might consider implementing PV headroom reserve control to account for the under-frequency support. However, this approach would require the PV system to operate below MPP, and it is not feasible during the nighttime or on cloudy days with no solar irradiation.

Short-term energy storage can provide flexibility to operate the system while providing support to the grid. However, due to its limited energy capacity, the design and operation will greatly impact service performance. Thus, the requirements of the grid support functions should be considered in the storage's sizing, charge management [43], and coordinated control with other systems such as PV curtailment control when the storage is unavailable.

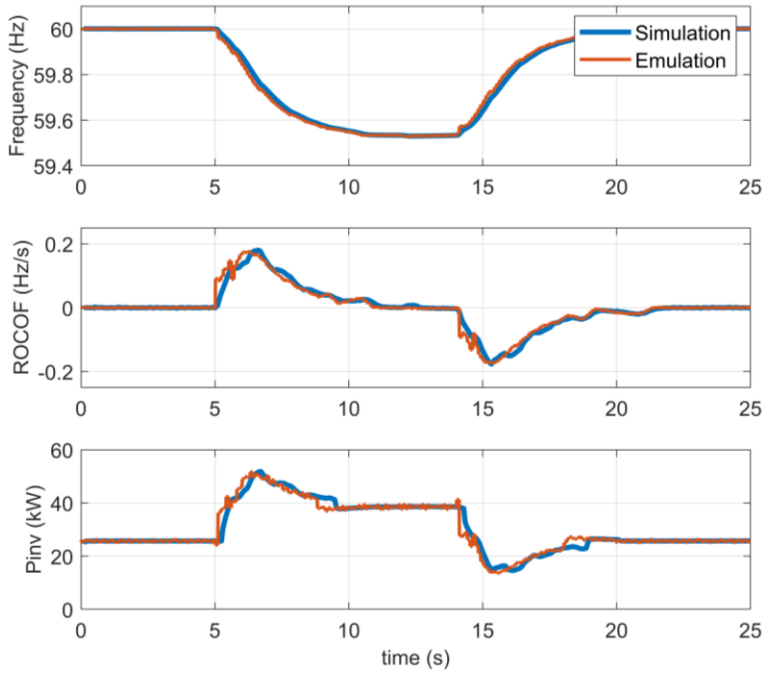

(a)

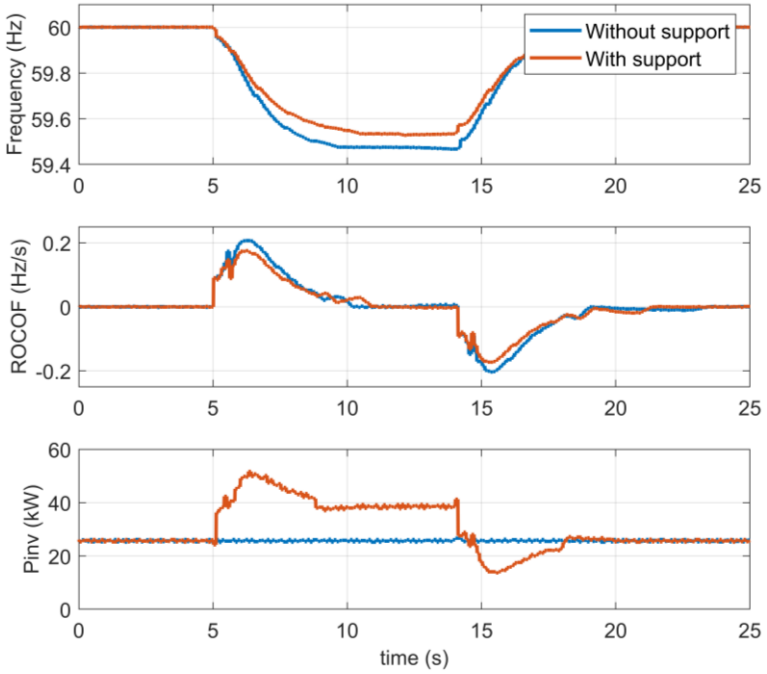

(b)

Figure 3.10: Grid under frequency support scenarios. (a) Emulation and simulation results during under-frequency support scenario and (b) Emulation results when providing frequency support compared to the case without frequency support.

3.3.2.5. Comparison of SC Models under Power System Scenarios

This section provides comparison results of SC models under power system scenarios. The SC dynamics will be compared between the Zubieta SC model and the simple SC models represented by series RC components as shown in Figure 3.11, and its parameters can be found in Table 3.3. The parameters used in both SC models are provided by [46], where the parameters are the results from the experiment of the BCAP 3000 cell.

The scenarios are emulated on the HTB, including SC charging and discharging at constant current, LVRT operation, and frequency events. The dynamic results of both SC models during the events are provided and discussed below.

- Constant current charging and discharging

In this scenario as shown Figure 3.12, the SC is being charged and discharged over time at a constant current of 100 A.

Figure 3.12(a) shows the test results from [90] when comparing the experiment results of BCAP3000 with several models, including RC and Zubieta models (which is called "2P" in the literature. These results are used as a reference to confirm the accuracy of the SC models employed on the HTB, in which the emulation results are shown in Figure 3.12(b).

The current test profile used in Figure 3.12(b) consists of discharging SC for 20 s, charging SC for 20 s, and rest time of 5 s between the discharging and charging operations. Both SC models have the initial SOC at 50 %. In the few cycles of charging and discharging, the two models have slightly different voltages. However, the voltage difference between the two models increases over time, as can be seen from the error shown in Figure 3.12(b). The error is calculated from the difference in voltage of the RC model compared to the Zubieta model from the HTB emulation results. Ref. [90] shows a similar trend of voltage difference between the RC model and the Zubieta model ("2P"). In this case, the error of the RC from [90] is calculated from the voltage difference between the RC model simulation result and the actual testing results of the BCAP3000 cell. The RC model's error from [90] is increasing over time, which is aligned with the comparison results between the RC and Zubieta models from the emulation on the HTB.

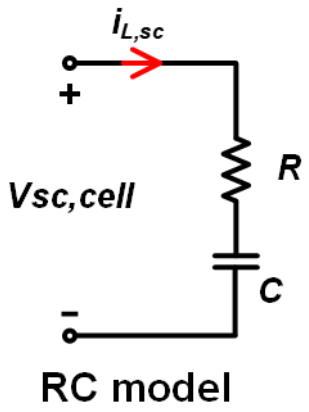

Figure 3.11: RC series SC model.

Table 3.3: RC series SC model Parameters [46].

RC series SC model Parameters	**Values**
R	0.414 mΩ
C	3139.3 F

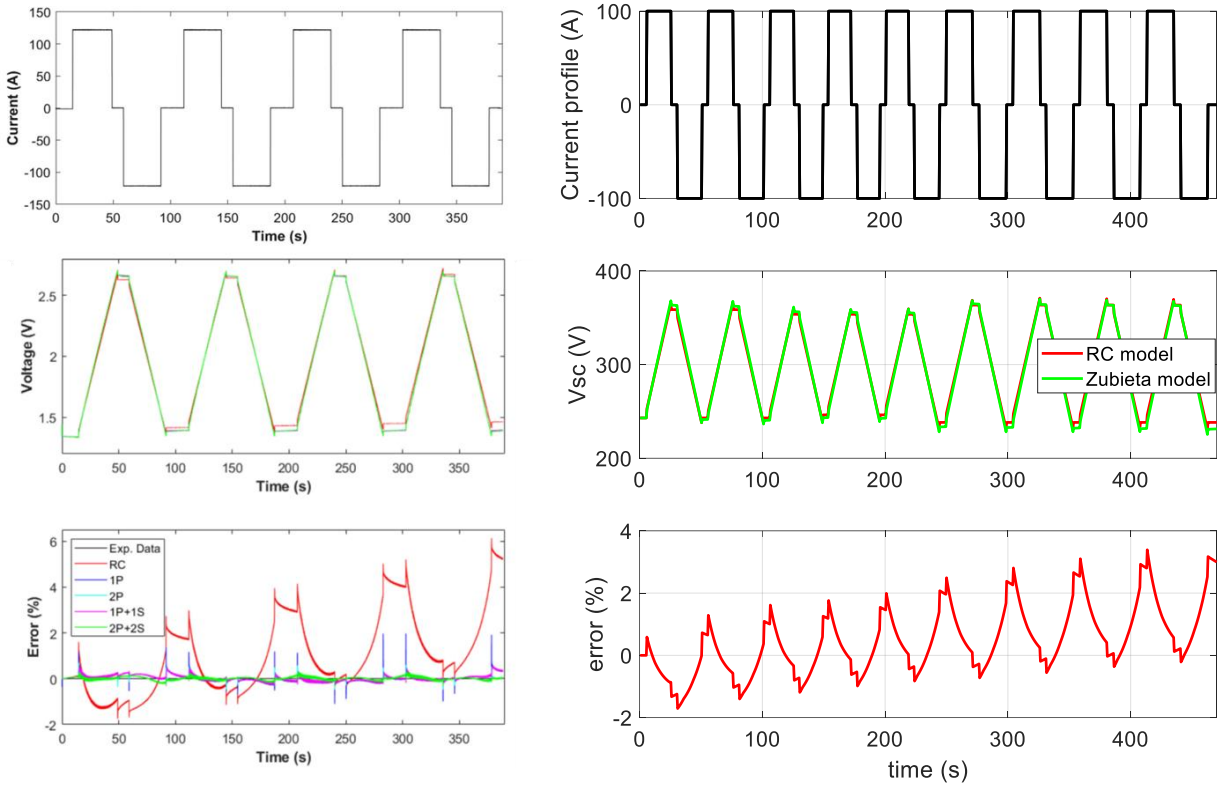

(a) (b)

Figure 3.12: Dynamics of SC models based on the constant current charge and discharge profile. (a) Comparison results from [90] and (b) Comparison results from the HTB emulation.

Since the RC model uses just two RC parameters that can only represent the SC dynamic behavior under the limited time range based on its time constant, its accuracy is reduced over time. Moreover, the RC model does not consider the SC's voltage-dependent characteristic, which makes the model unable to represent the SC dynamics accurately. Thus, it is not recommended to use the RC circuit when the time window of analysis is more than several minutes [90].

- LVRT operation

The SC dynamics of RC and Zubieta models are studied under LVRT operation. The consecutive faults with the event time duration of 6 s and the time between each fault of 5 s are emulated on the HTB. The SC absorbs PV power during the LVRT operations to allow the inverter to provide reactive power support to the grid.

Two SC models have equal initial SOC before the events. During the events, slight differences in voltage between the two SC models are observed over time. In the 3rd fault, the Zubieta model reaches its SOC upper limit faster than the RC model ~ 0.5 s.

- Frequency events

The SC dynamics of the two models are also observed under the frequency events as shown in Figure 3.14(a) for an under-frequency event, (b) an over-frequency event. During the under-frequency event, the SC is discharged to provide active power to reduce ROCOF and increase the grid frequency during the under-frequency event. For the over-frequency event, the SC is charged to absorb the active power from the PV and the grid to slow down the ROCOF and reduce the grid frequency during the event.

The voltage of SC models is very similar during both frequency events. For the under-frequency scenario, the Zubieta model reaches its lower SOC limit before the RC model ~ 0.1 s at the end of the event. Meanwhile, the Zubieta model reaches its upper SOC limit before the RC model around 1 s for the over-frequency scenario.

According to the comparison results between the series RC model and the Zubieta model, the SC dynamics of the two models are very close under grid support scenarios when the event is within the range of seconds. However, the models started having differences in voltage after charging and discharging the SC in the range of minutes. The simple RC model only has two components representing the SC with a single RC time constant. On the other hand, the Zubieta

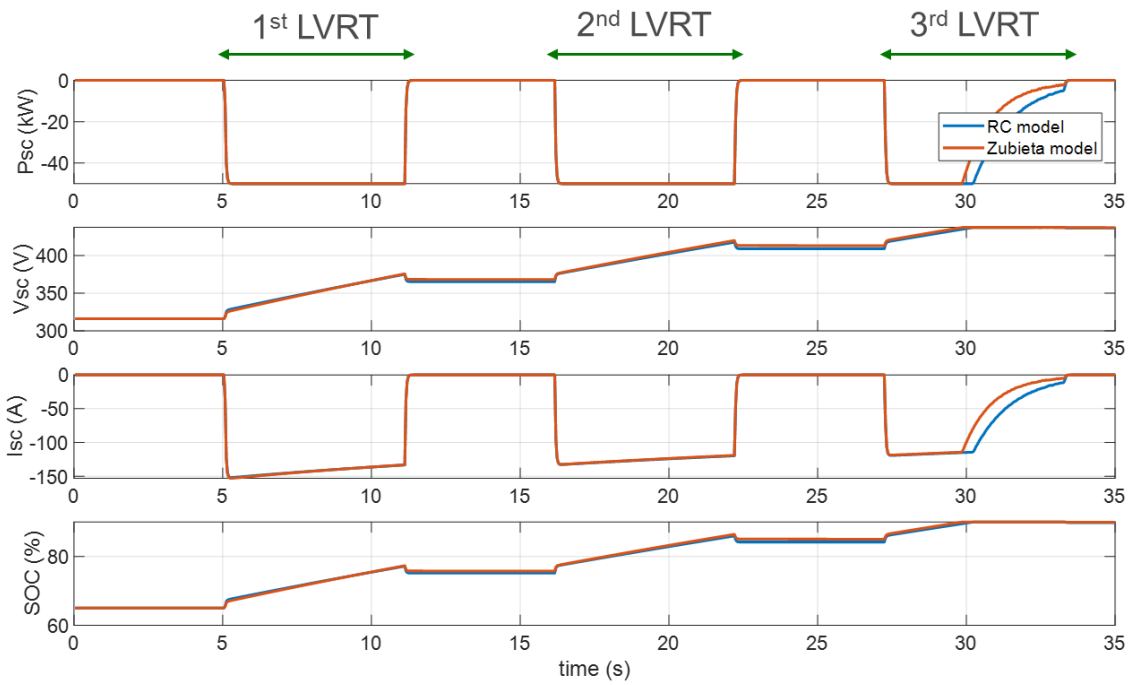

(a)

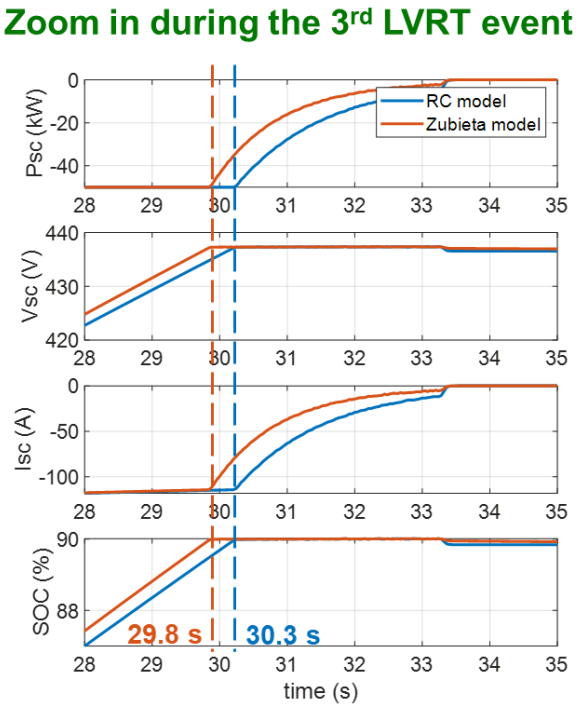

(b)

Figure 3.13: Comparison of the dynamics of SC models under LVRT operations. (a) SC dynamics under 3 consecutive LVRT operations and (b) Zoom in the SC dynamics at the end of the 3rd LVRT operation.

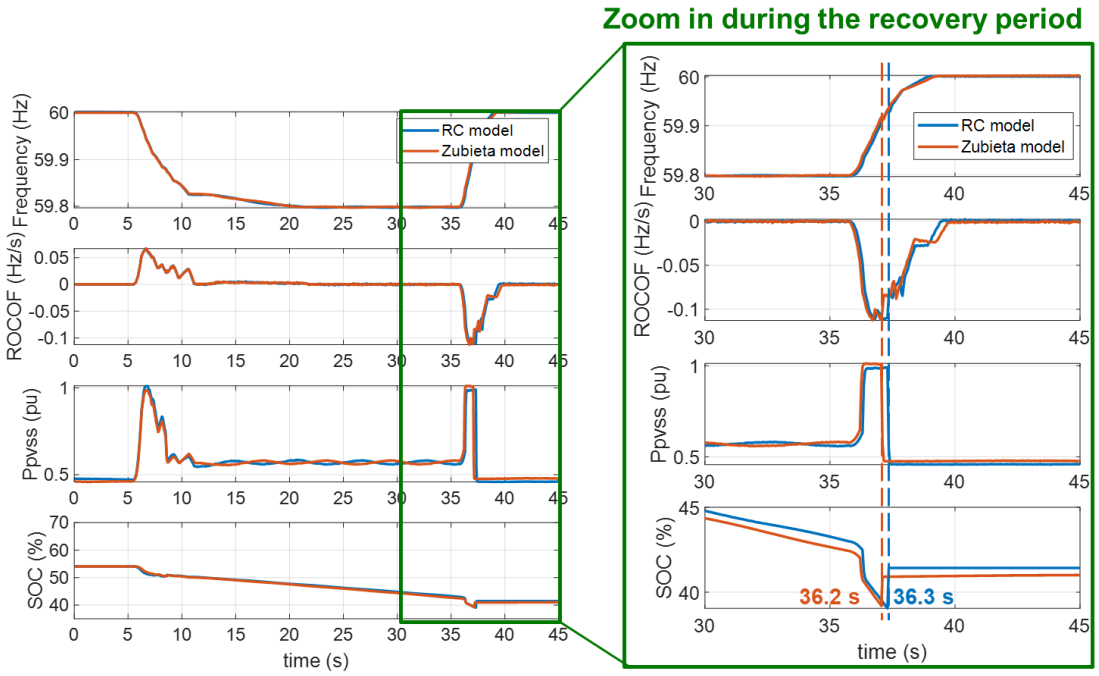

(a)

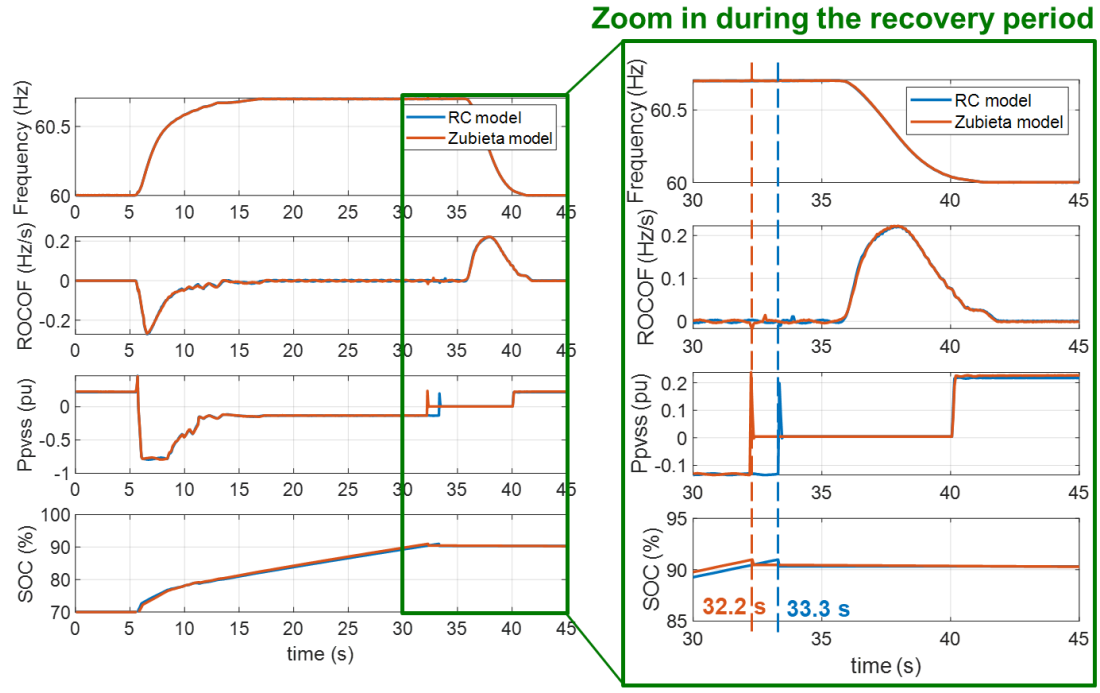

(b)

Figure 3.14: Comparison of the dynamics of SC models under grid frequency event (a) under-frequency (b) over-frequency.

model uses multiple RC components with separate RC time constant [17] to capture the SC dynamics over a wide time range.

When implementing the SC model on the HTB, the study is not limited to the grid support scenario but also considers other power system studies requiring the emulation in the range of minutes. So, the Zubieta SC model was selected to be implemented in the HTB rather than the RC model.

3.4 Conclusions

This chapter presents the development of the PVSS emulator to serve as a testing platform to accommodate the needs of power system tests related to grid-connected SC systems for PV applications on the HTB.

The Zubieta SC model is adopted in the emulator due to its compromise between complexity and accuracy. The Zubieta model can mimic the SC behavior accurately in both the short-term and long-term with a moderate computation burden. Common grid support functions, in terms of voltage, frequency, and LVRT operation are implemented in the emulator to investigate the PVSS's dynamics during the grid support scenarios. The dynamic results under grid support scenarios of the developed emulator are consistent with the results from the Simulink model, ensuring the accuracy of the developed emulator. By having the SC as an energy buffer of the PV system, the SC can effectively provide support and flexibility to operate the PV system during both normal and grid support operations. The PVSS can remain connected to the grid during severe fault conditions and provide support according to the grid's requirements.

Moreover, the developed emulator offers flexibility to test various power system scenarios, functioning both as a standalone emulator and integrated with other emulators, such as PV, wind, and battery to represent a large-scale system.

Chapter 4

State of Charge Management for Grid-Connected PV with SC System Considering LVRT Operation

This chapter introduces a state of charge (SOC) management strategy to ensure low-voltage ride-through (LVRT) services of a PVSS. A concept of SOC reservation is proposed for LVRT operations to guarantee that the grid-connected PV system can provide LVRT services complying with grid code requirements. The proposed SOC management considers several factors including the SC limitations, the current rating of the converters, and grid conditions, thereby ensuring safe operation of the power system and PVSS. Additionally, an electrothermal model of the SC is adopted to adjust the current set points during SOC management by considering the temperature-dependent SC parameters; thus, both safety and full utilization of the SC can be achieved. Consequently, SOC management can rapidly be accomplished, thereby increasing the certainty of providing LVRT services to the system.

Portions of this chapter have been previously published in the article "State of Charge Management for Grid-Connected PV with Supercapacitor System Considering LVRT Operation" that was presented at the IEEE Energy Conversion Congress and Exposition (ECCE) 2023 meeting.

4.1 SOC Management Considering LVRT Operation

During LVRT events, the PVSS is required to remain connected to the grid and provide voltage support according to the grid requirements. The SC serves as an energy buffer during such events to balance power between the PV system and the grid. However, due to the SC's limited energy capacity, there will be a case when the SC reaches its voltage limits during the LVRT event. Once its voltage limits are met, the SC is no longer able to support the PV system by providing or absorbing power. Thus, the DC-link voltage will be controlled by the inverter's controller, and the PV system may need to curtail its power generation to reduce the power that could not be injected to the grid during the low voltage conditions. During the transition, fluctuations in the DC-link voltage may occur. It can compromise the stability of the PV system, especially when the transition

happens during severe fault operations. Thus, the SOC reservation concept is introduced below to ensure that the SC has adequate capacity to support the PVSS during LVRT operations.

4.1.1 SOC Reservation Concept for LVRT Operation

SC normally absorbs or provides its power to maintain the power balance between the DC-side and grid side to regulate the DC-link voltage. During the LVRT event, the power imbalance within the PVSS (between the AC and the DC sides) tends to increase due to the low voltage condition of the grid, limiting the amount of PV power that can be injected to the grid. The SC should have sufficient capacity to support the system by absorbing the power from the PV that cannot be injected into the grid to maintain power balance within the PVSS.

To ensure the SC availability, the SOC reservation concept is proposed. It estimates the amount of SC capacity that will be used during a LVRT event, thereby reserving sufficient capacity to ensure its availability during LVRT services. The proposed SOC reservation band (SOC_{lvrt}), which indicates the estimated final value of the SOC after the LVRT event, can be calculated according to the PVSS operating conditions as follows:

$$\begin{aligned} P_{sc,lvrt} \times t_{lvrt} &= \frac{1}{2} C_{sc}\left(v_{sc,lvrt}^2 - v_{sc}^2\right) \\ SOC_{lvrt} &= SOC + \frac{(v_{sc,lvrt} - v_{sc})}{v_{sc,\text{rating}}} \end{aligned} \tag{4.1}$$

SOC_{lvrt} can be higher or lower than the current SC's SOC (SOC) depending on whether the SC will absorb or inject power during a LVRT event. The SOC reservation band is represented by the $\left(v_{sc,lvrt} - v_{sc}\right)/v_{sc,\text{rating}}$ term in (4.1). v_{sc} is the SC voltage, and $v_{sc,lvrt}$ is the estimated SC voltage after the LVRT event as determined from the calculation. The time duration (t_{lvrt}) is selected to be 5 s, which is the maximum time required for mandatory LVRT operations, based on Category II in IEEE 1547-2018 [18]. The estimated SC power ($P_{sc,lvrt}$) during LVRT operation is the unbalanced power at the DC-link between the PV output power and the critical local load's power that will be provided by the SC during the LVRT event.

When the PV generation is greater than the critical load, the SOC_{lvrt} will be higher than the SOC. This indicates that if the LVRT event happens, the SC will need to absorb the remaining PV power after supplying power to the critical load during the LVRT event. Also, the PVSS will

provide reactive power based on the available reactive power capacity to improve the grid voltage. This operation is depicted in Zone 1 in Figure 4.1.

Another PVSS operation is when the PV power is lower than the critical load as presented by Zone 2 in Figure 4.1. In this case, the SC will provide the power to support the critical load during the LVRT operation when the grid power is not available. So, the SOC_{lvrt} in this case will be lower than the SOC, which means the SC's capacity will be reduced during the LVRT event from supplying power to the load.

The SOC_{lvrt} is used to activate the SOC management to reserve the SC's capacity for supporting the PVSS during LVRT operation. An advantage of the proposed SOC reservation concept is a dynamic band according to the PVSS operating conditions, rather than assuming that the SC capacity will be used within a certain amount presented in [20] that could be larger or smaller than it should be. This avoids unnecessary SOC management that interrupts the SC operations while ensuring SC availability to support the LVRT event.

4.1.2 SOC Management Considering Grid Conditions

The SOC management is necessary to ensure the availability of the SC for operations. It involves charging or discharging the SC based on reference power to control the SC's SOC within its limits. Typically, the power reference during the SOC's management is set based on fixed power setpoints corresponding to a certain percentage of the SC's power rating [20], [62], [69]. Grid conditions are normally used to determine when to enable or disable SOC management to avoid worsening grid conditions during such operation [20], [62], [69]. The activation of the SOC management based on grid voltage conditions and fixed power can lead to issues on the grid when the grid voltage is close to its limits. The activation of the SOC management with the fixed power can push the voltage beyond its limit, and deactivation will bring the grid voltage back within limits. However, this cycle of activation and deactivation can cause oscillations of grid voltage during SOC management. Therefore, it is important to adjust the power reference setpoints based on grid conditions to mitigate these issues.

This study implements an active power-voltage (P-V) droop curve to incorporate the grid conditions while restoring the SC's SOC. The droop curve is modified from the concept presented in IEEE 1547-2018 [18] to accommodate SOC management, where the operating voltage during

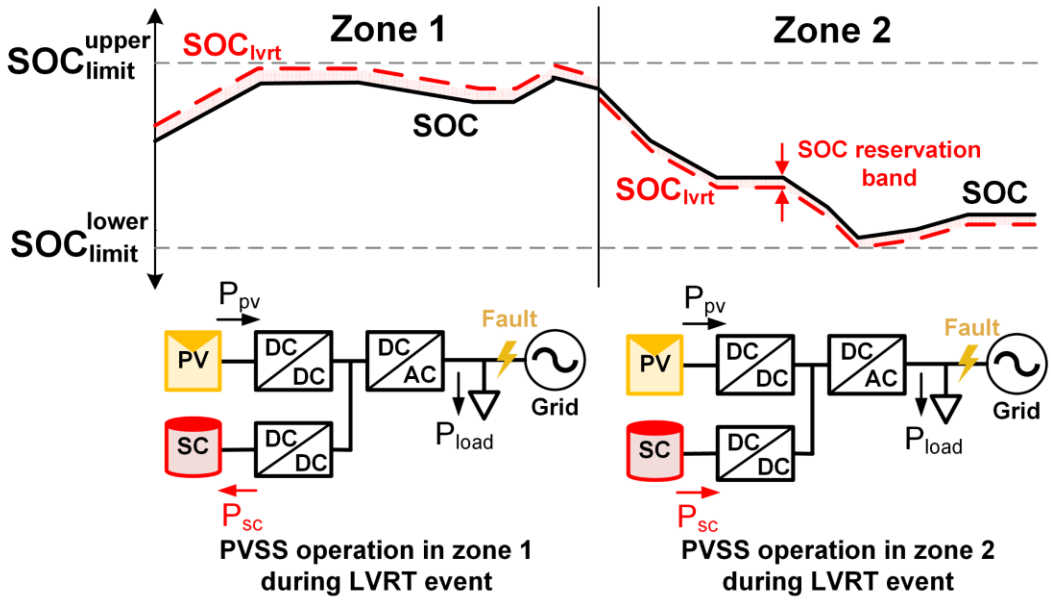

Figure 4.1: SOC reservation concept.

the management is limited within the grid voltage deadband to avoid violating the grid condition. During the SOC management when the SC is discharging (injecting power to the grid), the management power will be decreased if the grid voltage approaches the upper band at 1.05 pu. Conversely, during the SC charging (absorbing power from the grid), the management power will be reduced if the grid voltage reaches the lower band at 0.95 pu. By adjusting the power during SOC management according to the grid voltage, SOC management can be accomplished while maintaining the grid voltage within safe limits.

According to the proposed SOC management, the maximum grid-side power reference ($P_{soc,ref}^{max}$) during SOC management when considering grid conditions as shown in Figure 4.2 can be calculated as follows:

$$P_{soc,ref}^{max} = k_{vp}\left(v_{grid,lim} - v_{grid}\right) + P_{grid,int} \tag{4.2}$$

where $v_{grid,lim}$ is the grid voltage (v_{grid}) limits between 1.05 pu and 0.95 pu and $P_{grid,int}$ is the active power of PVSS before SOC management. k_{vp} is the coefficient of the active power-voltage control loop at 20, which is associated with 5% droop. Equation 4.2 is applicable only when the grid voltage is within its limits, as the SOC management will be disabled during overvoltage or undervoltage conditions in the system.

The $P_{soc,ref}^{max}$ will be used as one of the factors to determine the power reference ($P_{inv,ref}$) during the SOC management. Other factors including the SC thermal capacity, SC current, and converter's capacity will be discussed later in this chapter.

SOC management will be enabled only when the SOC_{lvrt} is outside the limits (upper limit at 90% and lower limit at 40%) and grid voltage is within the limits. The target SOC_{lvrt} value of the SOC management for this study is 65%, which is the middle of the SOC working range. This number is set by considering the equivalent possibility of the SC to be in charging or discharging modes.

4.1.3 Current Adjustment Based on SC Temperature

During the LVRT operations, the SC often absorbs the excess PV power that cannot be injected to the grid during low voltage conditions. After one LVRT operation, the SC's SOC may approach its upper limit, and the SOC management is required to discharge the SC (lower its SOC)

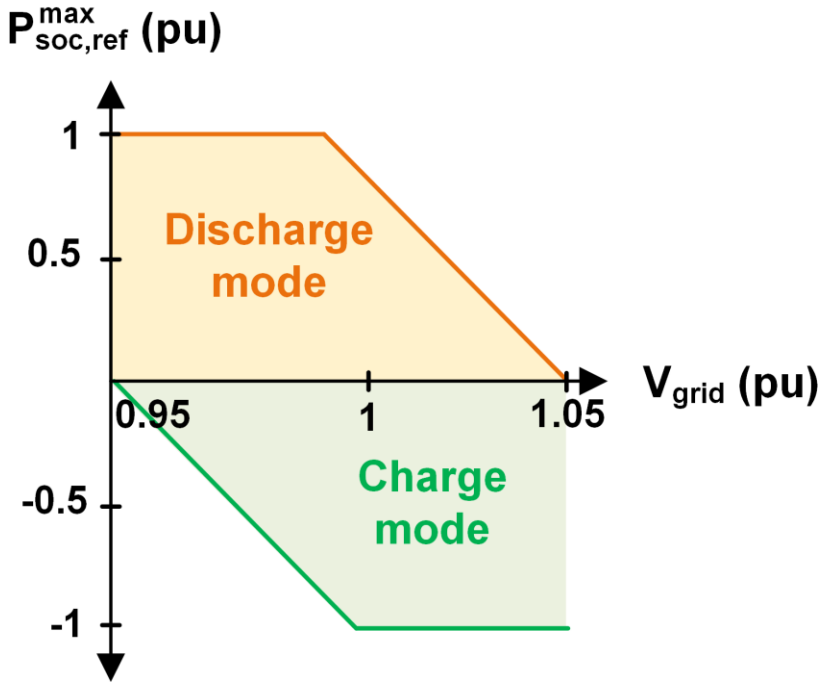

Figure 4.2: Active power-voltage curve for SOC management.

to prepare it for other operations. According to Category II of IEEE 1547-2018 requirement [18], PV systems are required to support consecutive LVRT events if the time between those two events is more than 10 s. For such operations, SOC management should quickly be accomplished (within 10 s) to ensure that the SC has sufficient capacity to support the next operation.

This study implements the adjustment of SC current based on its temperature to achieve SOC management within a short time. The models used to incorporate the SC thermal capacity into the SOC management function are presented in the sections below.

4.1.3.1. SC's Equivalent Series Resistance (R_{ESR}) Model

The SC's equivalent series resistance (R_{ESR}) is greatly impacted by the SC temperature, thus it should be properly modeled based on the operating temperature [91]. This study adopts the R_{ESR} model from [91], [92] in which the R_{ESR} of the SC cell according to its temperature (T) can be calculated as follows:

$$R_{ESR} = b_1 R_{ESR,0}\big(1 + \gamma(T - T_0)\big) + b_2 R_{ESR,0}(\exp(-0.5 k_T (T - T_0))) \quad (4.3)$$

where $R_{ESR,0}$ is 0.23 mΩ based on the temperature (T_0) at 25 ºC given in the SC datasheet [72]. The electronic (b_1) and ionic (b_2) weight factors of BCAP3000 SC cell are set to 0.55 and 0.45, respectively [91]. The coefficient of resistance sensitivity to temperature (γ) is 0.007, and the Arrhenius factor of ionic temperature dependence (k_T) is 0.045 [91], [92]. The updated R_{ESR} will increase the estimation accuracy of the SC cell temperature. Consequently, the SC current reference can be properly adjusted according to the SC temperature.

4.1.3.2. SC's Thermal Model

This study adopts the SC string thermal model [93]–[95] to estimate the SC temperature based on its operation. The SC cell temperature will be used as an input of the SC current adjustment function to adjust the SC current based on its thermal capacity so that the SOC management time can be shorter, thus the SC can be quickly ready for the next operation.

The adopted SC thermal model is an inline arrangement. This model can be simplified by assuming that the mass flow rate from one node to another is similar for all consecutive nodes [96]. Thus, the thermal network model of the SC stack for the inline arrangement can be reduced to a string thermal network [93], [96] as shown in Figure 4.3.

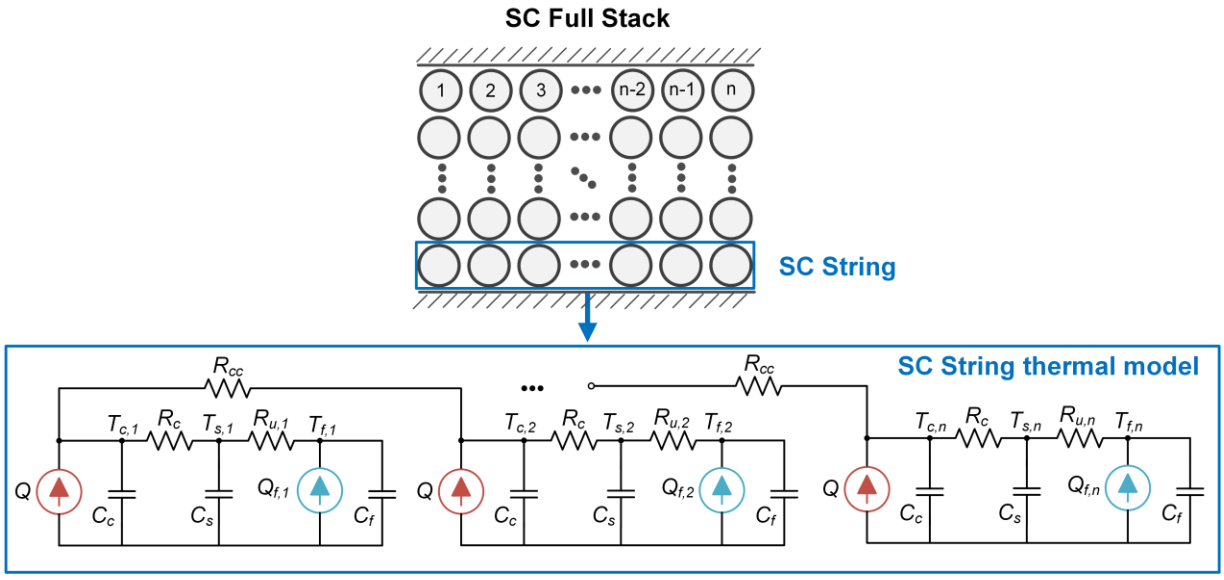

Figure 4.3: SC string thermal model [93]–[95].

The SC string thermal model is derived based on the heat balance equation of a single row of cells in the module, the SC temperatures, where there are n cells in the SC string can be calculated by using the following equation [93]–[95].

$$\begin{aligned} C_c \frac{dT_{c,n}}{dt} &= i_{L,sc}^2 R_{ESR} - \frac{(T_{c,n} - T_{s,n})}{R_c} - \frac{(T_{c,n} - T_{c,n-1})}{R_{cc}} - \frac{(T_{c,n} - T_{c,n+1})}{R_{cc}} \\ C_s \frac{dT_{s,n}}{dt} &= \frac{(T_{c,n} - T_{s,n})}{R_c} - \frac{(T_{s,n} - T_{f,n})}{R_{u,n}} \\ T_{f,n} &= T_{f,n-1} + \frac{(T_{s,n-1} - T_{f,n-1})}{R_{u,n} C_f} \end{aligned} \tag{4.4}$$

where T_c is SC cell core temperature, T_s is SC cell surface temperature, and T_f is ambient temperature, with all temperatures in Kelvin.

The heat generation (Q) for the SC string thermal model is approximated by the power loss of the SC cell caused by the current passing through the SC equivalent internal resistance, which can be represented by ($i_{L,sc}^2 R_{ESR}$) [93]. Since each SC cell is connected by a tab, the lump resistances (R_{cc}) is used to represent the tap connections [93].

The heat balance equation in (4.4) consists of two parts: the heat balance of the internal part of the SC and the outer part of the SC. The heat balance equation for the internal part includes the heat generation term and the heat transfer terms. The first heat transfer term is the heat exchange between the SC's core and its surface, which is modeled by the heat conduction over a conduction resistance (R_c) , and it is represented by $\frac{(T_{c,n} - T_{s,n})}{R_c}$ in (4.4). Other heat transfer terms for the internal part of the SC involve the heat exchange between the SC's core and tap connections to other SC cells, which are represented by $\frac{(T_{c,n} - T_{c,n-1})}{R_{cc}}$ and $\frac{(T_{c,n} - T_{c,n+1})}{R_{cc}}$ in the equation.

For heat balance equation of the outer part of the SC cell, it is modeled by the heat transfer between the SC core and the SC surface via R_c using $\frac{(T_{c,n} - T_{s,n})}{R_c}$, and the heat transfer between the surface and ambient via a convection resistance (R_u) [95], which is represented by $\frac{(T_{s,n} - T_{f,n})}{R_{u,n}}$. $T_{f,n}$ at the nth cell can be calculated by the heat balance equation related to the heat flow [93]; where the generated heat at the ambient node ($Q_{f,n}$) is the summation of the heat taken from the ($n-1$)th cell by the convection and the heat transferred from the previous ambient node ($Q_{f,n-1}$).

R_u is greatly affected by the airflow pattern, turbulence, and velocity [93]; thus, their values vary based on the cell's location with respect to the airflow source. Since the kinetic energy of the airflow will eventually reach the steady value in one location, the cells starting from that location will have a similar R_u [93]. Additional details of the thermal mode implemented in this study can be found in [93]–[95]. Other parameters in (4.4) are referred from [93], [94], [96], and their values are provided in Table 4.1.

The airflow of the SC string thermal model is from the SC cell number $n-1$ to n. Thus, the SC cell with the highest temperature will be the last one in the SC string since it's the farthest from the airflow source.

4.1.3.3. SC Current Adjustment based on SC's Temperature

Due to the need for quick SOC management, higher current operation is preferred to reduce the SOC management operating time. The SC can operate at a high current based on its current limit determined by the voltage and R_{ESR} as described in [73]. However, the main concern of high current operation is related to the temperature rise in the SC cell, which can lead to thermal runaway.

The study incorporates the SC cell temperature from the SC thermal model discussed in the previous section so that the SC current can be adjusted based on its thermal limitations [73] to maximize the SC capacity. The SC current reference ($I_{temp,ref}$) when considering the SC thermal capacity can be calculated as follows [73]:

$$I_{temp,ref} = \frac{T_{max} \times \sqrt{\frac{\Delta T}{R_{ESR} \times R_{u,sc}}}}{T_{sc}} \tag{4.5}$$

where T_{sc} and R_u are the temperature of the last SC cell in the SC string thermal model and its convection thermal resistance. Because the inline arrangement of the SC string with the airflow direction from the first cell to the last cell, the last SC cell will have the highest temperature. T_{max} is the maximum allowable SC cell temperature provided in the SC datasheet. ΔT is the difference between T_{max} and the ambient temperature. The power reference during the SOC management can be determined by using Algorithm 1, which incorporates the thermal capacity of the SC, grid conditions, and the limits of the PVSS's converters presented in the above sections.

Table 4.1: SC Thermal Parameters [93], [94], [96].

Parameters	Values
Cell to cell conduction resistance	R_{cc} = 21.99 KW^{-1}
Conduction thermal resistance	R_c = 0.627 KW^{-1}
Convection thermal resistance	$R_{u,1}$ to $R_{u,4}$ = 1.38 KW^{-1}
	$R_{u,5}$ to $R_{u,20}$ = 2.4 KW^{-1}
Thermal capacity corresponding to the internal elements	C_c = 700 JK^{-1}
Thermal capacity corresponding to the casing elements	C_s = 7 JK^{-1}
Cooling air heat capacity based on the cooling fan speed at 34.1 CFM	C_f = 18.45 $JK^{-1}s^{-1}$

Algorithm 1: Power reference during the SOC management

Input:

$I_{temp,ref}$: current reference according to the SC thermal capacity from (6)

v_{sc}: SC's voltage

$P_{soc,ref}^{max}$: the maximum grid-side power reference considering grid condition from (3)

Output:

$P_{inv,ref}$: the inverter's power reference during the SOC management

Procedure:

Compute $P_{sc,ref} = I_{temp,ref} v_{sc}$;

if $P_{sc,ref} > P_{sc,rating}$

$P_{sc,ref} = P_{sc,rating}$; *// limit the SC power based on its DC-DC converter rating*

end

Compute $P_{inv,ref} = P_{pv} + P_{sc,ref}$; **and** $P_{ac,avi} = \sqrt{S_{inv,rating}^2 - Q_{inv}^2}$;

if $P_{inv,ref} > P_{ac,avi}$;

$P_{inv,ref} = P_{ac,avi}$; *// limit the active power reference based on the available active power of the inverter*

end

if $P_{inv,ref} > P_{soc,ref}^{max}$

$P_{inv,ref} = P_{soc,ref}^{max}$; *// limit the active power reference of the inverter based on the maximum grid-side power reference considering grid condition*

end

4.2 Experiments of SOC Management Considering LVRT Operation

The experimental tests are performed on the HTB platform. A similar setup used in Chapter 3 for the PVSS emulator is used to test the proposed SOC management concept under the LVRT event. The short-term low voltage event when the grid voltage drops to 0.58 pu is emulated on the HTB shown in Figure 4.4 by applying the step change of the load emulator (add large load). During the LVRT operation, the PVSS provides reactive power to increase the grid voltage to 0.67 pu during the disturbance. Meanwhile, the SC quickly absorbs the PV power at 50 kW to reduce the unbalanced power on the DC-link. There are some DC-link voltage oscillations during the transition between the normal mode and LVRT operation, yet the DC-link voltage can be regulated at its nominal value due to the fast response of the SC. Thus, the PVSS can remain connected to the grid during this low-voltage event while the PV system continues its operation in the MPP mode.

4.2.1 SC Thermal Model of the PVSS Emulator

Regarding the proposed SOC management control, the SC temperature is required as input for adjusting the SC current of the PVSS emulator. Therefore, the SC thermal model presented in Section 4.1.3.2 is emulated on the HTB platform.

The emulation of the SC thermal model can significantly affect the computational efficiency of the PVSS emulator due to the extensive computational requirements of the string thermal model. The calculation of the PVSS emulator with the SC thermal model may exceed the allowable time frame of each time step, thereby affecting the overall accuracy of the emulated PVSS with the thermal system. There are multiple solutions to address the emulation of large systems, including reducing the switching frequency of the emulator and dividing the calculation into multiple subsystems [53]. Reducing the emulator's switching frequency extends the allowable calculation time. For instance, if the switching frequency is set at 5 kHz, the allowable calculation time will be 20 ms, which is longer than the 10 ms provided by the 10 kHz switching frequency currently used in the emulator. However, this approach may compromise the calculation accuracy

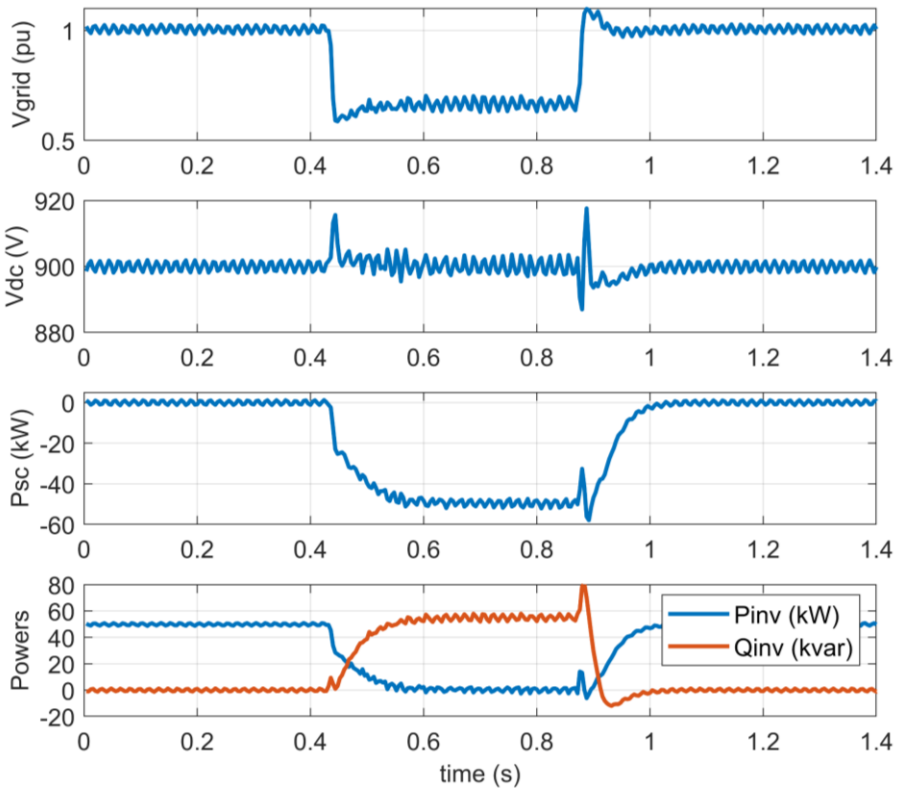

Figure 4.4: Experimental results of PVSS operation under LVRT event.

of the emulated system [97]. Another solution is to separate the emulation of the SC thermal model from the PVSS emulator. This can be achieved by using another VSC similar to the approach presented in [53] or by using the LabVIEW platform. The required data between the PVSS emulator and the SC thermal model can be exchanged over the communication that has been established on the HTB platform. In this study, the SC thermal model is emulated in the LabVIEW platform, as the SC temperature change is slow compared to the dynamic model of the SC in the emulator [98], [99]. Therefore, it is unnecessary to calculate the thermal model at every sampling period (0.0001 s) of the emulator. This ensures that the SC thermal model can be emulated without impacting the real-time emulation of the PVSS on the HTB. The thermal model in the LabVIEW is calculated every 0.01 s, and the SC temperature is updated to the emulator.

To validate the emulation accuracy, the emulation result of the SC thermal model is compared to the result obtained from the simulation. The SC current and the emulated SC cell temperatures based on the experiment are recorded while the PVSS emulator undergoes charging and discharging operations. These emulated SC current profiles are input into the SC thermal model developed in Simulink to obtain the simulated SC temperature based on the same current profiles as in the emulation.

The SC thermal model implemented in the simulation uses Simulink thermal libraries and parameters provided in Table 4.1. The SC cells depicted in Figure 4.5(a) are connected to form the string thermal network based on the inline arrangement as shown in Figure 4.5(b) and described by (4.4). The inputs of the thermal model are the power loss from the current going through the SC cell and the ambient temperature. The comparison results demonstrate that the maximum SC cell temperature obtained from the emulation closely matches the simulation result under the same charging and discharging profiles as shown in Figure 4.6. This verifies the accuracy of the SC thermal model emulation.

4.2.2 Experimental Results of SOC Reservation Concept

The performance of the SOC reservation concept is demonstrated in this section. Its effectiveness is evaluated by comparing it to the traditional SOC management for the LVRT operation proposed in [20].

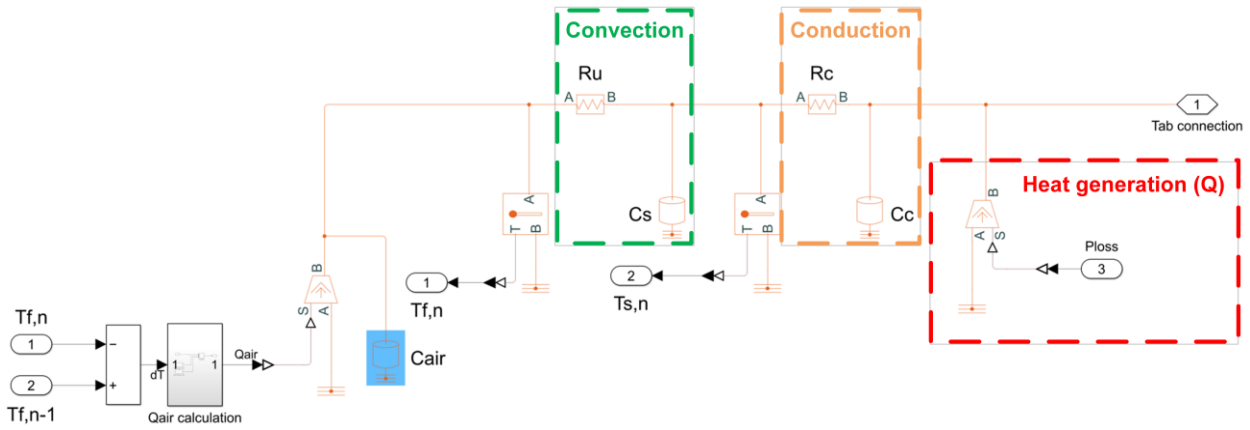

(a)

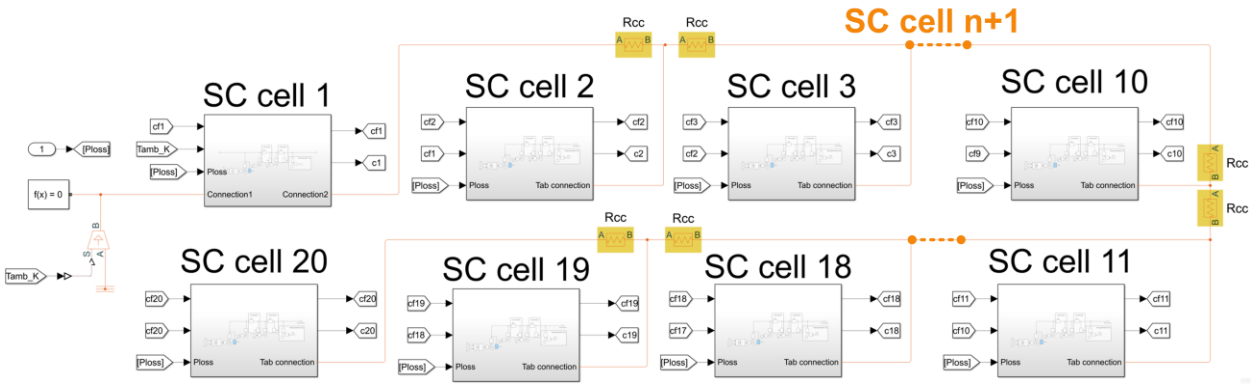

(b)

Figure 4.5: The SC thermal model in Simulink. (a) A single cell SC thermal model in the SC cell subsystem and (b) SC thermal network based on the inline arrangement.

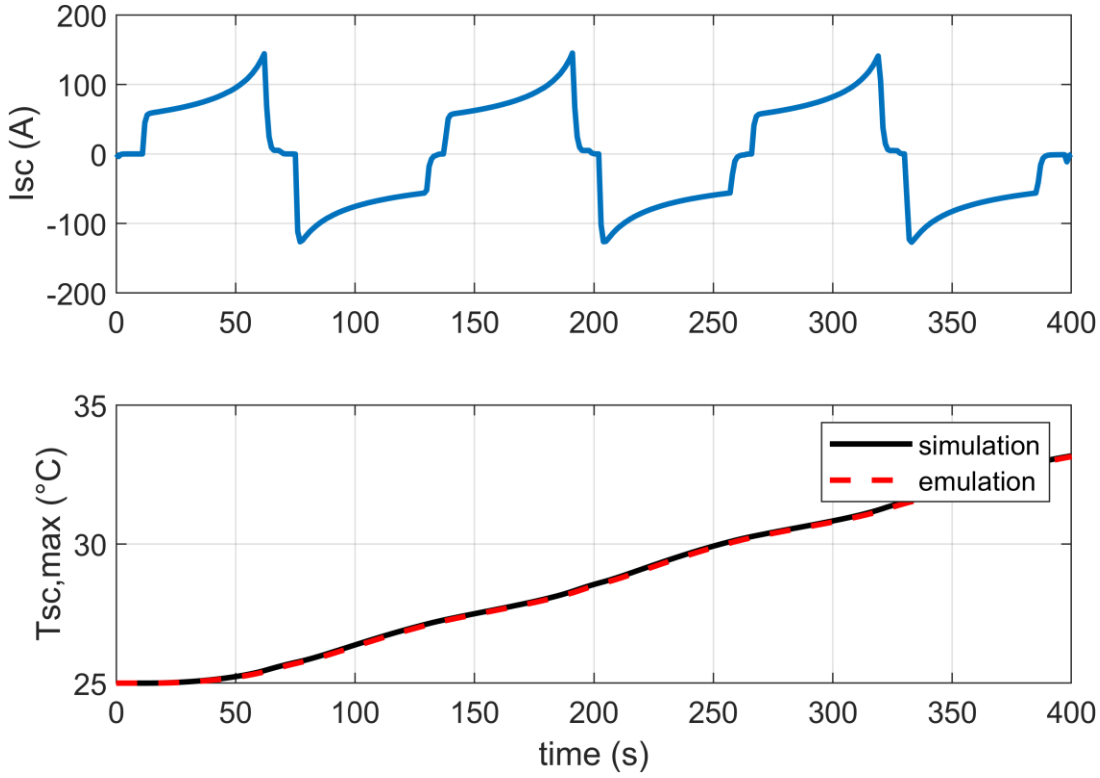

Figure 4.6: Comparison results of the SC thermal model in simulation and emulation.

For this LVRT scenario as shown in Figure 4.7, two consecutive LVRT events are emulated. The PVSS operates at 40 kW with no load and the SC's SOC is at 80% before the LVRT operations. This test represents the worst-case scenario, where the LVRT event's duration is 5 s for each operation and the time between the end of the 1st event and start of the 2nd event is 10 s.

During the 1st LVRT event, the PVSS can remain connected to the grid and provide reactive power to increase the grid voltage, complying with the grid requirements for both traditional [20] and the proposed methods. For the proposed method, the SOC after the 1st LVRT event is equal to the SOC_{lvrt} before the LVRT operation, which verified that the estimation accuracy of the SC capacity used during the event was properly reserved. After the 1st LVRT event when the grid voltage is back within its operation range, the SOC management of the proposed method is activated due to the SOC_{lvrt} is higher than its limit as shown in Figure 4.7(a). Meanwhile, the SOC management of the traditional method [20] as presented in Figure 4.7(b) is not activated because the SOC has not yet reached its limit at 90%.

The SOC management based on the proposed method is designed to stop when the SOC_{lvrt} reaches the target value at 65%. However, it is interrupted by the 2nd LVRT event that happens after the 1st LVRT operation is completed by 10 s. Since the power during the SOC management of the proposed method was maximized according to the SC thermal capacity, the SOC_{lvrt} of the proposed method was lower than 90% (the upper SOC limit) before the 2nd LVRT operation. When the reserved SOC band as indicated by the SOC_{lvrt} is lower than the SOC limit, it indicates that the SC has sufficient capacity to support the 2nd event based on the current PVSS operation. Consequently, the PVSS can remain connected to the grid, and it can provide voltage support while regulating its DC-link voltage throughout the 2nd event.

On the other hand, the SC of the traditional method reaches its limit during the 2nd LVRT event as shown in Figure 4.7(b). During the unavailability of the SC, the PV needs to curtail its power generation to zero to reduce the unbalanced power on the DC-link. Meanwhile, the grid-side inverter needs to control the DC-link voltage instead of the SC. This study adopts the PV power curtailment function from [42] in which the PV's DC-DC converter is controlled by the duty cycle according to the PV power reference during the curtailment. During the control mode transition, the DC-link voltage oscillates to 1020 V before returning to its nominal value. This DC-link overvoltage can be higher in magnitude and last for a longer time if the PV needs to curtail

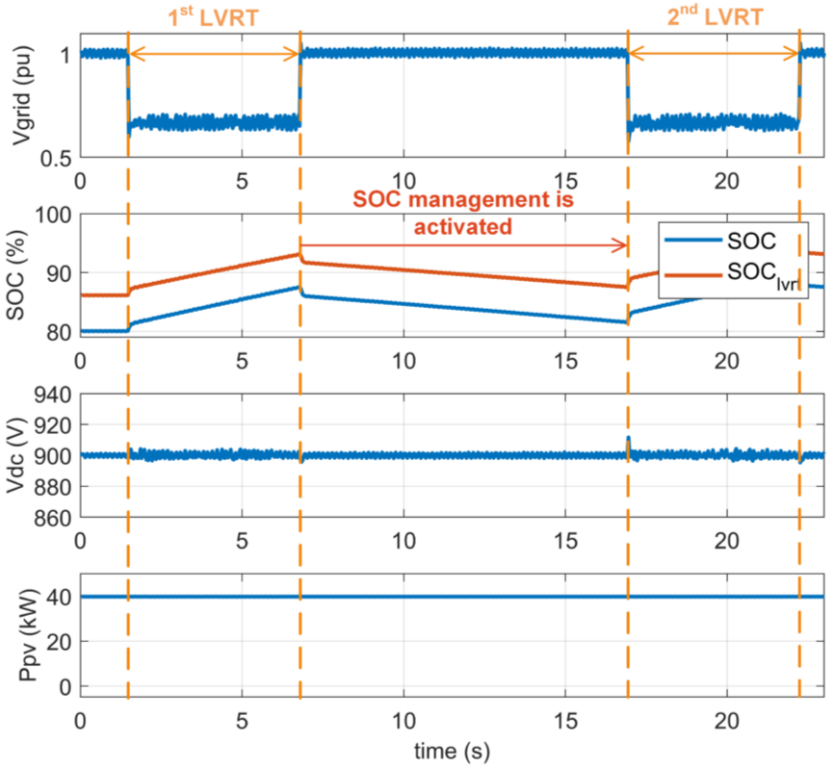

(a)

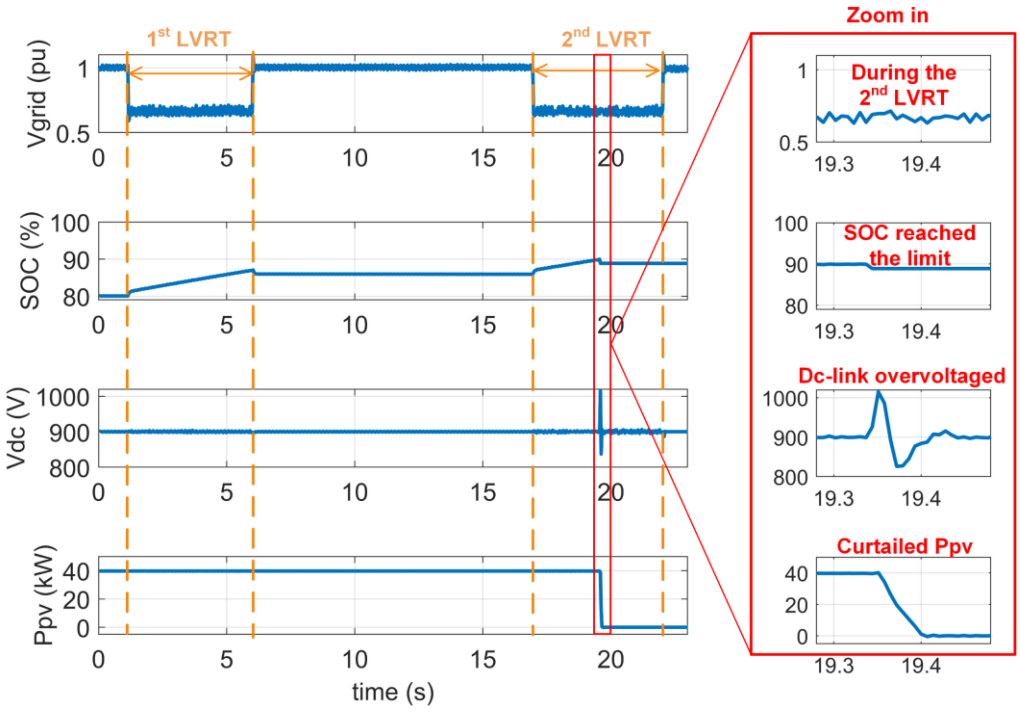

(b)

Figure 4.7: LVRT performance of the SOC reservation concept compared to the traditional control [20]. (a) Experimental results of the SOC reservation concept and (b) Experimental results of the traditional method [20].

from a higher PV power or the PV control has a slower response time than the one implemented in this study. Consequently, the PVSS's stability might be reduced, and it might lead to the disconnection of the PVSS from the grid during a severe LVRT event.

As compared to the proposed method with sufficient SC capacity during the events, the SC can maintain the PVSS's stability as verified by the seamless transition during the LVRT events without any DC-link overvoltage issues. Meanwhile, the PV can continue its MPP operation during the events.

4.2.3 Experimental Results of SC Current Adjustment Based on SC Thermal Model

This study incorporates a SC thermal model to adjust the SC current during SOC management rather than adopting the constant SC current based on the SC datasheet to shorten the management time. The comparison results of the SOC management according to these methods when charging the SC are presented in Figure 4.8.

The SC current from the model incorporating the SC temperature is higher than the limit current provided in the SC datasheet. Because the SC current is set based on the SC temperature at 25 ºC, which is relatively low compared to its upper limit of 60 ºC. Thus, the management time of the high current operation is shorter than the time when using the constant SC current. The temperature rise according to the high current operation is higher than using the constant current. However, the temperatures are not much different within the short time of the SOC management.

By incorporating the SC thermal capacity to adjust the SC operations, the tradeoff between the thermal model accuracy and the required computation time should be considered for the real-time application.

4.2.4 Experimental Results of Adjusting Power during SOC Management based on Grid Conditions

The SOC management when considering the grid condition is demonstrated in this section as shown in Figure 4.9. In this scenario, the PV operates at 25 kW, and the SC needs to inject power into the grid since the SOC_{lvrt} reaches its limit at 90%.

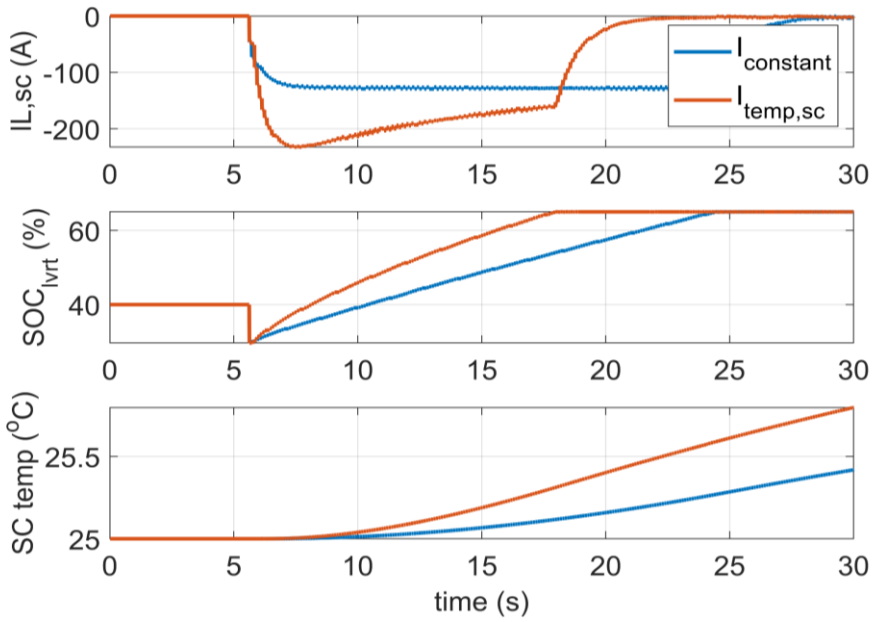

Figure 4.8: Experimental results of the SOC management based on constant current (blue) and current depending on the SC temperature (red).

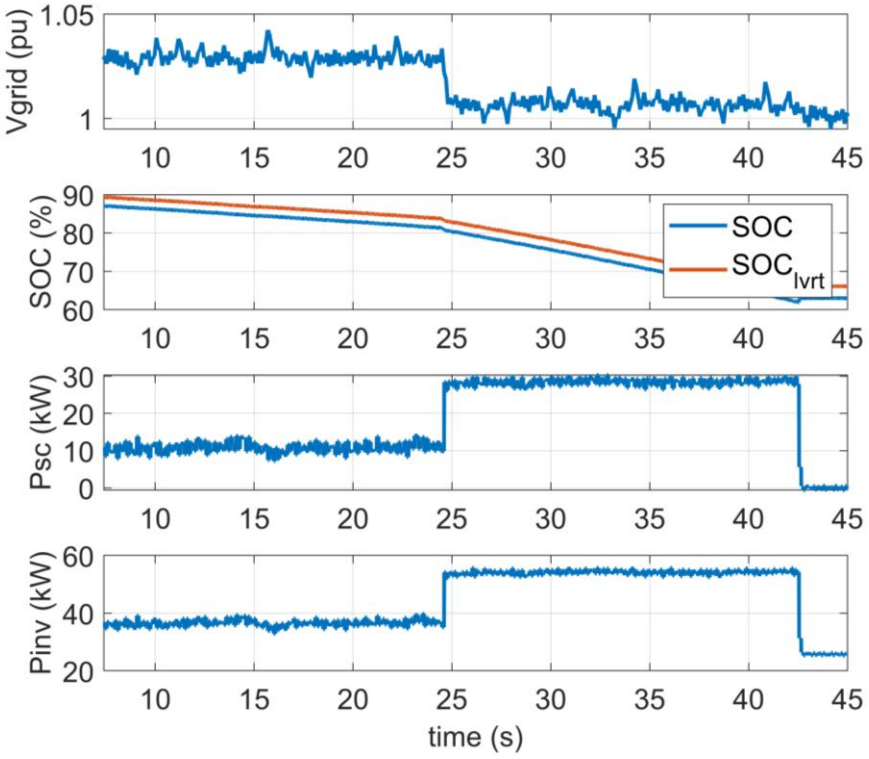

Figure 4.9: Experimental results of SOC management when considering the grid voltage condition.

At the beginning of the SOC management, the grid voltage is close to the upper boundary, thus the power during the management is adjusted to a low value to avoid violating the grid condition. After the grid voltage is reduced close to its nominal value, the injected power is increased to the full power capacity until the SOC_{lvrt} reaches the target value at 65%.

Another scenario is demonstrated where the results of the SOC management comparing the benchmark method with the proposed method are shown in Figure 4.10. The benchmark method with the traditional fixed power [20], [62], [69] is set based on its maximum power at 55 kW to quickly achieve SOC management while utilizing the disable and enable function of the SOC management based on the grid voltage conditions. Meanwhile, the proposed method adjusts the power reference during SOC management according to the grid voltage.

In this scenario, the SOC management begins at 5 s when the grid voltage is close to the boundary at 1.05 pu, and there is no PV power generation. The SC power from the proposed method is adjusted to be at a low value of 5 kW to maintain the grid voltage within the limits. Meanwhile, using a traditional fixed SC power causes power fluctuations due to disabling and enabling SOC management from the oscillation of the grid voltage at the limit. This power fluctuation worsens the grid voltage condition which can lead to the disconnection of other nearby devices in the grid due to their undervoltage or overvoltage protection settings.

The experiment results presented in this section highlight the significance of incorporating SOC management as a part of PVSS's operations. SOC management should consider both the PVSS's capacity and the power system condition so that the safe operations of both the grid and the PVSS can be accomplished.

4.3 Conclusions

During LVRT operations, a SC is used to absorb or provide power to maintain the DC-link voltage of a grid-connected PV with a supercapacitor system (PVSS). The DC-link voltage stability of PVSS can be well regulated due to the fast response of the SC. With a limited capacity of the SC, PVSS stability can be compromised if the SC reaches its limits during LVRT operations. This chapter introduces the SOC reservation concept for LVRT operations with SOC management that considers both grid and PVSS conditions. The proposed SOC reservation concept can ensure

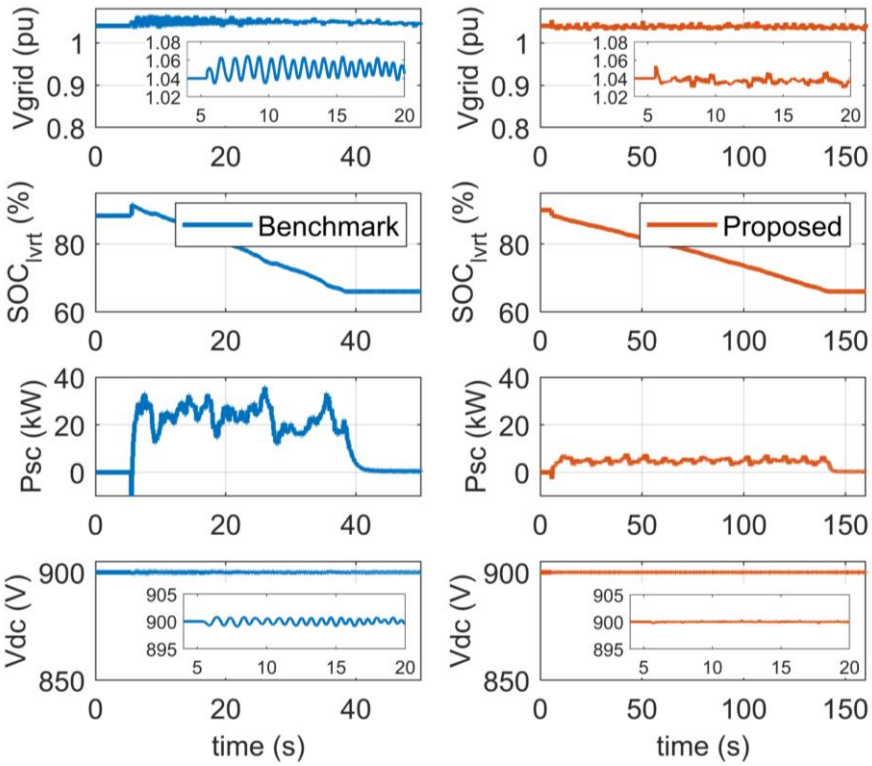

Figure 4.10: Experimental results of SOC management based on the benchmark method (blue) and the proposed method (red).

SC availability to provide LVRT services complying with grid code requirements while maintaining PVSS's stability during LVRT operations. Meanwhile, the proposed SOC management method can fully utilize the SC capacity according to its limits in terms of voltage, current, and temperature while ensuring the operation will not violate the grid conditions. Thus, SOC management can be completed faster than the existing literature with the fixed power reference during normal grid conditions.

Chapter 5

Reactive Power Allocation of Distributed Energy Resources (DERs) for Voltage Support Based on Transactive Energy (TE) Approach

This chapter presents the reactive power allocation of distributed energy resources (DERs) for voltage support in power systems by engaging the transactive energy (TE) concept. Voltage sensitivity analysis is performed to determine the impact of DERs at different locations that will simultaneously participate in a reactive power market. The modified DER's supply curve is proposed to consider the impact of a DER's location on the TE control. The performance of the proposed method is evaluated by comparing it to other location-based and non-location-based reactive power dispatch methods. The comparison results are demonstrated and discussed at the end of the chapter.

Portions of this chapter have been previously published in the article "Reactive Power Allocation of PV Inverters for Voltage Support in Power Systems Based on Transactive Energy Approach" that was presented at the IEEE Energy Conversion Congress and Exposition (ECCE) 2021 meeting.

5.1 Engaging Transactive Energy (TE) Approach to Reactive Power Support

The TE concept has been integrated into voltage support services to address voltage challenges in power systems with high DER integration as briefly introduced in Chapter 2. The TE approach aims to improve power system conditions and reliability by leveraging existing utility-owned and non-utility-owned assets. Use cases of engaging the TE concept in providing reactive power services for voltage improvement during service restoration have been presented in the literature [21], [23]. The TE approach utilizes economic incentives to dynamically balance supply and demand across the system [23]. Under this framework, the non-utility inverters can receive incentives based on their available capacity of inverters for providing reactive power to

the system, and the system operator receives system operational benefits from voltage support without the need of expensive capital investment.

In practical scenarios, DERs in different locations across the system can participate in reactive power support events. However, reactive power should not be supplied over long distances because it yields high losses in the power lines and increases transmission congestion [100], [101]. This location challenge is a main characteristic of reactive power that limits the number of potential reactive power suppliers at any location and time [101]. Therefore, the DER's location should be considered when determining reactive power dispatch based on the TE approach.

The TE algorithm consists of two components: a demand curve and a supply curve. The demand curve represents the required amount of reactive power from the system operator. The DER's supply curve represents the cost curve of the inverter when providing reactive power support to the system. This study will focus on determining the DER's supply curve from the perspective of service providers.

The traditional reactive power support when engaging the TE approach, as presented in Chapter 2, considers the available reactive power of the DER to determine its supply curve. The DER's supply curve can be categorized into two zones depending on the DER operating condition; curtailment and non-curtailment zones [102]. The curtailment zone is related to the cost of providing reactive power when the inverter needs to curtail (reduce) its active power output to supply more reactive power into the system. For the non-curtailment zone, the cost of providing reactive power support comes from the power losses in the inverter while providing reactive power in addition to providing active power. The power losses mainly consist of 1) semiconductor switching loss, 2) semiconductor conduction loss, and 3) auxiliary circuit energy consumption [81]. Figure 5.1 illustrates an example of the supply curves of three different DERs with ratings of 5, 10, and 15 kVA in partial load condition, where the curtailment begins at 3, 6, and 9 kvar, respectively. It can be seen from Figure 5.1 that the cost of providing reactive power in the non-curtailment zone of all DERs is less expensive compared to the cost in the curtailment zone.

The double auction mechanism is implemented to determine the cleared price for the required amount of reactive power [21], [23]. The market is cleared when demand and supply curves intersect, and at that point, the cost per kvarh ($/kvarh) of the amount of reactive power that the system needs is considered as the cleared price for the DERs [21], [23].

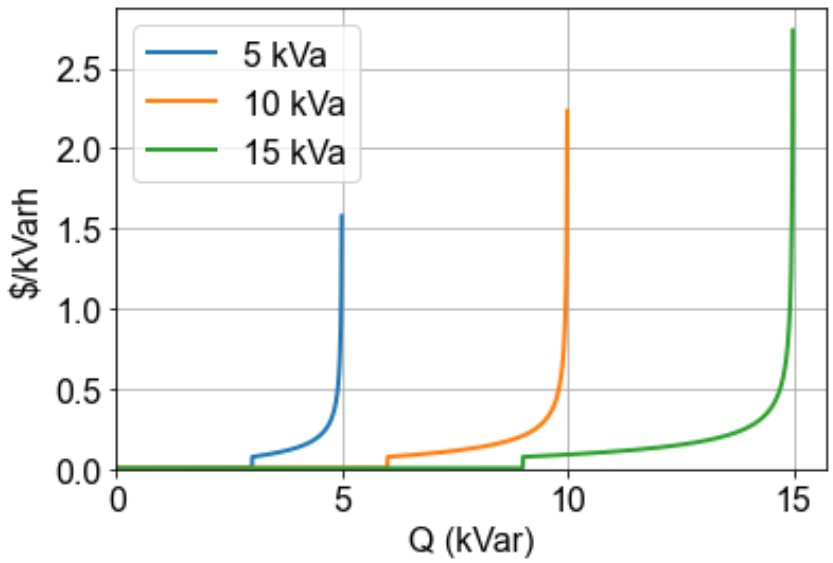

Figure 5.1: DER Supply curves of 5, 10, and 15 kVA in partial load condition.

5.2 Voltage Sensitivity Analysis for Reactive Power Support

To efficiently provide voltage support, most voltage support devices are installed close to the target location [100]. This is because voltage issues are typically considered a local problem. In the same manner, as providing voltage support from DERs, the location of the DERs should be a factor to consider when improving voltage in the system.

Voltage sensitivity analysis has been used to determine the sensitivity of the voltage based on the change of active and reactive power at different locations in the system. The analysis identifies the most effective locations and amount of reactive power from DERs to support the system [103]. There are several ways to obtain voltage sensitivity such as Jacobian matrix, impedance-based method, and perturbation method [104]–[106]. In this study, the perturbation method is implemented since it is suitable for adoption with the distributed control system [107]. The sensitivity calculation can be performed by using measurement data from the system [108]. In this study, the voltage sensitivities of DERs represent the relationship between voltage at the target location and the amount of reactive power provided by DERs based on the current state of the system [109]. These sensitivities can be obtained using the perturbation method before constructing the DER's supply curve.

The change in voltage at the target location (node *i*) with respect to the small perturbation of active or reactive power at the DERs' locations (node *j*) can be formulated as follows [110]:

$$\Delta V_i = \sum_{j=1}^{j=n} \left(S_{vp,ij} \Delta P_j + S_{vq,ij} \Delta Q_j \right) \tag{5.1}$$

where ΔV_i represents the change in voltage at node i, n is the total number of DERs in the system. S_{vp} (V/kW) and S_{vq} (V/kvar) are voltage sensitivity matrices due to the change of active power (ΔP_j) and reactive power (ΔQ_j) at node j, respectively.

A larger value of voltage sensitivity will result in a larger impact of changing voltage at the target location. For this study, it is assumed that the load in the system remains stable while applying a reactive power perturbation to calculate the voltage sensitivity.

5.3 Transactive Energy Approach Considering DER's Location

The transactive energy approach is implemented to engage the DERs to participate in the reactive power support when needed by the system. As mentioned in the previous section, the location of each DER is an important factor in determining the contribution of DER to provide the voltage support to the location. In this study, the sensitivity factors are implemented in the TE approach to evaluate the impact of voltage support based on different locations of DERs in the system. The proposed method is based on the concept of determining the cost of providing reactive power support to change a similar amount of voltage at the target location.

Each DER's supply curve will be reconstructed to incorporate the voltage sensitivity factor based on the DER's location. Given that this study is mainly focused on the change of voltage based on the reactive power output from the DERs, a relationship between the change of voltage (ΔV) at the target location (i) by reactive power contribution (ΔQ) of DERs at different locations (j) can be represented as follows:

$$\Delta V_i = S_{vq,ij} \times \Delta Q_j \tag{5.2}$$

where S_{vq} represents the reactive power sensitivity of the target location (i) and the DER's location (j).

The DERs at different locations can impact the same amount of voltage at a specific location by providing the amount of reactive power based on their voltage sensitivities. By using this relationship, the modified DER's supply curve based on curtailment cost (MC_{curt}) and cost of power loss (MC_{loss}) in terms of \$/V can be derived as follows:

$$MC_{curt} = \frac{ET \times \frac{1}{S_{vq}}\left(Q_{inv} + \frac{\Delta V}{S_{vq}}\right)}{\sqrt{S_{inv}^2 - \left(Q_{inv} + \frac{\Delta V}{S_{vq}}\right)^2}} \tag{5.3}$$

$$MC_{loss} = \frac{ET \times \frac{1}{S_{vq}} \times \left(\frac{1-\eta_2}{\eta_2}\right)\left(Q_{inv} + \frac{\Delta V}{S_{vq}}\right)}{\sqrt{P_{inv}^2 + \left(Q_{inv} + \frac{\Delta V}{S_{vq}}\right)^2}} \tag{5.4}$$

where ET is the electricity tariff at 0.1 \$/kWh, S_{inv} is the rated apparent power of the inverter, P_{inv}, Q_{inv} are the active and reactive power operating points of the inverter, respectively. η_1 and η_2 are the inverter's efficiency related to the operating point of the inverter at S_1 and S_2, respectively. S_1 is an inverter's apparent power before providing reactive power, and S_2 is an inverter's apparent power while providing reactive power support. In this study, test data of the inverters are used to determine inverter efficiency by using the curve fitting method to fit the inverter's test data to the inverter efficiency curve [111].

Normally, the DER's supply curve, which represents the cost of reactive power support of the DER, will depend on the rating of the inverter and the current operating point of the inverter in terms of active and reactive power. When considering the location of DERs, the DER's supply curve will also be impacted by the different values of voltage sensitivity. In the sections below, the modified DER's supply curve will be presented based on each impacting factor.

5.3.1 Impact of DER's Location on TE

Voltage sensitivity values of the DERs are affected by their respective locations to the target location that requires voltage support. The DER with a shorter electrical distance to a target location will have a larger value of voltage sensitivity. This implies that a change in reactive power will result in more change of voltage at the needed location compared to DERs with lower voltage sensitivity. An example is illustrated in Figure 5.2 with the modified DER supply curves of DER1 and DER2. The two DERs have similar reactive power capacities of 5 kvar and voltage sensitivities of 0.3835 and 0.3491, respectively.

According to Figure 5.2, DER1 is the closest DER to the needed location. Due to its higher voltage sensitivity, it requires less reactive power than DERs at other locations to change the same amount of voltage. Consequently, the cost of DER1 to provide reactive power support to the target location is lower than DER2 across all voltage ranges.

5.3.2 Impact of DER's Reactive Power Capacity on TE

According to the TE approach, the cost of providing reactive power increases when the DER operates close to its rating. In this case, the modified DER's supply curves of two DERs in

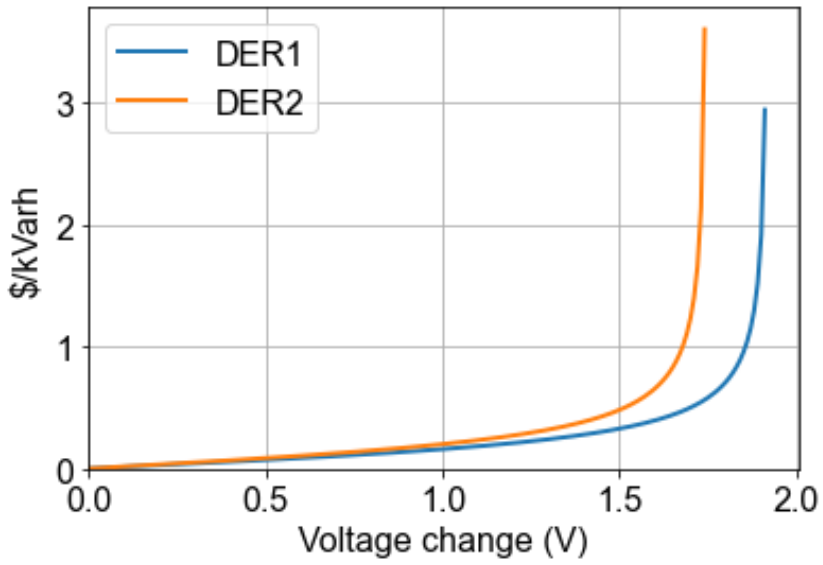

Figure 5.2: Modified DER's supply curves of DERs with similar reactive power capacities in different locations.

the same location but with different reactive power capacities are illustrated in Figure 5.3. The reactive power capacities of DER1 and DER2 are 5 kvar and 10 kvar while they have similar voltage sensitivity of 0.3835. From the modified DER's supply curves of two DERs shown in Figure 5.3, DER1 has a smaller rating resulting in a higher cost of providing reactive power than DER2 in this case.

In a real market, multiple DERs will participate in the reactive power market at the same time. The aggregate DER's supply curve of participating DERs will be used to determine the cleared price of the market. The aggregate curve is calculated by a sequence of the cost of providing reactive power of the DERs from the lowest to highest values. An example of aggregate DER's supply curve in Figure 5.4 is calculated from the individual supply curves shown in Figure 5.3.

5.4 Simulation Verification

Due to the participation of DERs in the market from multiple locations, the system will have several solutions for selecting DERs to support voltage. These inverters have different available capacities based on their operations and locations resulting in different costs of providing reactive power support to the system. Therefore, the idea of integrating the voltage sensitivity to the transactive energy approach is investigated in this section. The analysis is conducted using two different test feeders; a 15-node test feeder, as a proof of concept, and the IEEE 123-node test feeder [112] to demonstrate scalability.

5.4.1 15-Node Test Feeder

As shown in Figure 5.5, a simple 15-node test feeder with 9 DERs is used to evaluate the result of a modified DER's supply curve. Line parameters of the test feeder are taken from the IEEE 8500-node test feeder and parameters of connected DERs are provided in Table 5.1. Assuming all DERs operate based on the parameters provided in Table 5.1, the aggregate modified DER's supply curve when all DERs participate in the reactive power market is shown in Figure 5.6.

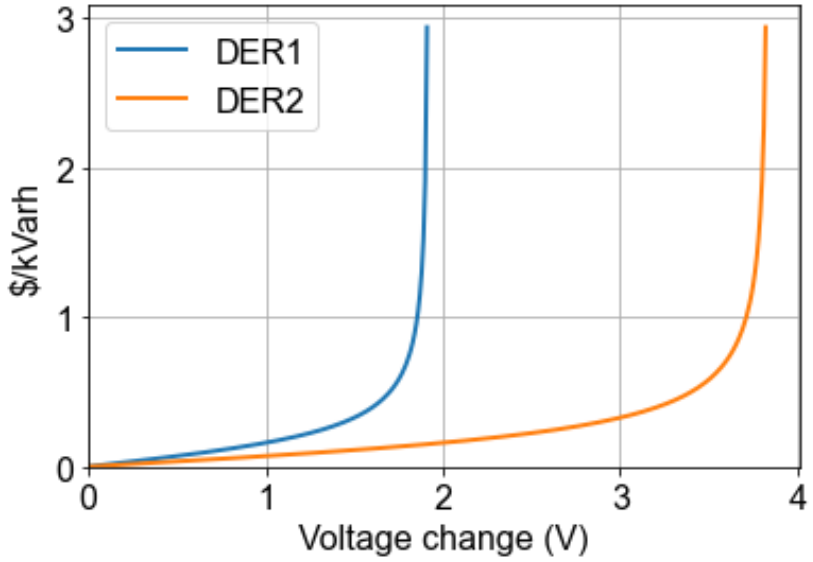

Figure 5.3: Modified DER's supply curves of DERs with different reactive power capacities in the same location.

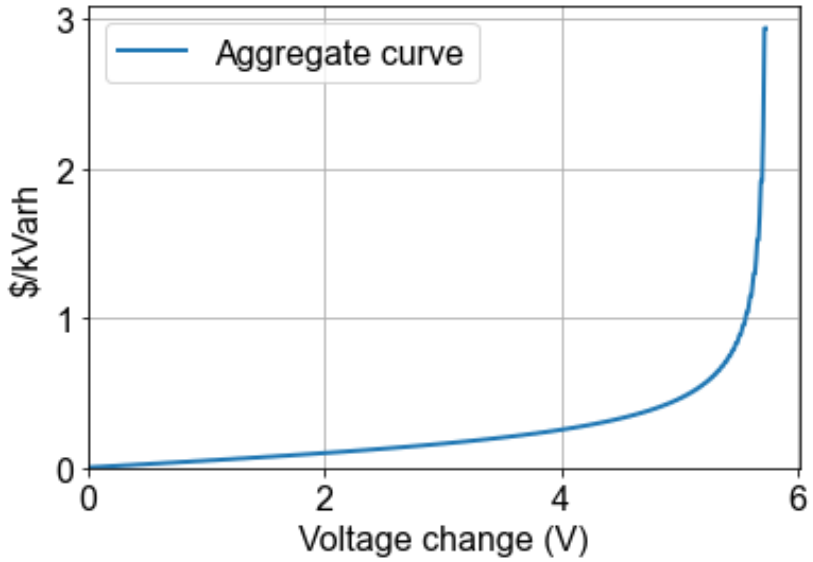

Figure 5.4: Aggregate DER's supply curve.

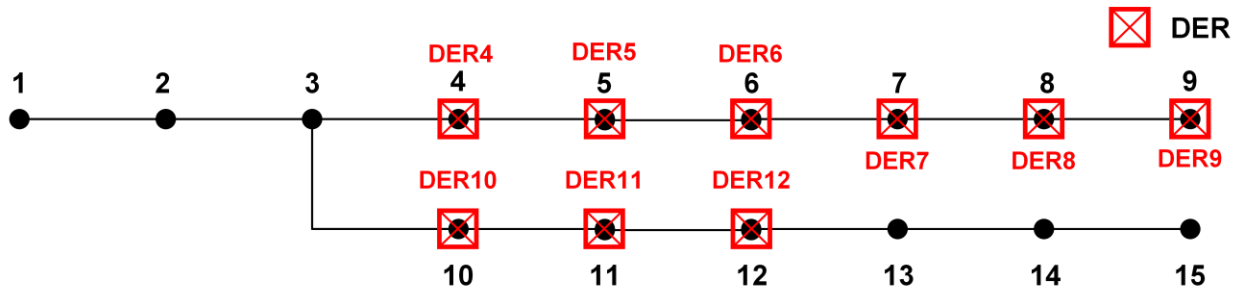

Figure 5.5: 15-Node test feeder with line parameters from the 8500-node test feeder.

Table 5.1: Parameters of 15-Node Test Feeder.

Parameters	**Values**
Rating apparent power of DERs (kVA)	5[(a)], 10[(b)]
Operating active power of DERs (kW)	4[(a)], 8[(b)]
Operating reactive power of DERs (kvar)	0
Distance between each section (km)	0.5

[(a)] For DER7, DER8 and DER9.

[(b)] For DER4, DER5, DER6, DER10, DER11, and DER12.

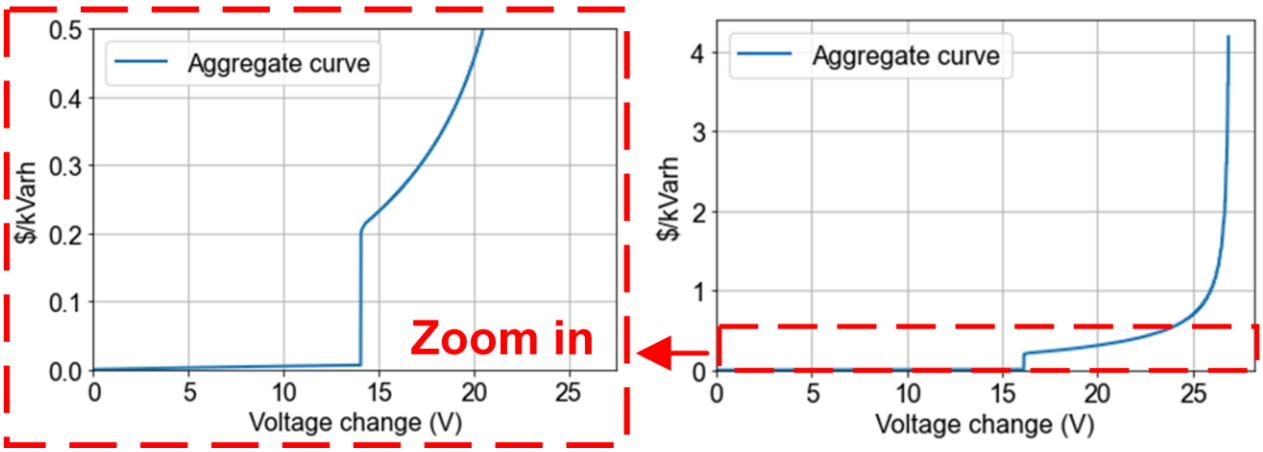

Figure 5.6: Aggregate DER's supply curve of participant DERs on the test feeder.

Assuming the system requests to change voltage at node 9 by 10 V, the cleared price of this voltage change would be 0.00475 $/kvarh. Based on this cleared price, the reactive power dispatch of the DERs and their respective voltage sensitivity values are summarized in Table 5.2.

The results of the reactive power dispatch of DERs show that the DERs closer to the target location (Node 9) will provide more reactive power (as a percentage of their available capacity) than the farther DERs. For instance, DER7, DER8, and DER9 have similar reactive power capacities, and they are at a nearby location. DER9 connected directly at the target location will provide more reactive power than DER7 and DER8 due to its higher voltage sensitivity. For other further away DERs with lower voltage sensitivities, these DERs should provide less reactive power support to avoid power losses during the reactive power dispatch in the system. However, these DERs (DER4 - DER6 and DER 10 - DER 12) provide more reactive power than the closer DERs (DER7 - DER9) because they have a lower cost of providing reactive power due to more available reactive power capacity according to their rating.

The feeder model in GridLAB-D with the dispatch of DERs based on the approach is simulated. Voltage profiles of the feeder before and after the reactive power dispatch are shown in Figure 5.7. The voltage at node 9 is changed by 10 V corresponding to the set value. Because of the small test feeder, the reactive power support at the target node affects the voltage of other nodes in the system, which can be explained by the voltage sensitivity of all nodes being very close to each other.

5.4.2 IEEE-123 Test Feeder

To examine the approach on a larger scale, a modified version of the IEEE 123-node test feeder [112] by including DERs is employed. The modified feeder includes 53 DERs connected to the nodes on the test feeder as shown in Figure 5.8. Loads are modeled as constant power loads. Although the system is three-phase unbalanced, the focus here is on one phase (phase A) to verify the performance of the approach in this study.

Voltage sensitivity analysis is applied to the test feeder to determine sensitivity factors based on the change of reactive power at different locations. For this analysis, node 114 is selected as the target location due to this node having the lowest voltage among all locations. The results of the sensitivity analysis for all DERs with respect to the target location are shown in Figure 5.9.

Table 5.2: Reactive Power Dispatch on 15-node Test Feeder.

	DER 4	**DER 5**	**DER 6**	**DER 7**	**DER 8**	**DER 9**	**DER 10**	**DER 11**	**DER 12**
Voltage sensitivity factor (S_{vq})	0.355	0.361	0.366	0.372	0.378	0.384	0.349	0.349	0.349
Reactive power (kvar)	4.20	4.30	4.37	2.23	2.28	2.32	4.12	4.12	4.12
Reactive power dispatch (%)	70	72	73	74.3	76	77.3	68.7	68.7	68.7

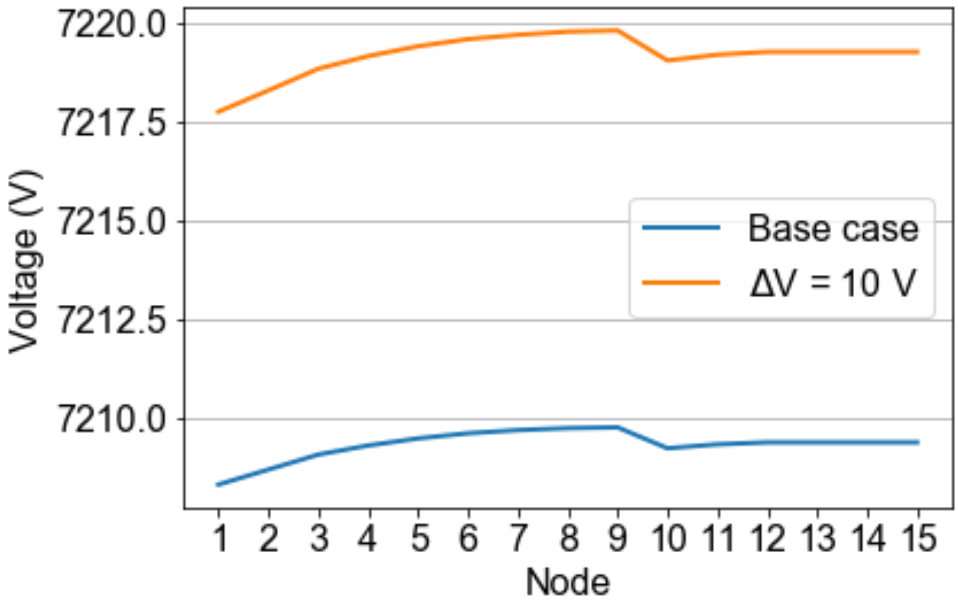

Figure 5.7: Voltage profile of the 15-node test feeder before and after reactive power dispatch.

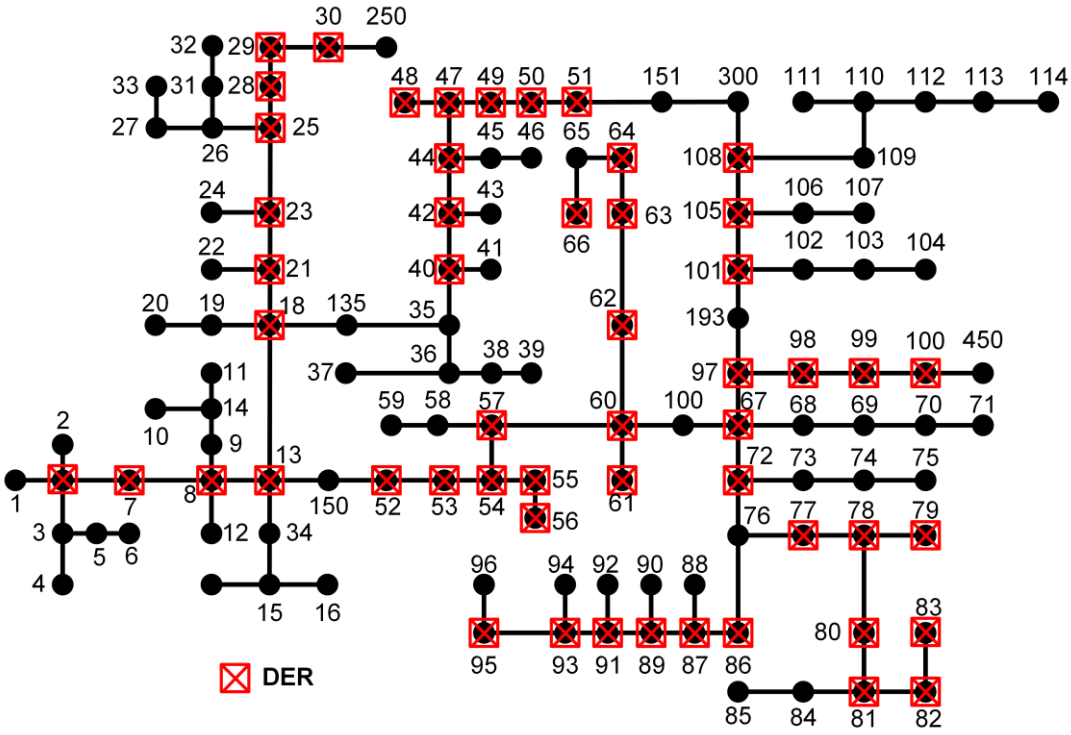

Figure 5.8: Modified IEEE-123 node test feeder with connected DERs.

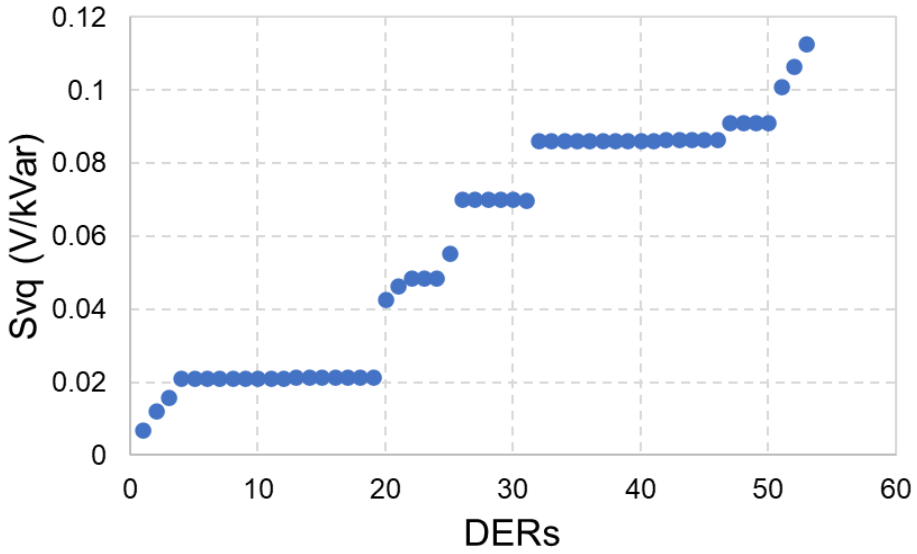

Figure 5.9: Voltage sensitivity of DERs with respect to node 114 in the IEEE-123 node test feeder.

To evaluate the proposed method, the case scenarios listed in Table 5.3 will be studied. The result of reactive power dispatch based on each scenario will be provided along with the voltage profile after the reactive power support from the DERs.

For Scenario 1, the DERs in the test feeder are assumed to operate by producing active power at 6 kW. Hence, the reactive power capacity of the DERs is at 8 kvar without curtailing the active power. The modified DERs' supply curves of all DERs are shown in Figure 5.10.

The modified DER's supply curves show that the DERs closer to the target location have a lower cost of providing reactive power than the DERs that are farther away from the target location when considering the same amount of voltage change at the same location. The aggregate curve of DERs as shown in Figure 5.11 is used to determine the cleared price of the market.

The maximum voltage at the target location can be changed based on the contribution of all DERs is at 30.6 V. Assuming the system requires to change the voltage at the target location by 20 V, the cleared price will be 0.034 $/kvarh. After the market is cleared, the reactive power dispatch of each DER is presented in Figure 5.12.

Based on the reactive power dispatch result, the DERs that are closer to the target location provide a higher amount of reactive power than the other DERs that are farther away. Since the reactive power capacity of DERs is similar at 8 kvar without active power curtailment, the DERs that have more capabilities to change the voltage at the target location with a lower price to provide reactive power support will provide more reactive power than the DERs that have less capabilities to change voltage i.e. require more reactive power to change the same amount of voltage, which results in a higher price of providing reactive power.

The voltage profile after the DERs provide reactive power support to the system is presented in Figure 5.13. Following the reactive power support from the DERs, the voltage at the target location changes by 20 V according to the system's requirement.

For Scenario 2, the DERs near the target location (DER25 – DER53) have lower reactive power capacities, rated at 5 kVA, compared to the DERs that are farther away (DER1 – DER24), rated at 10 kVA. Consequently, the price of providing reactive power support from the closer DERs to the target location will be higher than that from the farther away DERs.

Table 5.3: Parameters of DERs based on Scenarios.

Parameter	**Cases**	
	Scenario 1	***Scenario 2***
DER rating (kVA)	10	5[(a)], 10[(b)]
Current operating active power (kW)	6	3[(a)], 6[(b)]
Current operating reactive power (kvar)	0	0

[(a)] For DER25 – DER53.

[(b)] For DER1 – DER24.

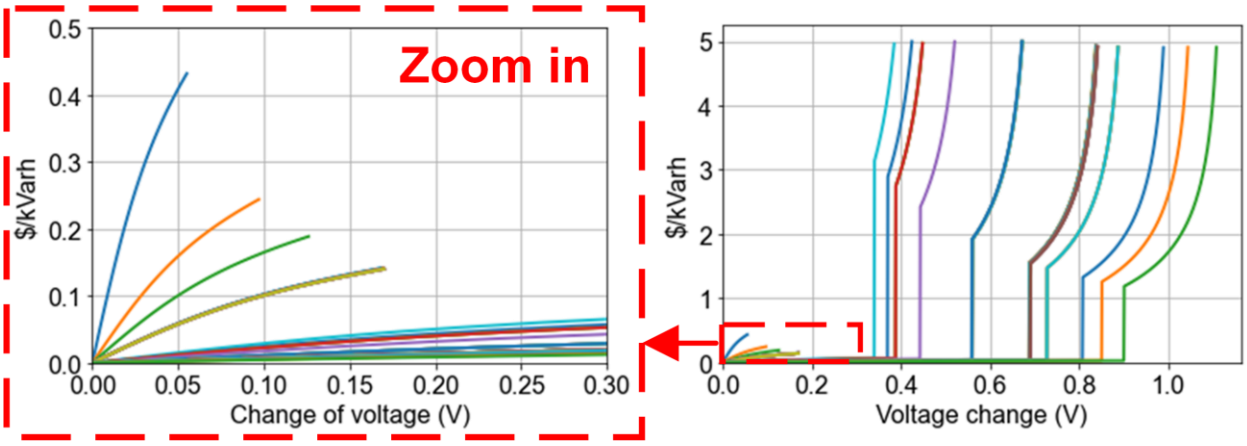

Figure 5.10: Modified DERs' supply curves of all participating DERs based on Scenario 1.

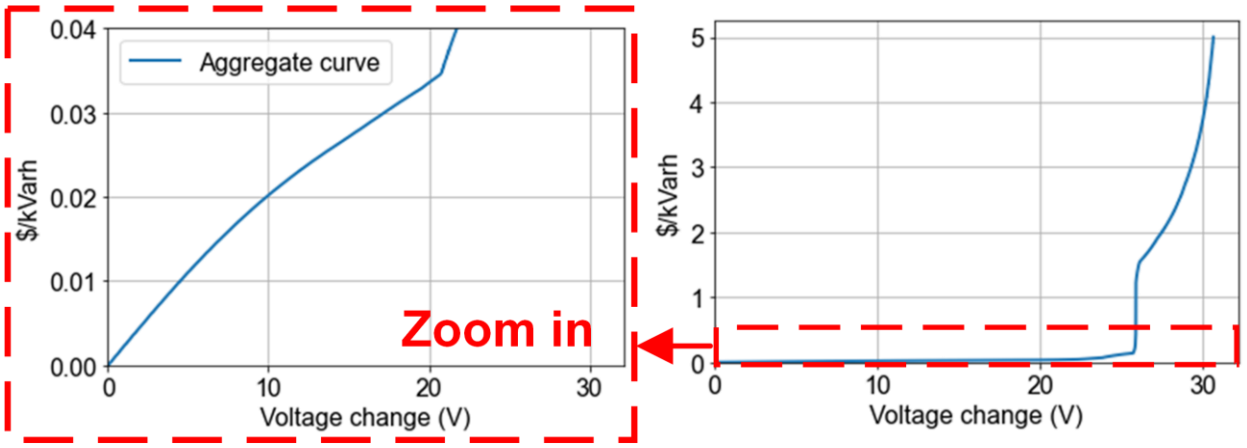

Figure 5.11: Aggregate modified DER's supply curve based on Scenario 1.

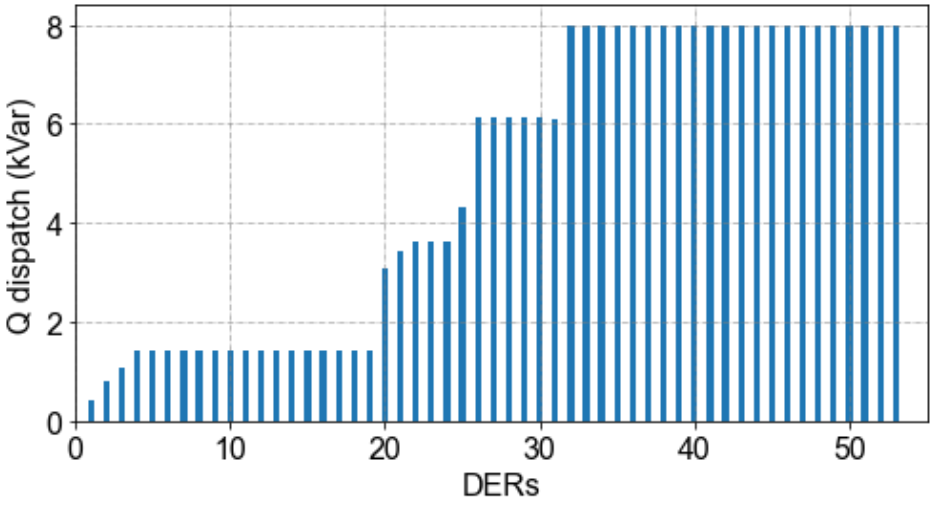

Figure 5.12: Reactive power dispatch of all DERs with similar reactive power capacities based on Scenario 1.

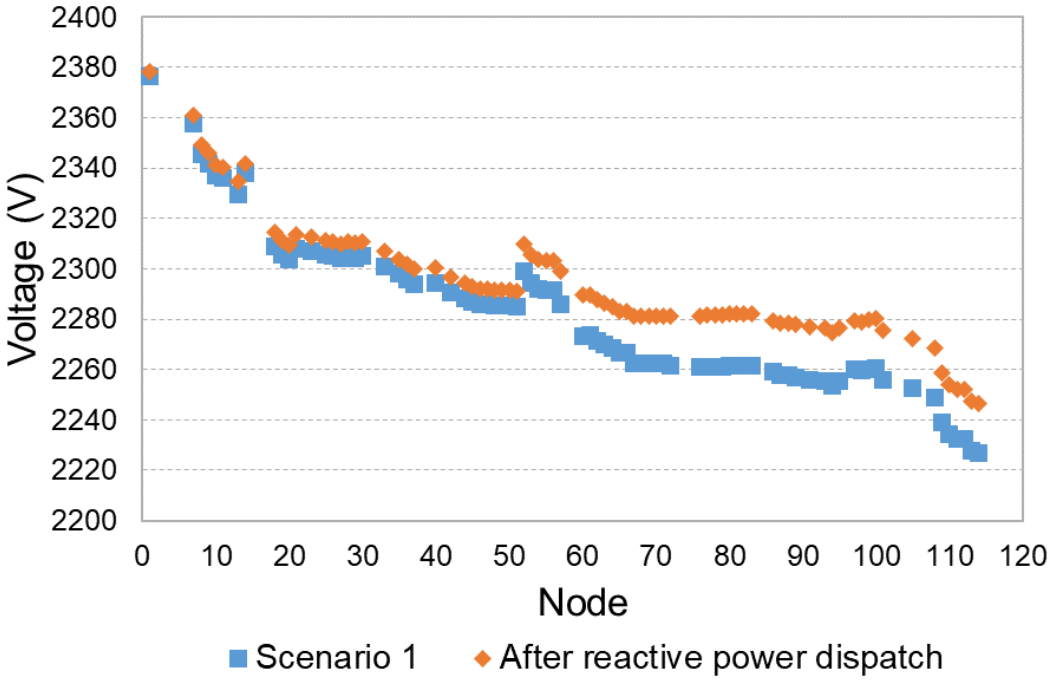

Figure 5.13: Voltage profile after the DERs provide reactive power support based on Scenario 1.

When the system requires a change of 10 V at the target location, the cleared price is at 0.032 $/kvarh. The reactive power dispatch of the DERs is presented in Figure 5.14.

In the 2nd scenario, the reactive power dispatch based on the proposed method differs from the result of dispatch based on the 1st scenario. For the 2nd scenario, the dispatch of some DERs closer to the target location (DER 25 – DER 31) is lower than that of the farther away DERs (DER 20 – DER 24). Even though the DER 20 – DER 24 must provide more reactive power than the DER 25 – DER 31 to change a similar amount of voltage, their costs of providing reactive power support are lower than the closer DERs due to their higher reactive power capacities.

Based on the reactive power dispatch of all DERs, the voltage profile of Scenario 2 is presented in Figure 5.15. The voltage at the target location increases by 10 V after the DERs provide reactive power support.

5.4.3 Comparison of Reactive Power Dispatch Methods

This section investigates the reactive power dispatch of the proposed method when compared to non-locational-based reactive power dispatch and locational-based reactive power dispatch. In the locational-based reactive power dispatch, an order of voltage sensitivity is utilized to determine the amount of reactive power provided to the system, while non-locational does not consider voltage sensitivity. The cost of DERs to provide reactive power support and losses in the system will be evaluated. The comparison will be based on Scenario 2, with similar DER parameters for each method.

To compare with non-location-based reactive power dispatch, the reactive power dispatch will be determined using the total reactive power from the proposed method. Meanwhile, for comparison with the location-based reactive power dispatch approach, the optimization method will be employed to minimize the voltage deviation at the target location when considering an order of voltage sensitivity of the DERs. The evaluation will assess the effectiveness of changing the voltage at the target location among the approaches.

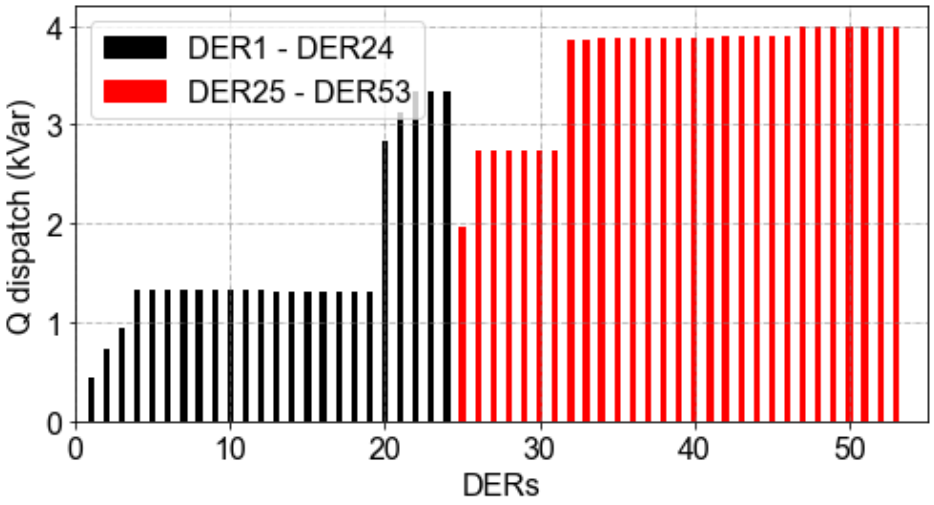

Figure 5.14: Reactive power dispatch of DERs with reactive power capacities at 8 kvar (black bar) and 4 kvar (red bar) based on scenario 2.

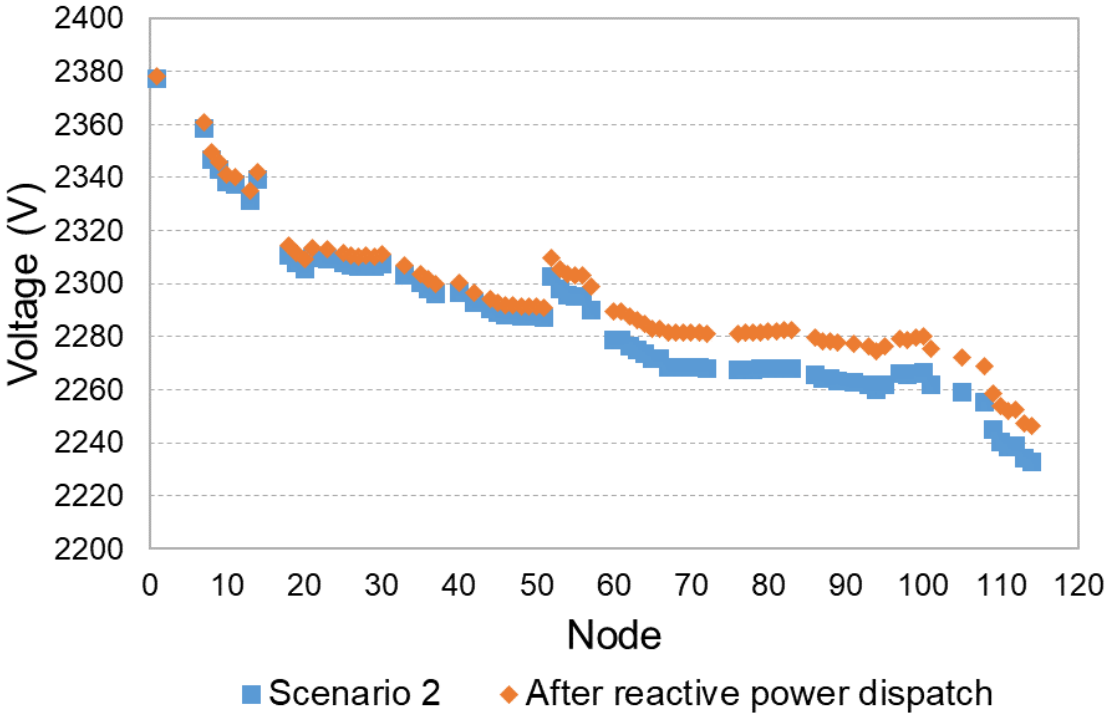

Figure 5.15: Voltage profile after the DERs provide reactive power support based on the scenario 2.

5.4.3.1. Location-based Reactive Power Dispatch: Optimization Method by Minimizing Voltage Deviation at Target Location

In this section, reactive power dispatch of the DERs will be based on the optimization approach when the objective function is to minimize the voltage deviation at the target location. The formulation of the optimization method is presented as follows:

$$Minimize\left(\Delta V_i = \sum_{j=1}^{j=n} S_{vq,ij} \times \Delta Q_j\right) \tag{5.5}$$

subject to,

$$P_{gen,j}^{min} \leq P_{gen,i} \leq P_{gen,j}^{max}, \qquad j = 1,2,\ldots,n$$

$$Q_{gen,j}^{min} \leq Q_{gen,i} \leq Q_{gen,j}^{max}, \qquad j = 1,2,\ldots,n$$

where n is the total number of DERs in the system, j is a DER's connected node, and i is a target node for voltage change.

When the system requires the participating DERs to change the voltage at the target location by 10 V, the total reactive power support needed based on the optimization approach is 137 kvar. The reactive power provided by each DER is shown in Figure 5.16. The voltage profile before and after reactive power dispatch based on the optimization approach by minimizing the voltage deviation at the target location will be provided at the end of Section 5.4.3.2.

5.4.3.2. Non-Location-based Reactive Power Dispatch

This section aims to investigate the TE approach when not considering the locations of the DERs. The rating of the inverter will be the main factor to determine the cost of DER to provide reactive power support to the system.

Based on the different ratings of DERs, the DER's supply curve of the 5 kVA and 10 kVA ratings DERs are shown in Figure 5.17(a), and the aggregate curve is presented in Figure 5.17(b). When the DERs expect to support the voltage at the target location by 10 V, the results of reactive power dispatch of the DERs based on the TE approach when not considering their locations are presented in Figure 5.18.

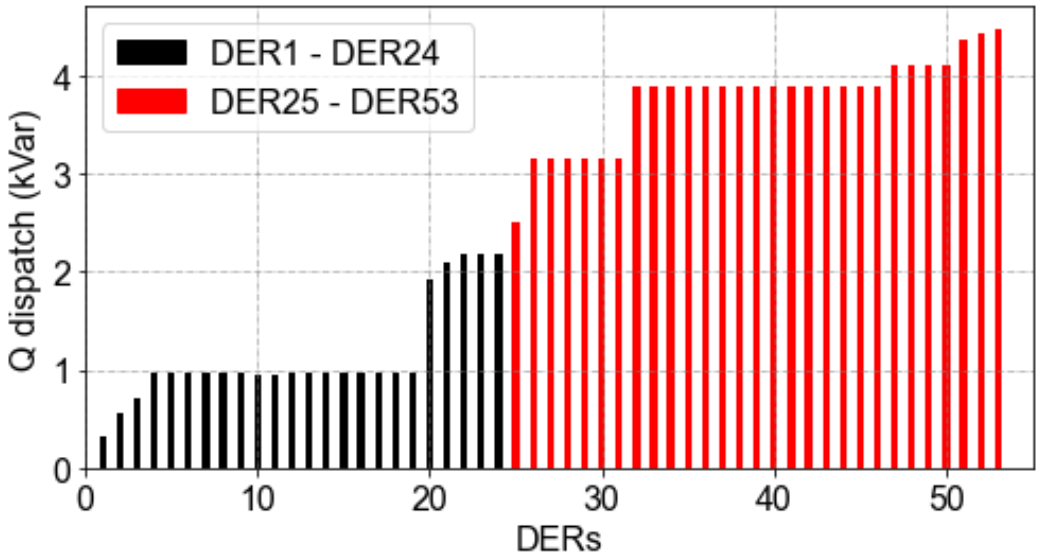

Figure 5.16: Reactive power dispatch of DERs with reactive power capacities at 8 kvar (black bar) and 4 kvar (red bar) based on the optimization approach by minimizing voltage deviation at the target location.

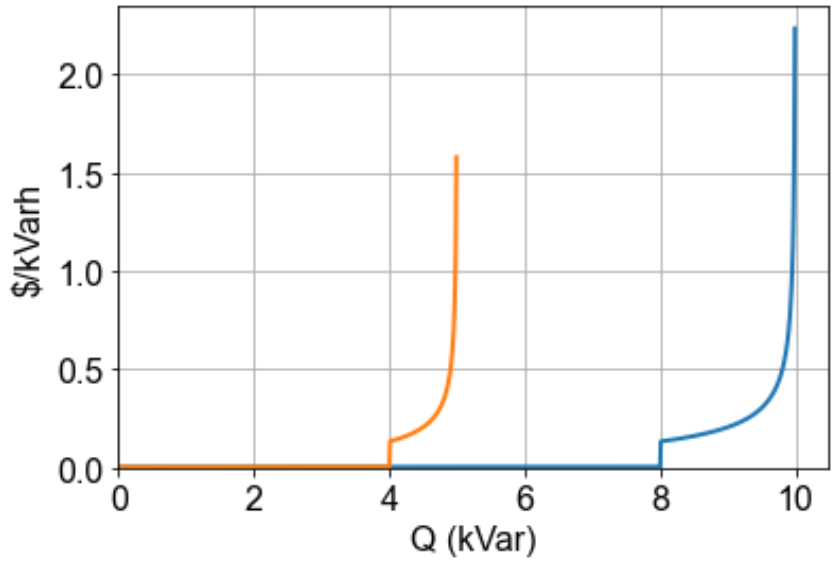

(a)

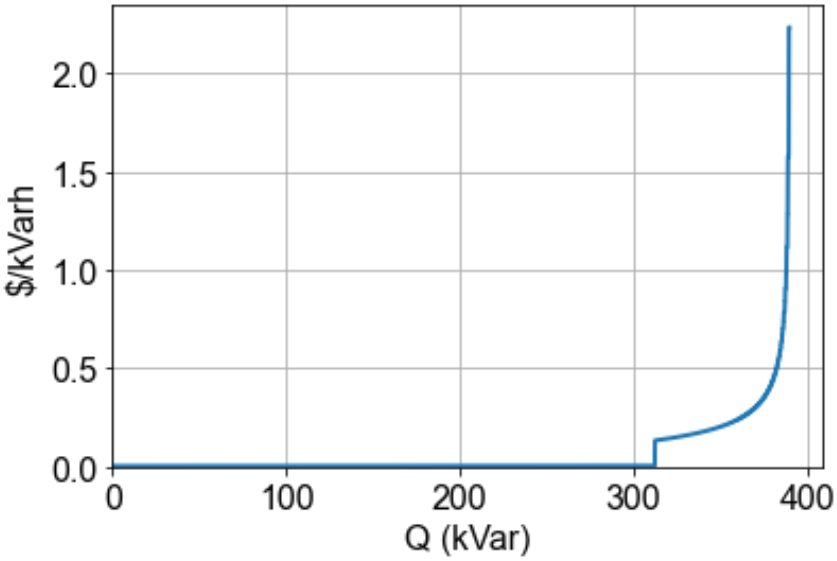

(b)

Figure 5.17: DER's supply curves without considering DER's location. (a) DERs at 5 kVA (orange curve) and 10 kVA rating (blue curve) and (b) Aggregate curve.

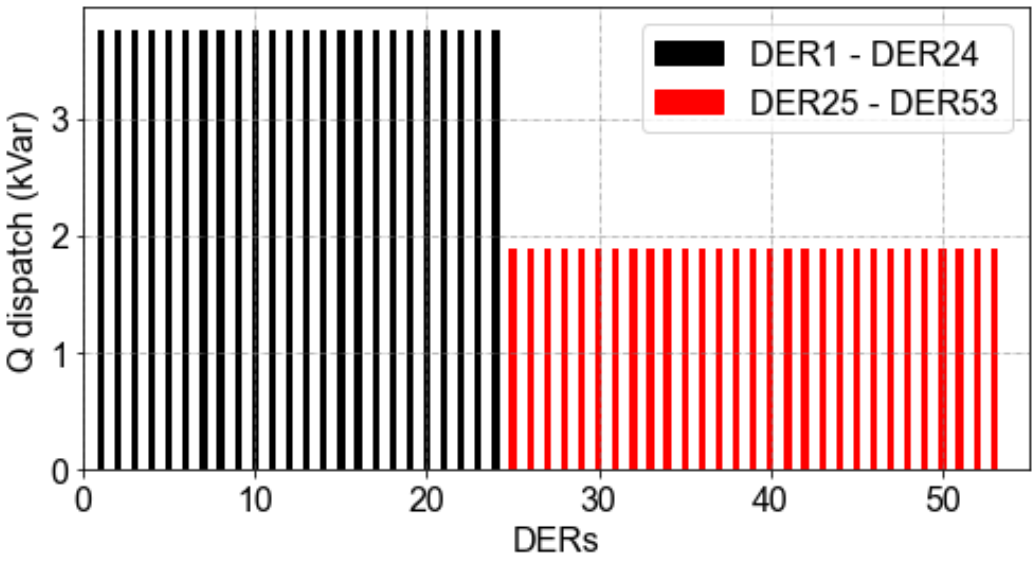

Figure 5.18: Reactive power dispatch of DERs with reactive power capacities at 8 kvar (black bar) and 4 kvar (red bar) based on the transactive energy approach when not considering the location of the DERs.

Based on the total amount of reactive power at 144 kvar, the reactive power dispatches from DERs are at 3.76 kvar and 1.88 kvar according to the different ratings of the DERs at 10 kVA and 5 kVA, respectively. The farther away DERs with higher reactive power capacities at lower cost provide more reactive power support than the closer DERs with higher cost due to the lower capacities. The voltage profiles based on reactive power dispatch of the three methods is presented in Figure 5.19.

The proposed method and the optimization method based on location-based reactive power dispatch successfully achieve the desired change in voltage at the target location. However, the non-location-based reactive power dispatch only increases the voltage at the target location by 6.9 V, despite providing the same amount of reactive power support based on the proposed method. Because the non-location method determines reactive power dispatch solely based on the cost of DERs. Hence, the lower cost DERs with lower impact on voltage change at the target location provide more reactive power in this case.

For the optimization method, it improves the voltage at the target location with less reactive power provided. However, since the cost of providing reactive power is not considered in the objective function, some closer DERs, which have a higher impact on voltage change at the target location, are required to curtail their active power to provide more reactive power support. This leads to an increase in the cost of providing reactive power support from these DERs.

Power losses from the power lines in the system after reactive power dispatches of location-based dispatches and non-location-based dispatch are investigated. The power losses including active and reactive power losses of the system based on test cases are shown in Table 5.4.

In the test feeder without the regulator, the voltage profile of the system has already been lower than the acceptable range at 0.95 pu. Table 5.4 shows that after the reactive power dispatch of all methods, both active and reactive power losses in the system can be reduced. The system losses decreased by 3.2% for active power loss and 4.5% for reactive power loss from the base case for both the proposed method and the optimization method. On the other hand, the reduction in losses achieved by the non-location dispatch method is less than the other two methods.

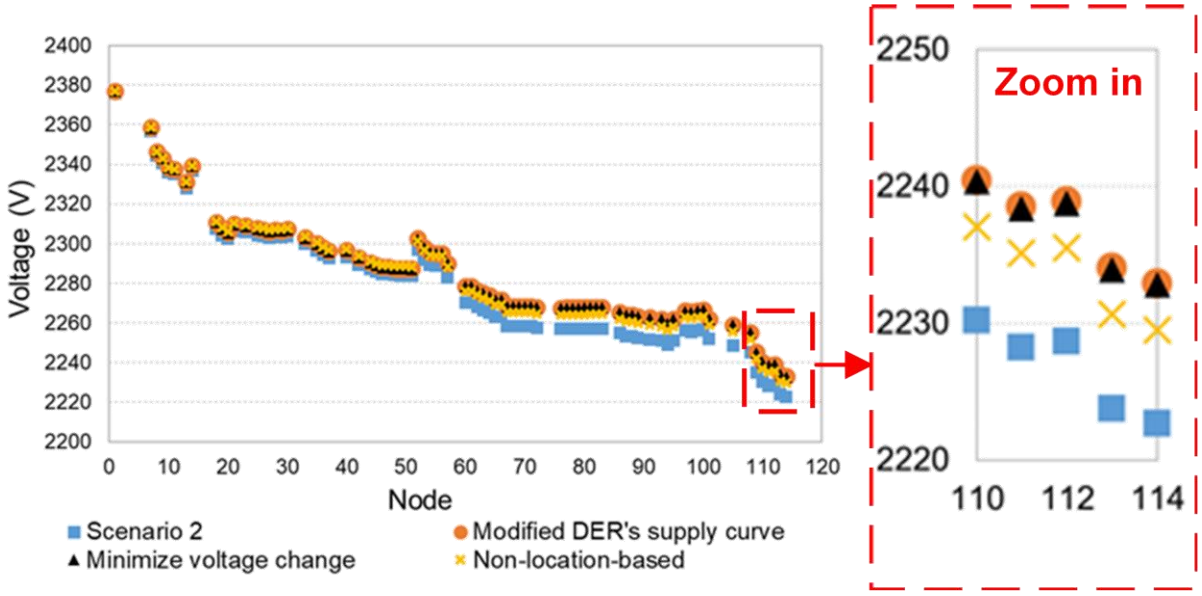

Figure 5.19: Voltage profile before (■) and after reactive power dispatch of the DERs based on the modified DERs' supply curves approach (●), optimization approach by minimizing the voltage deviation at the target location (▲), and non-location-based reactive power dispatch (×).

Table 5.4: Power Losses in the IEEE-123 Node Test Feeder based on Reactive Power Dispatch Methods.

Method	Active power loss (kW)	Reactive power loss (kvar)
Before reactive power dispatch from the DERs	27.745	61.238
Proposed	26.850 (3.23 % ↓)	58.469 (4.52 % ↓)
Optimization by minimizing voltage deviation	26.884 (3.10 % ↓)	58.569 (4.36% ↓)
Non-location reactive power dispatch	26.952 (2.86 % ↓)	58.844 (3.91% ↓)

5.5 Conclusions

Based on the limitation of location and cost of providing reactive power support, the allocation of reactive power support based on the TE approach is studied. By integrating voltage sensitivity into the DER's supply curve, the reactive power dispatch based on the TE approach can be done more efficiently. The simulation results of the test feeder show that the modified DER's supply curves can be used to determine the cleared price of the market, and once the DERs dispatch their reactive power based on the cleared price, the voltage at the target location can be changed accordingly.

The effectiveness of the proposed method is investigated by using two different test feeders. The results of the reactive power dispatch based on the proposed method can be effective on both feeders. Some test scenarios are provided to illustrate the characteristics of the method. The results show that the DERs with more impact on the voltage with the lower cost of providing reactive power will be considered first based on the approach. The closer DERs might provide less reactive power support if they have lower reactive power capacities (higher cost to provide voltage support) than the further away DERs. Voltage profiles of the IEEE 123-node test feeder are compared between different reactive power dispatch approaches. The voltage at the target location can be successfully changed by the implementation of the proposed method and the optimization method. However, the non-location-based reactive power dispatch could not adequately change the voltage at the target location and will require more reactive power than the location-based dispatches. The power loss analysis for the system is performed, and the result shows that the proposed method does not represent a significant change in the system's losses.

Chapter 6

Linear Quadratic Regulator-based Controller for Control Mode Switching Under Fault Operation of PVSS

This chapter presents a regulator-based controller to address a control mode switching of PVSS when SC is fully charged during fault. Due to the challenge presented by the standard IEEE1547.9-2022 revision [50] in LVRT operations of grid-connected energy storage systems (ES DERs), it is recommended that the ES DERs should be able to provide LVRT operations based on Category III. Regarding the updated requirements, the PVSS will have to reserve more SC's capacity to ensure that the SC can provide LVRT services for a longer time compared to Category II as presented in Chapter 4. Moreover, the standard requires PVSS to support more consecutive faults where the time between each fault event is shorter at 5 s compared to Category II at 10 s as shown in Figure 6.1 [50]. Thus, these become challenges to reserve SC's capacity to support the LVRT operations according to Category III requirements. SC usually has low energy capacity; it will have to charge and discharge more often with a bigger reserved band based on the proposed control in Chapter 4 to ensure the SC's capacity during the LVRT events according to Category III requirements. Consequently, this might impact the SC during normal operations.

As demonstrated in Chapter 4, DC-link overvoltage happens when the SC reaches its voltage limits during LVRT operation. At that time, the DC-link voltage is switched to be controlled by the inverter, and the PV system might need to curtail its power generation. Under this condition, the PVSS stability is compromised, which might lead to the disconnection of PVSS from the grid under severe fault conditions. Thus, this work proposes a linear quadratic regulator (LQR)-based controller to ensure a smooth control mode transition when the SC is completely charged during fault operations. The proposed LQR-based controller is validated on the HTB to demonstrate its effectiveness in reducing DC-link overvoltage during the control transitions.

Portions of this chapter have been previously published in the article "Linear Quadratic Regulator-based Controller for Control Mode Switching Under Fault Operation of Grid-Connected PV with Supercapacitor System" that was presented at the IEEE Energy Conversion Congress and Exposition (ECCE) 2024 meeting.

Table 17 —Voltage ride-through requirements for consecutive temporary voltage disturbances caused by unsuccessful reclosing for DER of abnormal operating performance Category I, Category II, and Category III

Col. 1	Col. 2	Col. 3	Col. 4
Category	Maximum number of ride-through disturbance sets	Minimum time between successive disturbance sets (s)	Time window for new count of disturbance sets (min)
I	2	20.0	60
II	2	10.0	60
III	3	5.0	20

Figure 6.1: Voltage ride-through requirements for consecutive faults based on different categories [50].

6.1 Control Mode Switching of PVSS when SC is Unavailable

SC controls the DC-link voltage of the PVSS by charging or discharging itself to maintain power balance between AC side and DC side of the PVSS. During LVRT operations when PVSS is required to stay connected to the grid based on IEEE 1547 requirements, the SC typically absorbs PV power that cannot be injected into the grid during low voltage conditions, and the PV system can continue its operation in MPP mode. Also, the grid-connected inverter provides reactive power to support grid voltage during LVRT operations according to the requirements. The SC acts as an energy buffer to store the PV power and maintain the DC-link voltage and power balance within the PVSS. In the case when the SC reaches its upper voltage limit from absorbing PV power (fully charged), its operation will be stopped to prevent itself from over-charging [20], [43]. The inverter then needs to take control of the DC-link voltage to stabilize the PVSS [20], [43] and the PV system curtails its power generation to maintain power balance within the PVSS.

The PV power curtailment control during non-MPP operation is adopted from [42] in which the PV's DC-DC converter is controlled by the duty cycle calculated based on the PV power reference during the curtailment. The duty cycle during the non-MPP operation ($d_{pv,non-MPP}$) can be calculated as follows [42]:

$$d_{pv,non-MPP} = 1 - \frac{P_{pv,non-MPP}}{I_{sc} v_{dc}} \tag{6.1}$$

where $P_{pv,non-MPP}$ is the target PV power during non-MPP operation, I_{sc} is the PV's short circuit current, and v_{dc} is the DC-link voltage.

The PV system will operate on the left side of the PV characteristic curve to reduce instability concerns during rapid changes in the PV operations [42]. The PV control also uses a rate limiter to prevent a sudden change in the calculated duty cycle of the PV system. It helps reduce the oscillations of the PV power that can lead to unstable operations when the non-MPP control is activated.

6.2 Linear Quadratic Regulator (LQR) for Control Switching

A linear quadratic regulator (LQR)-based controller can minimize the discontinuity of the plant's input signal during control mode switching between different operations. The discontinuity

of the input signal can cause large transients in the system's output waveforms during the control transition, which can impact the system's stability, especially during vulnerable operations such as faults.

Two controllers are involved in the control switching operation: the active controller and the nonactive controller. The active controller represents the current controller that gives the input signal to the plant. Meanwhile, the nonactive controller is the offline controller that will later be online after the control mode switching.

The LQR-based controller utilizes information from both active and nonactive controllers, including the nonactive controller's states, the plant's input signal from the active controller, and the nonactive controller's error input signal. The following information is used to control the nonactive controller prepared for the mode transition, thus reducing the step change or discontinuity of the input signal to the plant.

According to Figure 6.2 in the inverter control diagram of the PVSS, two switching actions will happen at the instant of the control mode transition [113]; the plant input will switch from the active controller (active power control) to the nonactive controller (DC-link voltage control), and the input to the nonactive controller will switch from the LQR compensator output to the error between reference and measurement signals of the DC-link voltage.

6.2.1 Requirement of LQR Compensator

The LQR compensator can be designed according to the overshoot and settling time (T_s) criteria of the 2nd order system [113], [114], which are presented as follows [115]:

$$Overshoot\ (\%) = 100 \times e^{\frac{-\xi\pi}{\sqrt{1-\xi^2}}}$$
$$T_s = \frac{4}{\xi W_n} \tag{6.2}$$

where ξ is a damping ratio and W_n is a natural frequency regarding the damping ratio.

Based on the system requirement equations, overshoot will be lower with a higher value of ξ. For an underdamped system, the commonly used values of ξ in the design is at 0.707 [113], [114]. Thus, the overshoot specification should be more than 4.33% according to the requirement of ξ for the underdamped system. The nonactive controller's eigenvalues are calculated according

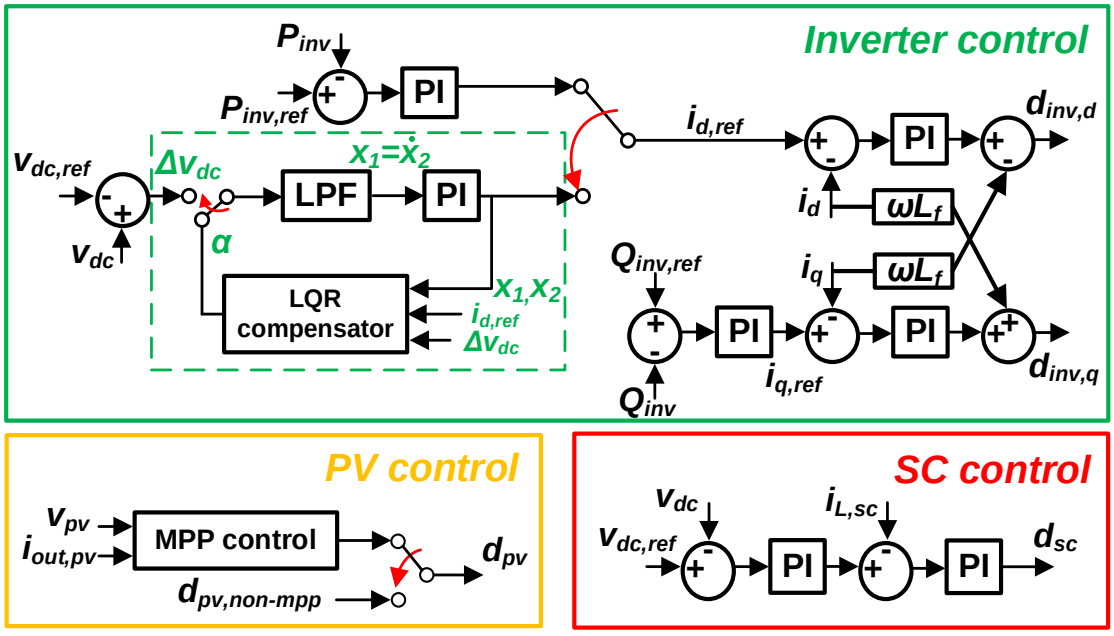

Figure 6.2: Control mode switching of PVSS when SC reaches its voltage limit during LVRT operation.

to the design requirements presented above. They will be used in the optimization problem that will be discussed in Section 6.2.4.

6.2.2 LQR-Based DC-LINK Voltage Control of PVSS

The LQR-based control requires the state space model of the nonactive controller to compute its feedback matrix. The state space model of the DC-link voltage control in Figure 6.2 can be derived and presented as follows:

$$\begin{aligned}\begin{bmatrix}\dot{x_1}\\ \dot{x_2}\end{bmatrix} &= \overbrace{\begin{bmatrix}-w_{c,v_{dc}} & 0\\ 1 & 0\end{bmatrix}}^{A}\begin{bmatrix}x_1\\ x_2\end{bmatrix} + \overbrace{\begin{bmatrix}w_{c,v_{dc}}\\ 0\end{bmatrix}}^{B}[\alpha]\\ [i_{d,ref}] &= \overbrace{[-k_{p,v_{dc}} \quad -k_{i,v_{dc}}]}^{C}\begin{bmatrix}x_1\\ x_2\end{bmatrix} + \overbrace{[0]}^{D}[\alpha]\end{aligned} \tag{6.3}$$

where $w_{c,v_{dc}}$ is the cut-off frequency of the low-pass filter of the DC-link voltage PI controller, $k_{p,v_{dc}}$ and $k_{i,v_{dc}}$ are PI control parameters of the DC-link voltage loop, α is the output of the LQR-based controller. $i_{d,ref}$ is the reference of the *d*-axis current loop, x_1 is the state of the input filter of the PI controller and x_2 is the state of the integrator of the DC-link voltage PI controller.

6.2.3 Design of LQR-based Controller

Algorithm 2 is used to find the LQR parameters regarding the desired requirements, which are revised from [113]. The algorithm takes the Overshoot and T_s from (6.2) as input requirements of the LQR controller. The state-space model of the DC-link voltage controller from (6.3) in the form of A, B, C, D matrices are used in (6.4) to compute the parameters $(\tilde{A}, \tilde{B}, \tilde{C})$ as follows:

$$\begin{aligned}\tilde{A} &= A + B\Delta D'QC\\ \tilde{B} &= B\Delta B'\\ \tilde{C} &= C'Q(I + D\Delta D'Q)C\end{aligned} \tag{6.4}$$

where Q and R are weighting matrices of the LQR controller and $\Delta = -(D'QD + R)^{-1}$.

According to (6.4), the Algebraic Riccati Equation (ARE) can be formulated as follows:

$$P\tilde{A} + \tilde{A}'P + P\tilde{B}P + \tilde{C} = 0 \tag{6.5}$$

where P is the output matrix from solving the ARE by using the care function in MATLAB [113]. The equation is solved by assuming that $(\tilde{A}, \tilde{B})$ are controllable and $(\tilde{A}, \sqrt{\tilde{C}})$ are observable.

Algorithm 2: Design of LQR compensator [113]

Input: $Overshoot\ (\%)$: percentage of overshoot from (6.2)

T_s: settling time from (6.2)

$k_{p,v_{dc}}, k_{i,v_{dc}}$: DC-link voltage control loop PI control parameters

$w_{c,v_{dc}}$: Low pass filter cutoff frequency of the DC-link voltage controller

Output: F_b: LQR state feedback matrix

Procedure:

Compute the state-space model of the DC-link voltage controller from (6.3)

Compute pole locations based on the input requirements in terms of T_s and $Overshoot$. *// these pole locations will be used in the optimization problem*

Compute the optimization problem from (6.8)

while ε < optimization criteria

Solve the optimization problem by using the solver in MATLAB

Compute input parameters of ARE equation in (6.4)

Compute and solve the Algebraic Riccati Equation (ARE) in (6.5)

Compute LQR feedback matrix (F_b) in (6.7)

end

After the ARE is computed, the output of the LQR-based controller (α) can be calculated as follows:

$$\alpha = F_b \begin{bmatrix} x_1 \\ x_2 \\ u_1 \\ e_2 \end{bmatrix} \tag{6.6}$$

where $u_1$is output of the active power's PI controller and e_2 is the DC-link voltage error between its reference and measurement. F_b is the LQR feedback matrix, which can be calculated by (6.7) as:

$$F_b = \Delta \begin{bmatrix} (B'P + D'QC)' \\ \left(-D'Q + B'A_g^{-1}(C'Q + C'QD\Delta D' + PB\Delta D'Q)\right)' \\ \left(-R + B'A_g^{-1}(C'QD\Delta R + PB\Delta R)\right)' \end{bmatrix}' \tag{6.7}$$

According to Figure 6.2, α is an input to the DC-link voltage PI controller instead of the error of the DC-link voltage and its reference when the active power controller is online. During the control mode switching, when the SC becomes unavailable, the *d*-axis current control will switch its input from the active power controller to the DC-link voltage control to maintain the DC-link voltage of the PV system instead of the SC. At the instant of the control mode switching, the input of the PI controller of the DC-link voltage loop is switched from α to the error of the DC-link voltage when compared to its reference value.

6.2.4 Selection of LQR Control Parameter by Optimization

Optimization is adopted to find the LQR-based controller's parameter to achieve the desired specifications mentioned in Section 6.2.1. Optimization aims to find the parameters of the nonactive controller whose performance can satisfy the overshoot and settling time requirements. Optimization can be achieved by minimizing the distances between the desired pole locations of the nonactive controller's eigenvalues based on the overshoot and setline time requirements and the current pole locations of the nonactive controller.

The optimization function can be formulated as [114]:

$$Min\ F = \ \sum_i \left(\left|\lambda_i^{des}\right| - \left|\lambda_i^{off}\right|\right)^2 (1 + Pen) \tag{6.8}$$

where λ_i^{des} are the destination locations of the dominant poles i, and λ_i^{off} are the current pole locations of the nonactive controller. The penalty function (Pen) is added to incorporate the controllability and observability conditions according to the assumption of solving the ARE equation in (6.5) [114].

6.3 Experiment of LQR Control of PVSS in HTB

6.3.1 PVSS Dynamics during the LVRT Event

The low voltage condition for the LVRT scenario is emulated on the HTB platform by applying a step change (add large load) to the load emulator. The AC terminal voltage decreases according to the amount of the load applied during the LVRT scenarios. According to IEEE 1547 requirements, PVSS is required to provide reactive power during LVRT events according to grid voltage level and the maximum injected reactive power can be up to the PVSS's power rating [50]. Figure 6.3 demonstrates the PVSS dynamics during LVRT operation with the case when the SC is available (red) and the Base case when the SC reaches its voltage limit during the operation (blue). When the LVRT event happens at 0.3 s with the voltage decreasing to 0.58 pu, PVSS starts providing its reactive power at 55 kvar (its power rating) according to the low voltage condition and the grid voltage can be improved to 0.65 pu. The PVSS needs to reduce the active power injected into the grid to make room for the reactive power support at its full power rating. The SC simultaneously absorbs the PV power at 50 kW to reduce the unbalanced power on the DC-link, and the PV system continues its MPP operation. When the SC is available to support the PV system during LVRT operation, the control mode does not have to be switched, and PV power does not have to be curtailed. Thus, no transient overvoltage happens at the DC-link. For the case when the SC reaches its voltage limit during the LVRT event at ~1 s, the PV system must curtail its output power to zero, and the control mode is switched to the inverter controller to control the DC-link voltage instead of the SC. The SC power is reduced to zero to prevent it from overcharging. During the control mode transition, the DC-link voltage oscillates to 1024 V before returning to its nominal value at 900 V as shown in Figure 6.3.

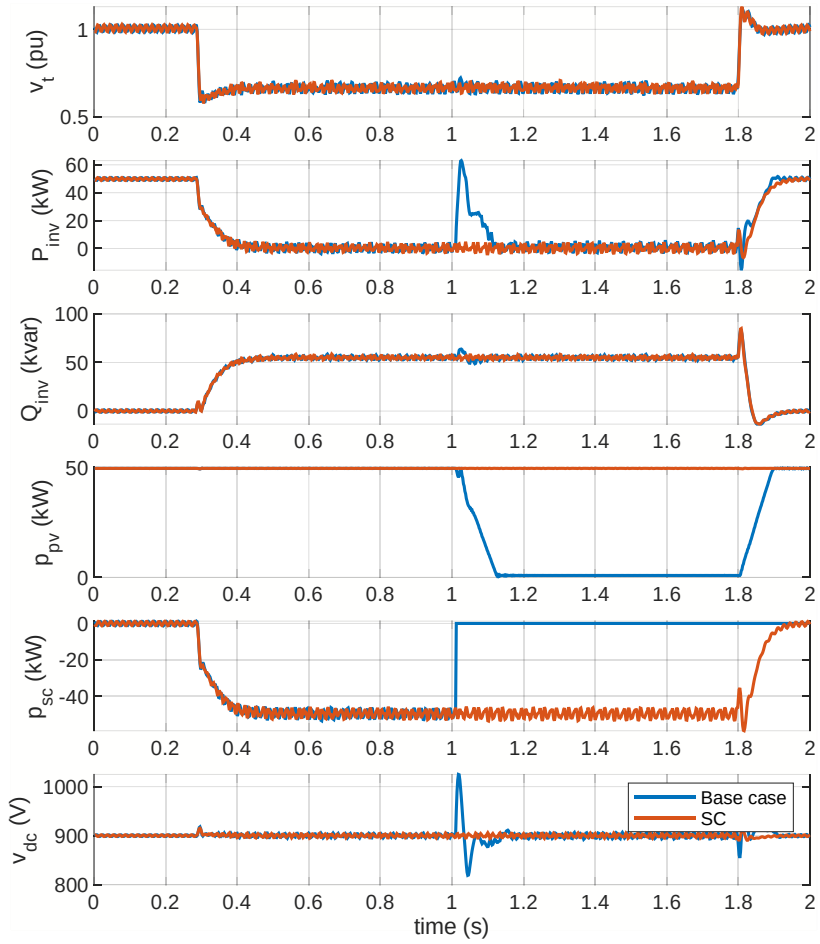

Figure 6.3: PVSS dynamic during LVRT event when SC is unavailable (Base case in blue) and when SC is available (SC in red).

6.3.2 Performance Evaluation of LQR-Based DC-Link Voltage Control

This section evaluates the performance of the LQR-based DC-link voltage controller. Its effectiveness in suppressing DC-link overvoltage is demonstrated by comparing it to the traditional feed-forward DC-link voltage compensator.

LQR-based DC-link voltage control is implemented in the emulator based on the settling time requirements at 100 ms and overvoltage limits of 5%. The feed-forward DC-link voltage control presented in [116] is used as benchmark control, considering PV dynamics directly in the DC-link voltage control loop. The compensator's output is calculated by dividing the PV power by the DC-link voltage. The output of the DC-link voltage control with the compensation is the summation of the DC-link voltage controller's output and the feed-forward term.

The performance of the proposed LQR-based control is demonstrated based on PV operations and different levels of grid disturbance and PV operations below.

6.3.2.1. PV operations

The LQR-based DC-link voltage compensator is evaluated under different PV generation outputs at 12.5 kW, 25 kW, and 50 kW (rating), as demonstrated in Figure 6.4. During high PV power output, the transient DC-link overvoltage increases due to more unbalanced power presented on the DC-link during PV curtailment and control mode switching under LVRT operation.

The LVRT operation is emulated, where the AC voltage drops to 0.58 pu (without the reactive power support from the PVSS) for every PV operation. Based on the voltage level, the PVSS provides reactive power support to the grid at 55 kvar (its full rating), and the grid voltage is increased to 0.65 pu during the operation. The control mode switching happens at 0.2 s, where the PV needs to curtail its power generation to zero when the SC is unavailable during the fault.

According to Figure 6.4, the experimental results demonstrate the DC-link voltage dynamics during the LVRT event according to PV operations at (a) 12.5 kW, (b) 25 kW, and (c) 50 kW. For each PV operation, the following test cases are conducted, including no compensator

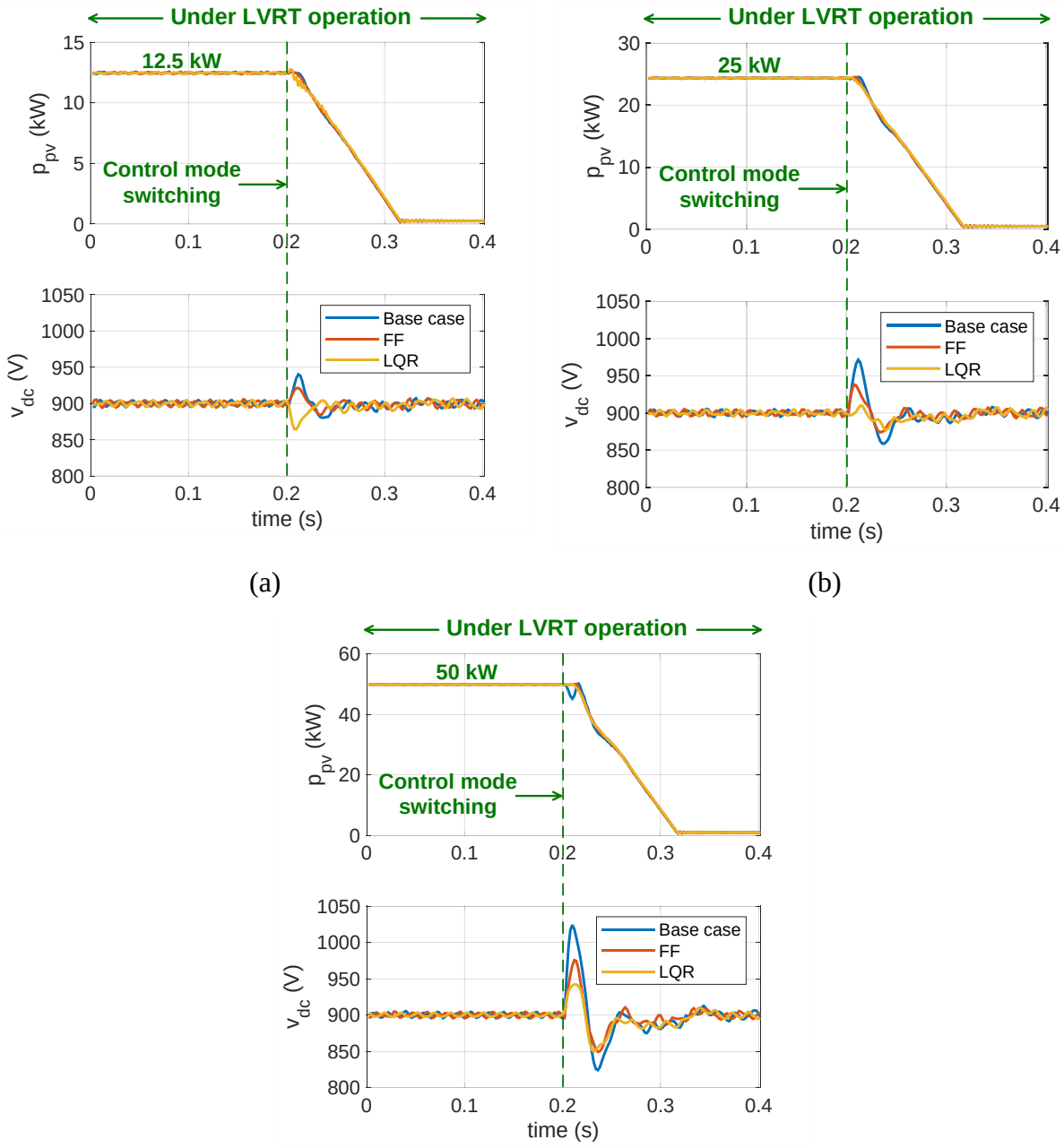

Figure 6.4: Comparison of the compensators during LVRT operation at PV operations of (a) 12.5 kW, (b) 25 kW, and (c) 50 kW.

(Base case), feed-forward (FF), and LQR-based DC-link voltage compensator (LQR). The transient DC-link overvoltage of the Base case increases when the PV operates closer to its maximum power rating at 50 kW. According to the results, the DC-link overvoltage can be suppressed using FF and LQR compensators in every PV operation.

When the PV system operates at 12.5 kW, the compensator performances are insignificant compared to the Base case because of less DC-link overvoltage during the LVRT event as shown in Figure 6.4(a). The FF and LQR compensators can keep the DC-link voltage within 5% of its nominal value during the control mode switching under LVRT operation. During the PV operation of 25 kW, the DC-link overvoltage of the Base case is at 971.58 V, and by implementing FF and LQR compensators, the DC-link overvoltage is at 938.26 V and 910 V, respectively. When the PV system operates at 50 kW, the DC-link voltage of the Base case is at 1024 V. The DC-link overvoltage of FF and LQR is 975.52 V and 942.07 V, respectively. For this case, only the LQR compensator can keep the DC-link overvoltage within 5%, reducing the overvoltage by 44% compared to the FF control. Details of the DC-link voltage value of each PV scenario can be found in Table 6.1.

Regarding performance, the LQR-based DC-link voltage controller outperforms the FF compensator in reducing DC-link overvoltage when the SC reaches its limit during LVRT operation under medium and high PV operations. For the scenario at low power PV operation (less than 12.5 kW), the LQR controller overcompensates the DC-link overvoltage, yet the voltage remains within 5% of its nominal value. The performance of the LQR compensator under this scenario can be improved by having another set of LQR parameters for the low-power PV operation. Another solution is disabling the compensators, which are unnecessary during low-power PV operations when the PVSS experiences less DC-link overvoltage.

6.3.2.2. Voltage sag levels

This section evaluates the proposed LQR compensator under different voltage sag levels within the mandatory operations of IEEE 1547 Category III requirements [50].

According to Figure 6.5, voltage sags at different levels are emulated on the HTB, including (a) 0.9 pu, (b) 0.8 pu, (c) 0.65 pu, and (d) 0.5 pu. The PV system operates at its power rating of 50 kW for every voltage sag scenario. The PVSS has higher transient DC-link overvoltage

Table 6.1: DC-link Overvoltage during the Control Mode Transition at Different PV Operations.

Test scenarios	**DC-link overvoltage (V) and its deviation from the nominal value (%) at PV operations**		
	12.5 kW	**25 kW**	**50 kW**
Base case	940.21 V (4.47 %)	971.58 V (7.95 %)	1024 V (13.77 %)
FF compensator	921.44 V (2.38 %)	938.26 V (4.25 %)	975.52 V (8.39 %)
LQR compensator	-	910 V (1.11 %)	942.07 V (4.67 %)

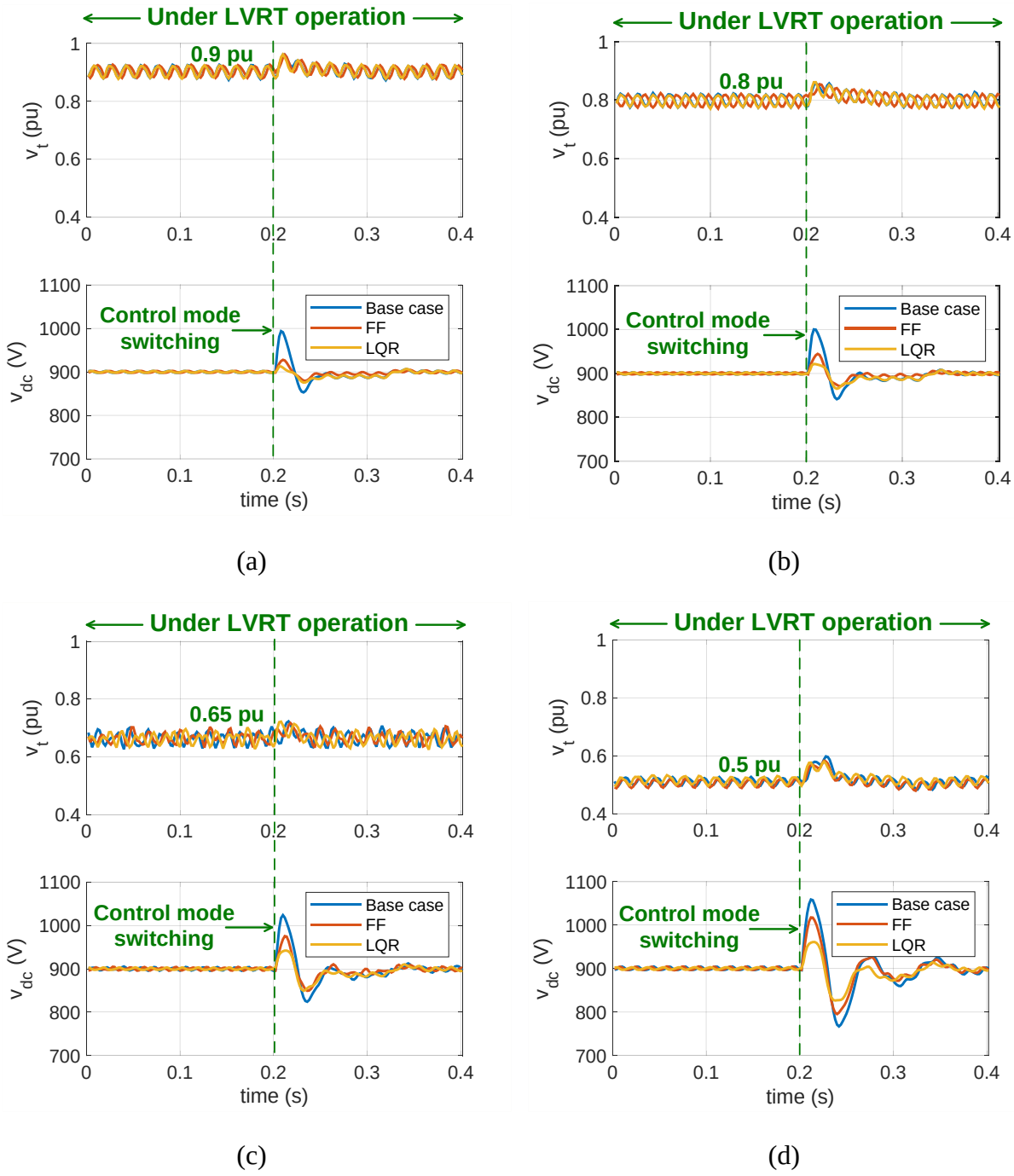

Figure 6.5: Comparison of the compensators at voltage sag levels of (a) 0.9 pu, (b) 0.8 pu, (c) 0.65 pu, and (d) 0.5 pu during LVRT operation.

when the AC terminal voltage drops to a lower value during the operation. For instance, during a 0.5 pu voltage sag, the DC-link overvoltage of the Base case reaches 1058.8 V, which is a 17.64% deviation from its nominal DC-link voltage. By implementing the FF and LQR compensators, the DC-link overvoltage can effectively be reduced during control mode switching under the LVRT event for every level of voltage sag when compared to the Base case without compensators.

Overall, the LQR compensator performs better in reducing the transient DC-link overvoltage; the DC-link voltage is reduced by 44% to 53% compared to using the FF compensator for every voltage sag test scenario, as detailed in Table 6.2. The LQR compensator can keep the transient DC-link overvoltage within 5% based on the design requirement until the voltage sags at 0.65 pu. The PVSS with the LQR compensator experiences higher DC-link overvoltage later when the AC terminal voltage drops below 0.65 pu. Meanwhile, the FF compensator has a DC-link overvoltage of ~5%, starting from voltage sag at 0.8 pu. The results demonstrate the effectiveness of the proposed LQR compensator in reducing the transient DC-link overvoltage when the control mode transitions and PV curtailment occurs during LVRT operation.

6.4 Conclusion

This chapter presents the design of the LQR-based compensator to help during the control mode switching when the SC reaches its capacity during LVRT operations. The proposed LQR-based controller can effectively reduce the transient DC-link overvoltage during the transition from active power control to DC-link voltage control when the SC reaches its capacity during severe fault ride-through operations. Experiments are conducted on the HTB platform to validate the performance of the LQR compensator. It can reduce the DC-link overvoltage, allowing the PV system to maintain its stability and operate under fault conditions, complying with grid requirements. The performance of the LQR compensator is evaluated by comparing it to the traditional feed-forward DC-link voltage compensator. The comparison results show that the LQR-based controller can effectively suppress the DC-link overvoltage compared to the feed-forward control. The effectiveness of the proposed LQR-based control is confirmed under different PV operations and voltage sag levels based on the mandatory operations according to IEEE-1547 requirements. Thus, the proposed control can increase the PV system stability when the SC reaches its limits during LVRT operation.

Table 6.2: DC-link Overvoltage during the Control Mode Transition at Different Levels of Voltage Sag.

Test scenarios	**DC-link overvoltage (V) and its deviation from the nominal value (%) at PV operations**			
	0.9 pu	**0.8 pu**	**0.65 pu**	**0.5 pu**
Base case	993.82 V (10.42 %)	1000.3 V (11.15 %)	1024 V (13.77 %)	1058.8 V (17.64 %)
FF compensator	927.86 V (3.1 %)	944.6 V (4.96 %)	975.52 V (8.39 %)	1017.6 V (13.06 %)
LQR compensator	912.95 V (1.44 %)	921.59 V (2.4 %)	942.07 V (4.67 %)	960.99 V (6.78 %)

Chapter 7

Fast Frequency Support and Fast Frequency Recovery provided by PVSS

The study of fast frequency support provided by the PVSS based on IEEE1547.9-2022 revision [50] is presented in Chapter 3. The results demonstrate that the support provided by the PVSS improves both grid frequency and ROCOF during grid frequency disturbances. This chapter will explore the inertia support and fast frequency recovery provided by PVSS, which extends the works presented in Chapter 3. The inertia responses of the PVSS based on different inertia coefficients are investigated, and the results show that power oscillations occur at high inertia coefficient settings without much improvement of ROCOF during the event. This challenge of power oscillation prevents the PVSS from efficiently providing support, as the SC power will be consumed during the oscillations without much improvement in the event's ROCOF. Thus, the proposed work aims to provide a control method to maximize the inertia support of PVSS while reducing power oscillations during the event. The fast frequency recovery service provided by the PVSS will also be studied in this Chapter. The PVSS will provide support during the frequency recovery period, assisting the grid frequency in return to its nominal value within a short time.

7.1 Impact of High Inertia Coefficient

Power systems with high integrations of DERs have experienced challenges in frequency regulation and reduction of ROCOF in the systems. Therefore, the standard IEEE1547.9-2022 revision [50] requires DERs with energy storage systems to provide fast frequency support, including frequency support and inertia emulation during frequency disturbance events.

PVSS can contribute more active power to reduce ROCOF during frequency disturbances by setting a high inertia coefficient (k_{iner}). However, the challenge of providing inertia emulation with the high k_{iner} is active power oscillations issue [117] and long frequency settling time during the frequency recovery period [118]. The power oscillation issue limits the utilization of the PVSS during the inertia emulation services due to less improvement in ROCOF while providing more

power to support the system. Thus, there is a need for a control method to reduce the power oscillations issue to enable support from PVSS efficiently.

PVSS is required to provide fast frequency support until the grid frequency is back within its nominal condition, and it should not cause a delay in the system's frequency recovery. However, if the traditional control is applied during the fast frequency support, the frequency recovery will be delayed due to a change of sign of the ROCOF when the grid frequency returns to its nominal value. For example, PVSS absorbs power from the system during the recovery period of the under-frequency, as presented in Section 3.3.2.4 due to a minus sign of ROCOF during the recovery period. With a high k_{iner}, the amount of absorbed active power will also be higher, causing more delay in returning the frequency to its nominal value.

To prevent the delay during the frequency recovery period, this study implements the control method proposed in the literature [117], [118], as so-called bang-bang control. The control considers a change of sign of inertia emulation during frequency recovery to continue injecting active power to support the frequency during the recovery period in the case of under-frequency events. Meanwhile, the PVSS will absorb active power during the frequency recovery period for the over-frequency events based on the bang-bang control. Thus, by implementing bang-bang control, the frequency recovery time can be reduced, leading to improved frequency recovery services.

7.2 Proposed Control for Fast Frequency Support including Fast Frequency Recovery

According to the challenges posed by setting a high k_{iner}, the study adopted a similar control concept to [118] by adjusting k_{iner} during the frequency event. The k_{iner} is set to be high to maximize active power support to lessen ROCOF at the beginning of the event. After the ROCOF approaches zero during the event, k_{iner} will be adjusted to a lower value to reduce power oscillations. In this way, the SC power will not be wasted during the support without any improvement in ROCOF.

During the frequency recovery, the bang-bang control is adopted to address the change in sign convention of ROCOF. This prevents the PVSS from causing a delay in the frequency

recovery period. The adjustment during the recovery period from [118] is proposed to achieve a faster frequency recovery service. Reference [118] proposes to adjust k_{iner} to a low value to reduce the settling time of the frequency during the recovery period. However, this study proposed to use a high k_{iner} to speed up the frequency recovery by utilizing both inertia and frequency deadbands to deactivate the inertia support during the recovery period. Figure 7.1 illustrates the concept of the benchmark control, as referred from [117], [118], and the proposed control.

7.3 Experimental Results

The proposed control is evaluated by conducting experiments on the HTB using the testbed presented in Chapter 3. Three converters are used to represent the test setup on the HTB, including a generator emulator, load emulator, and PVSS emulator. The under-frequency and over-frequency scenarios are emulated by changing the power generation or power load in the test system.

7.3.1 Experimental Results of Adjustment of Inertia Coefficient on HTB

The experiments are conducted to observe the PVSS dynamics under different static values of k_{iner} during an under-frequency event shown in Figure 7.2. The results show that high k_{iner} can slow down ROCOF during the frequency disturbance rather than the low k_{iner} because more active power is injected into the grid. However, there are power oscillations that limit the PVSS to efficiently provide support at the high k_{iner} values. The SC power of the high k_{iner} = 8 is dissipated during the power oscillations with limited improvement of ROCOF compared to the results of lower k_{iner} values. Therefore, the study proposes an adjustment of k_{iner} during grid frequency support when ROCOF approaches zero (ROCOF < 0.05 Hz/s) to reduce the power oscillations associated with high k_{iner} settings. Figure 7.3 demonstrates that by adjusting k_{iner} from 8 to be at a lower value (k_{iner} = 0 or 2) based on the proposed control, the power oscillations can be reduced. These test results confirm the effectiveness of the proposed control to minimize the power oscillation issue with high k_{iner} to maximize the inertia support from the PVSS during the frequency disturbances.

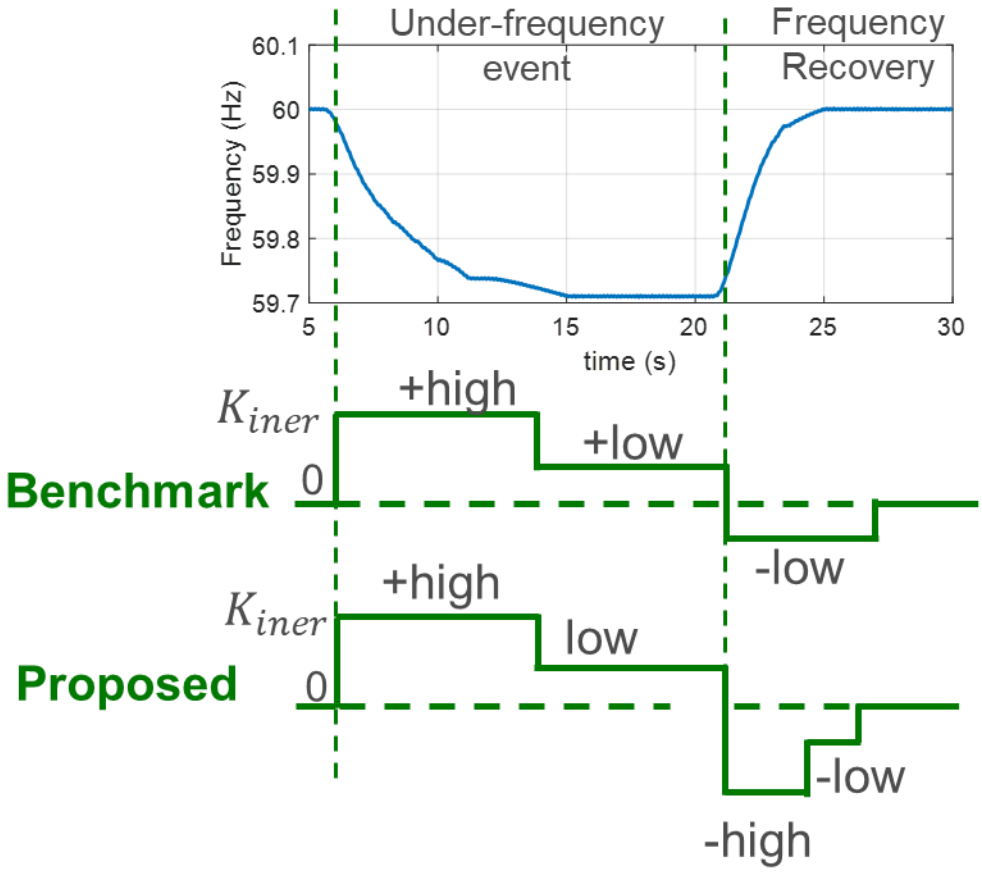

Figure 7.1: Concept of the benchmark control [117], [118] and the proposed modified inertia emulation control.

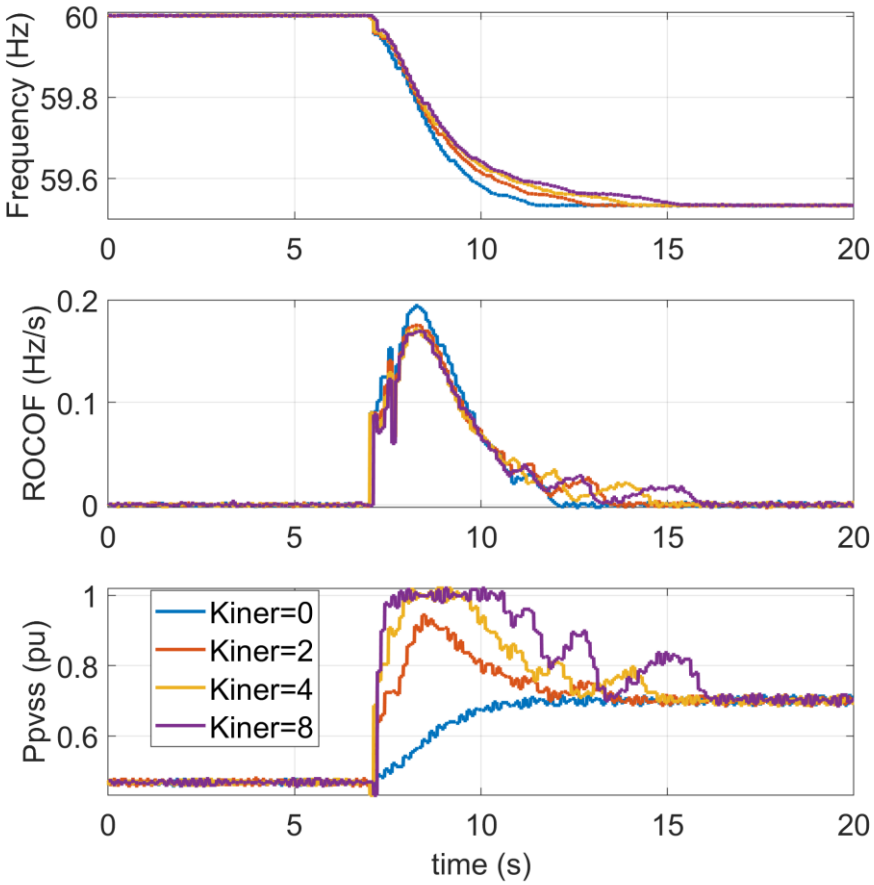

Figure 7.2: Frequency dynamics based on different static values of k_{iner} under the under-frequency event.

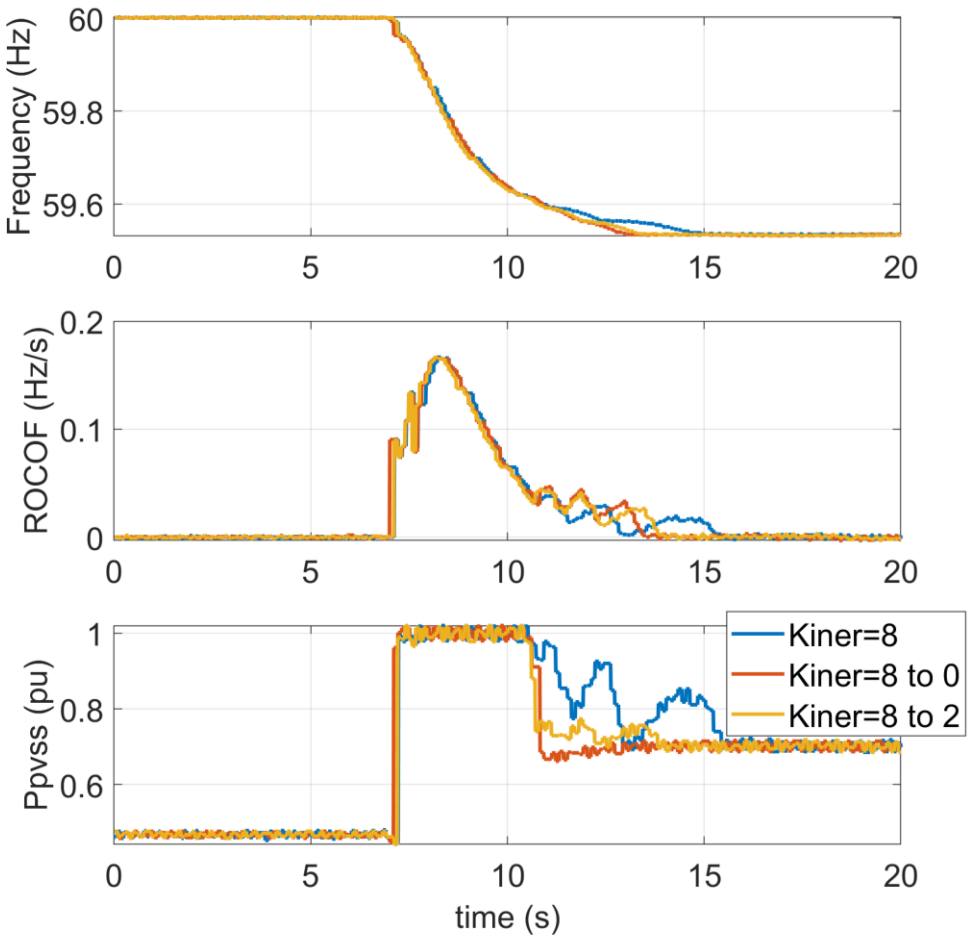

Figure 7.3: PVSS dynamics when adjusting k_{iner} during the under-frequency event.

The test is also conducted under an over-frequency event to confirm the effectiveness of the proposed control as shown in Figure 7.4. The results also show that the power oscillations can be reduced by adjusting k_{iner} from 8 to a lower value (k_{iner} at 0 or 2) during the event. In this way, the PVSS can provide maximum support at the beginning of the event with less power oscillations during the event when the ROCOF is getting close to 0 Hz/s.

7.3.1.1. Experiment Results under Different Severity of Frequency Events

The proposed control is validated under different severities of under-frequency and over-frequency events on the HTB. This is to confirm that the proposed adaptive inertia control can reduce power oscillations during the support under different severity of frequency events.

The event severity is determined by the level of unbalanced power between the generation and load in the test system, as indicated by L1 – L4 in Figure 7.5 and Figure 7.6. The unbalanced power of the test scenarios ranges from L1 (lowest) to L4 (highest). The higher unbalanced power will result in more severity of the event during the tests.

The test scenarios are conducted when the PVSS operates at 25 kW (0.4545 pu) before the frequency events for every level of unbalanced power. Figure 7.5(a) shows the results of the constant k_{iner} at 8 during the under-frequency events with different severities and Figure 7.5(b) demonstrates the results of the proposed control. Regarding the different severity of events, the system experiences higher ROCOF level and high deviation of the frequency from 60 Hz with increasing of the event severity (the L4 scenario has the highest ROCOF and highest frequency deviation from 60 Hz during the event). For all events, the PVSS provides active power support at high k_{iner} = 8 and then reduce the k_{iner} to 2 based on the proposed control, resulting in low active power oscillations for all levels of the event's severity compared to the constant k_{iner}. Figure 7.6(a) shows the results of the constant k_{iner} at 8 and Figure 7.6(b) shows the results of the proposed control during the over-frequency events. For all over-frequency scenarios, the PVSS absorbs active power based on k_{iner} = 8 to slow down ROCOF at the beginning of the event while reducing the event frequency. The active power oscillations can be reduced based on the proposed control compared to the constant k_{iner} for all levels of severity of the over-frequency event.

According to the results of different test scenarios, the effectiveness of the proposed control can be confirmed under various severities of both under-frequency and over-frequency events.

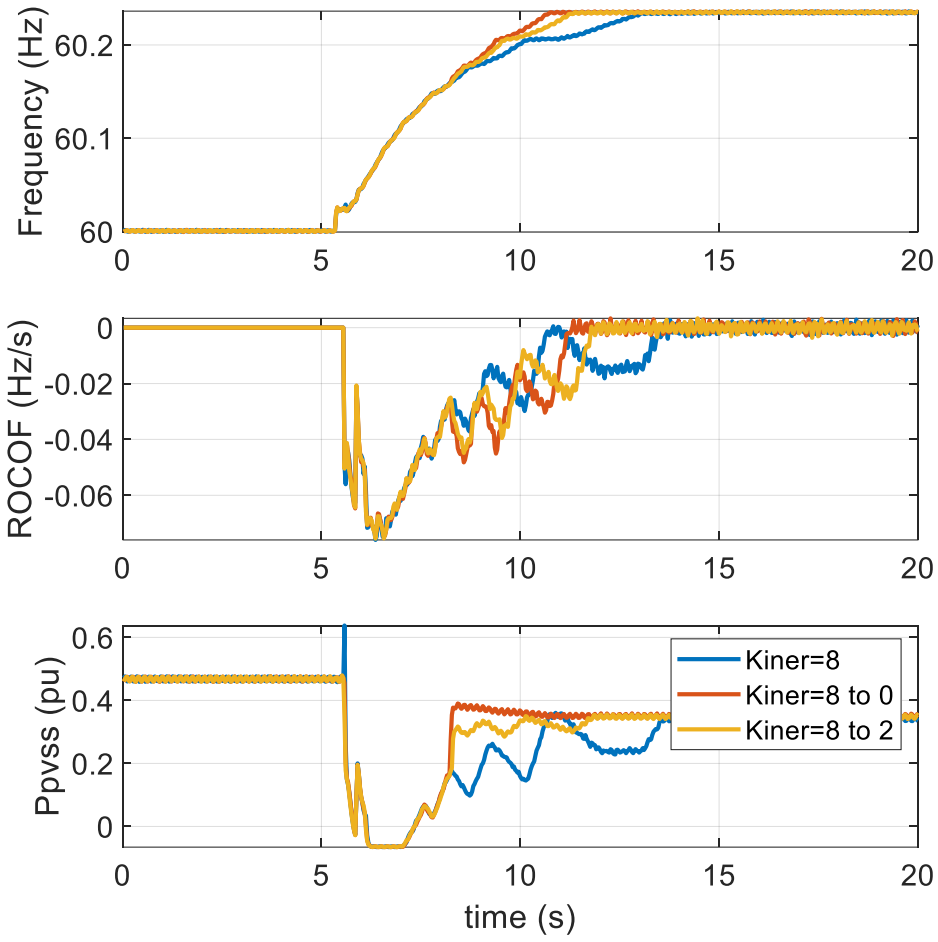

Figure 7.4: PVSS dynamics when adjusting k_{iner} during the over-frequency event.

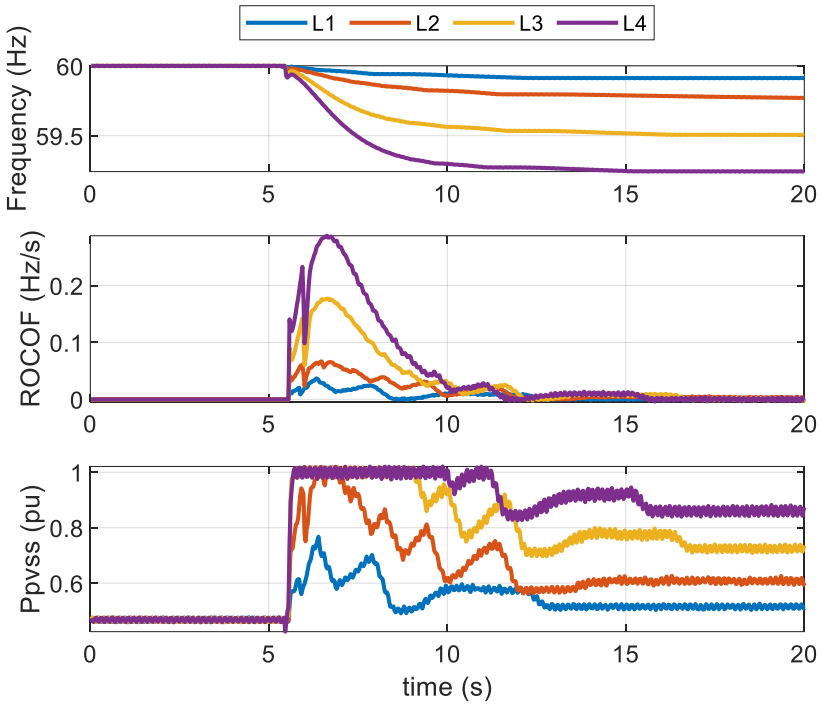

(a)

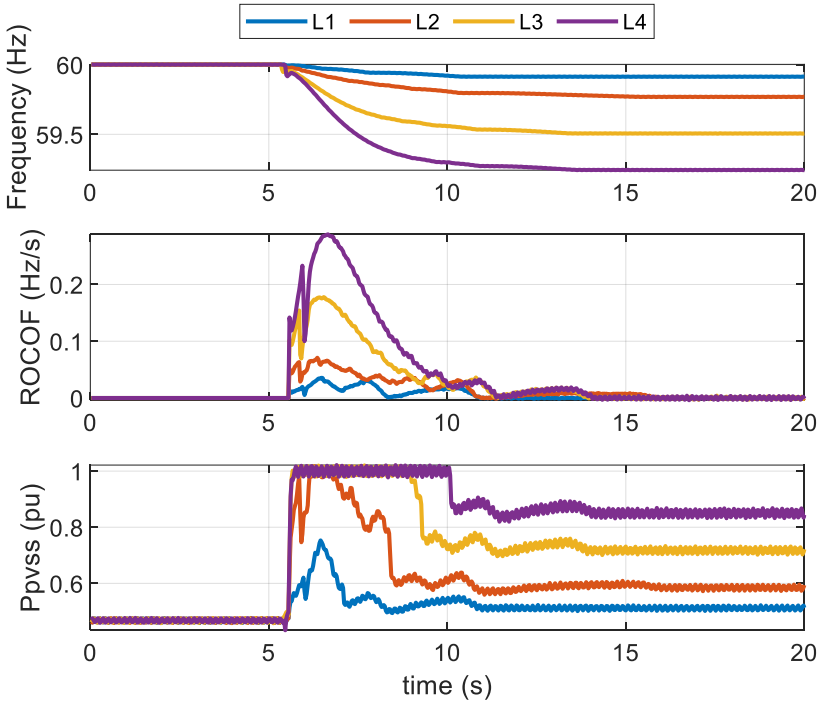

(b)

Figure 7.5: PVSS dynamics under different severities of under-frequency events. (a) Constant k_{iner} at 8 and (b) Adjusting k_{iner} from 8 to 2.

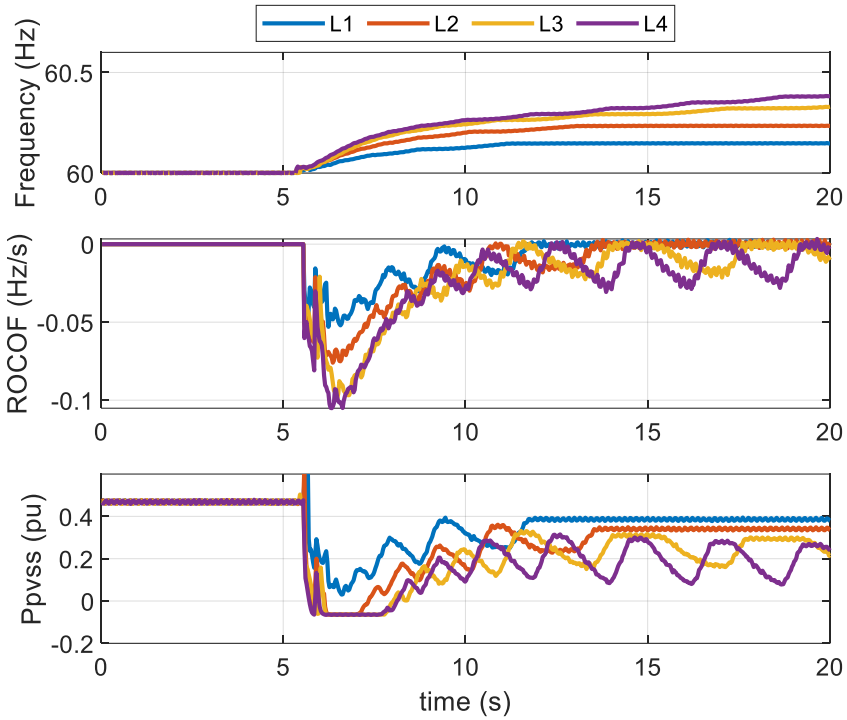

(a)

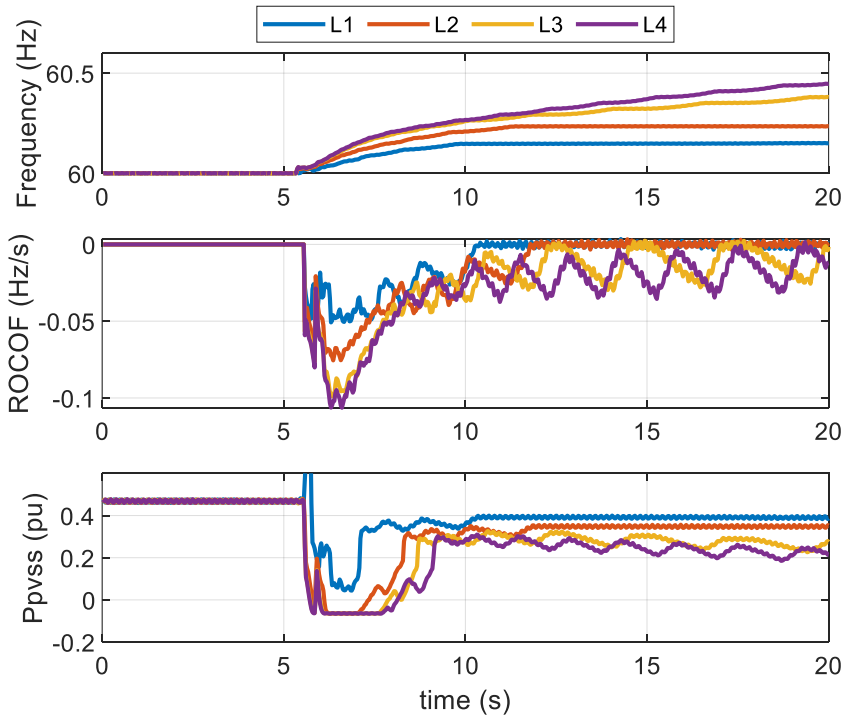

(b)

Figure 7.6: PVSS dynamics under different severities of over-frequency events. (a) Constant k_{iner} at 8 and (b) Adjusting k_{iner} from 8 to 2.

7.3.2 Experimental Results of Improvement of Frequency Recovery Service on HTB

The experiments are conducted on the HTB to verify the improvement of frequency recovery performance when implementing the bang-bang control based on [117], [118]. Figure 7.7 shows the comparison results during the frequency recovery period of an under-frequency event based on the traditional control with k_{iner} = 8, the bang-bang control with the adjustment of k_{iner} from 8 to 0, and the base case with k_{iner} = 0, which represents the case without inertia emulation. The frequency during the recovery of high k_{iner} based on the bang-bang control can ramp back to the nominal frequency value faster than the traditional control method, however, both controls have worsened performances than the case without providing inertia support during the frequency recovery period ($k_{iner} = 0$). This is because when the PVSS continues to inject power during the recovery period, it quickly drives the grid frequency out of the deadband and triggers the frequency regulation control to absorb active power, slowing down the frequency recovery process. Thus, additional control should be adopted to prevent the activation of frequency regulation control during the recovery process.

The study proposes to use the frequency control deadband (f_{db}) in addition to using the inertia deadband ($iner_{db}$) to deactivate the inertia emulation support provided by PVSS during the frequency recovery period. The experiment is conducted to verify the proposed control when implementing high k_{iner} with the bang-bang control in Figure 7.8 and Figure 7.9 for under-frequency event and over-frequency event, respectively. The proposed control uses both f_{db} and $iner_{db}$, whichever reaches first, to adjust the k_{iner} to be at 0 during the frequency recovery period. The current setup of f_{db} and $iner_{db}$ are at 0.036 Hz and 0.05 Hz/s, respectively. By using this proposed control, the frequency is back within the nominal condition at 5 s, which is less than 9 s from the control that only implements the $iner_{db}$ for the under-frequency scenario as shown in Figure 7.8. The test result under the over-frequency event in Figure 7.9 also confirmed that the frequency can return within its nominal operation faster by using the proposed control. The test results demonstrate that fast frequency recovery can be achieved with high k_{iner} and bang-bang control by using the f_{db} with the $iner_{db}$ to disable the inertia emulation support during the recovery period, without causing a delay in the frequency recovery process.

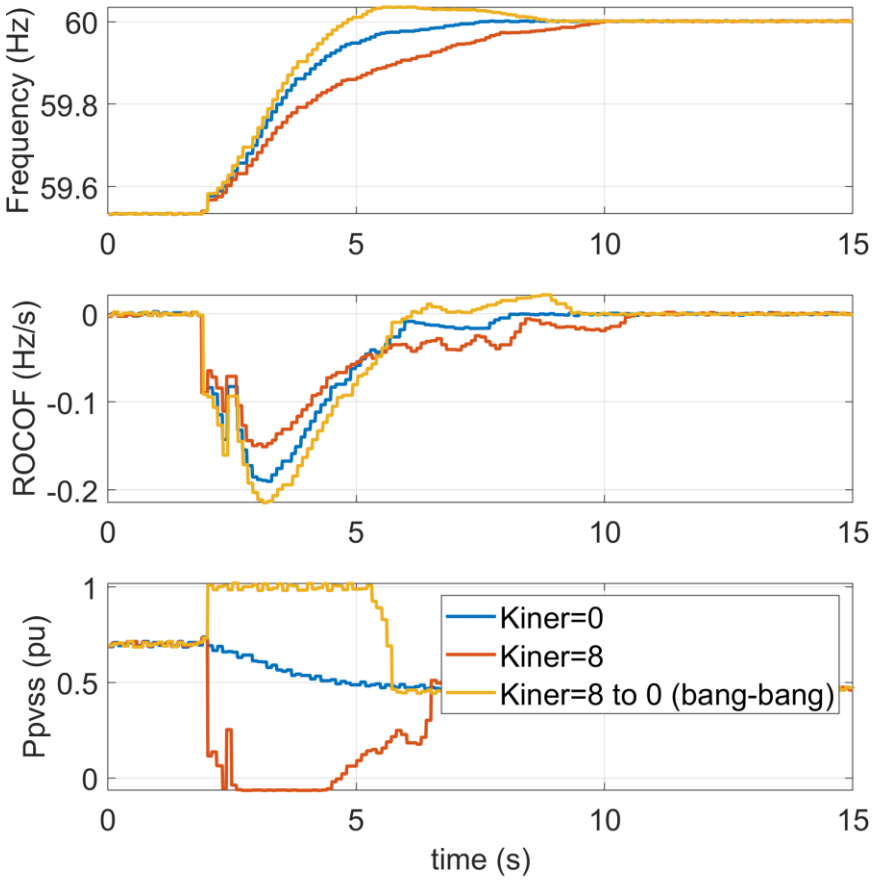

Figure 7.7: PVSS dynamics during the frequency recovery period of the under-frequency event based on the bang-bang control compared to the traditional inertia emulation control.

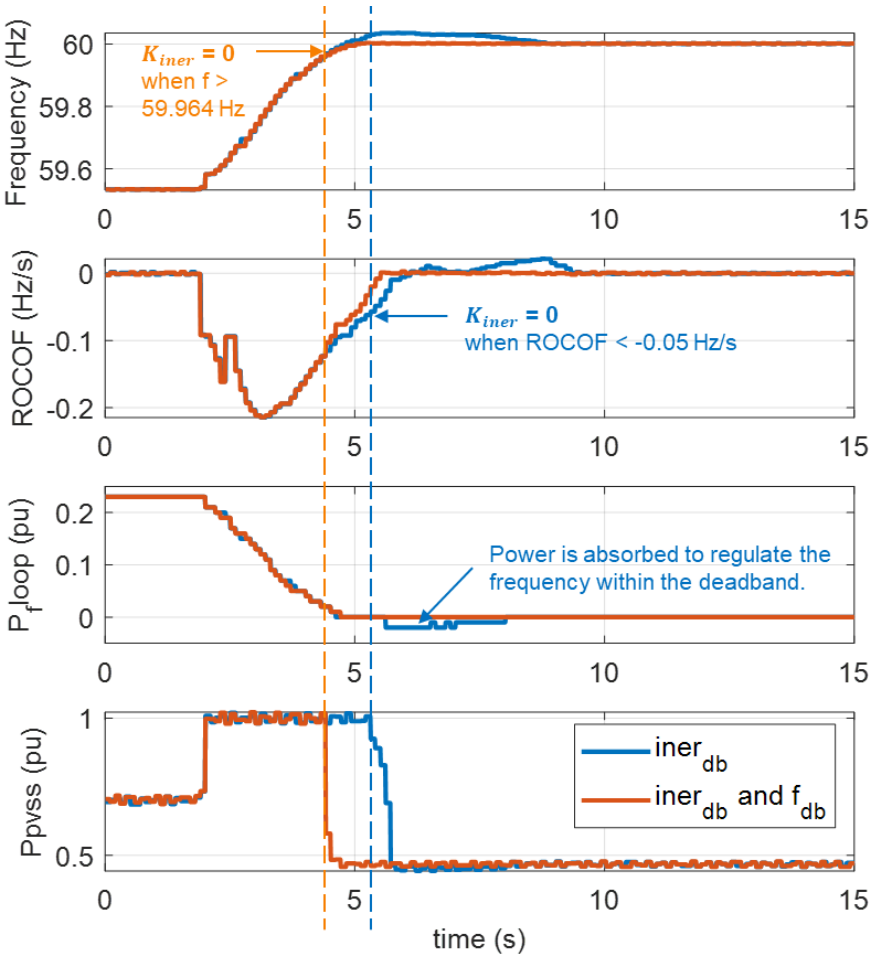

Figure 7.8: PVSS dynamics during frequency recovery of the under-frequency event based on bang-bang control without and with inertia deactivation.

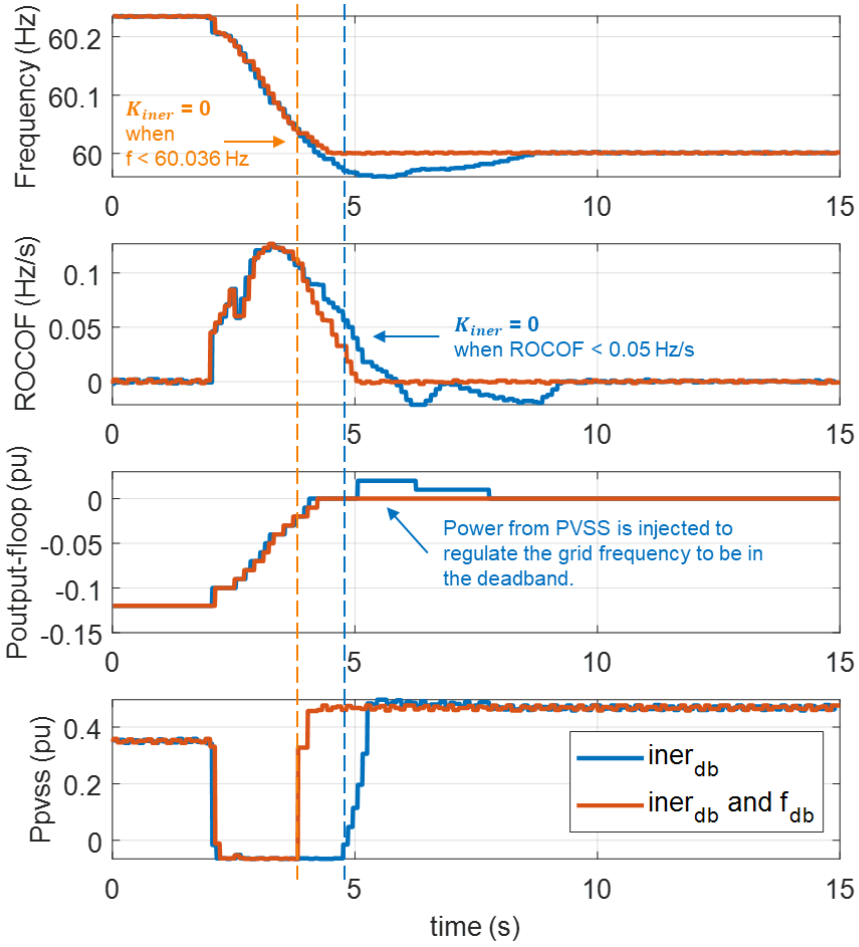

Figure 7.9: PVSS dynamics during frequency recovery of the over-frequency event based on bang-bang control without and with inertia deactivation.

7.3.2.1. Performance during Frequency Recovery at Different Operations of PVSS

The proposed control is evaluated when PVSS operates at different PV power outputs by comparing it to the control concept presented in [118]. The comparison results to the benchmark are provided and discussed below based on the event category and different PVSS operations.

- Under-frequency event

The PVSS operates at 12.5 kW and 25 kW before the under-frequency scenario. The SC will provide active power to the grid to increase the grid frequency during the event.

Figure 7.10 demonstrates the performance of the proposed control compared to the benchmark control during the under-frequency event with several event's severities. The proposed control has less frequency settling time than the benchmark, meaning that the frequency based on the proposed control can return to its normal operation more quickly. The results of when the PVSS operates at 12.5 kW is shown in Figure 7.10(a), in this case, the settling time of the proposed control is less than the benchmark ~1.75 s to 3 s based on the different severity of the event. For the case when PVSS operates at 25 kW, the settling time of the proposed control is less than the benchmark for every event severity ~0.57 s to 0.84 s as shown in Figure 7.10(b).

- Over-frequency event

The PVSS injects the PV power output of 12.5 kW and 50 kW into the grid before the over-frequency event. The PVSS absorbs active power from the grid to help reduce the frequency, while the SC is charged during the event.

The experimental results when the PVSS operates at 12.5 kW before the over-frequency event is shown in Figure 7.11(a). The results show that the proposed control has less frequency recovery settling time than the benchmark control in the range of 0.8 to 1.4 s under the different event's severity. Figure 7.11(b) shows the results of the test scenario when the PVSS operates at 50 kW before the event. In this test scenario, the proposed control also results in less frequency recovery settling time than the benchmark control ~0.3 to 0.6 s at low and medium event severities. For the highest event severity, both controls have a similar settling time of ~30 s regarding the dynamic of the high severity event that takes time to recover.

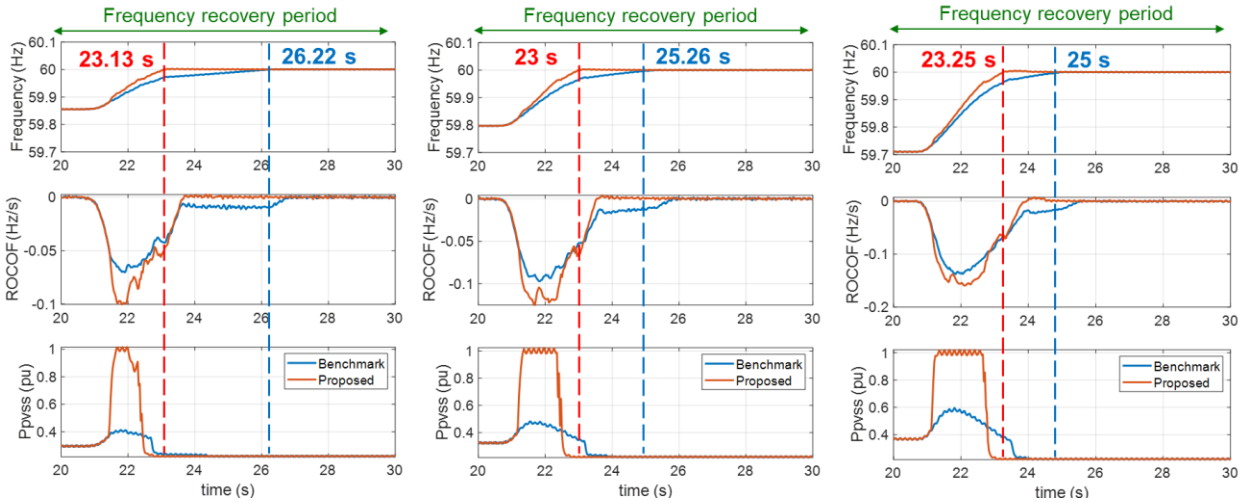

(a)

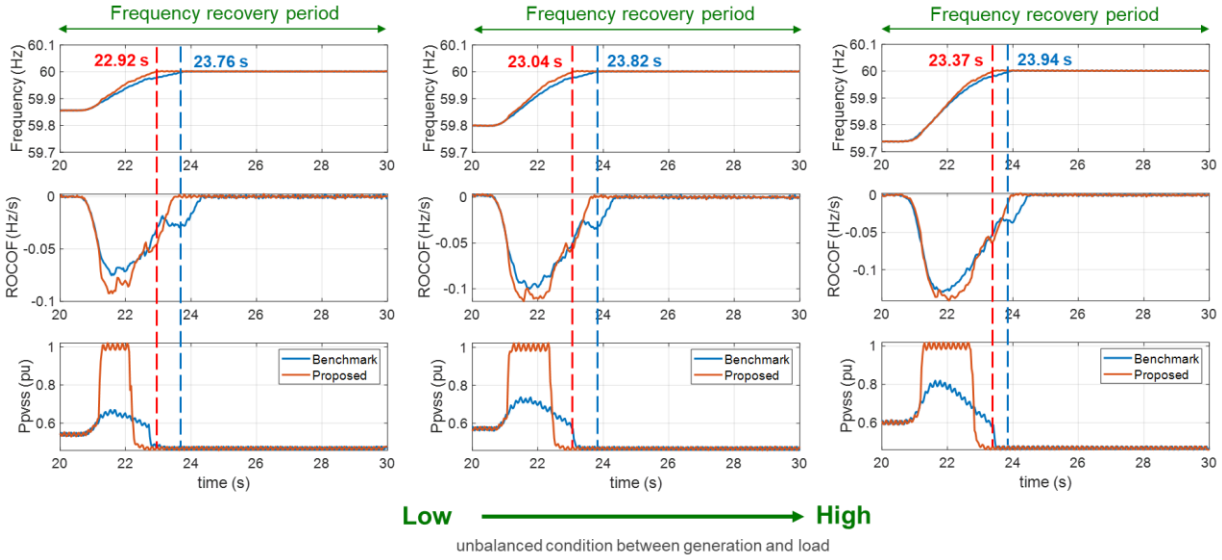

(b)

Figure 7.10: The frequency recovery time of the under-frequency event based on the benchmark control [118] and the proposed control at different PV operations (a) 12.5 kW and (b) 25 kW.

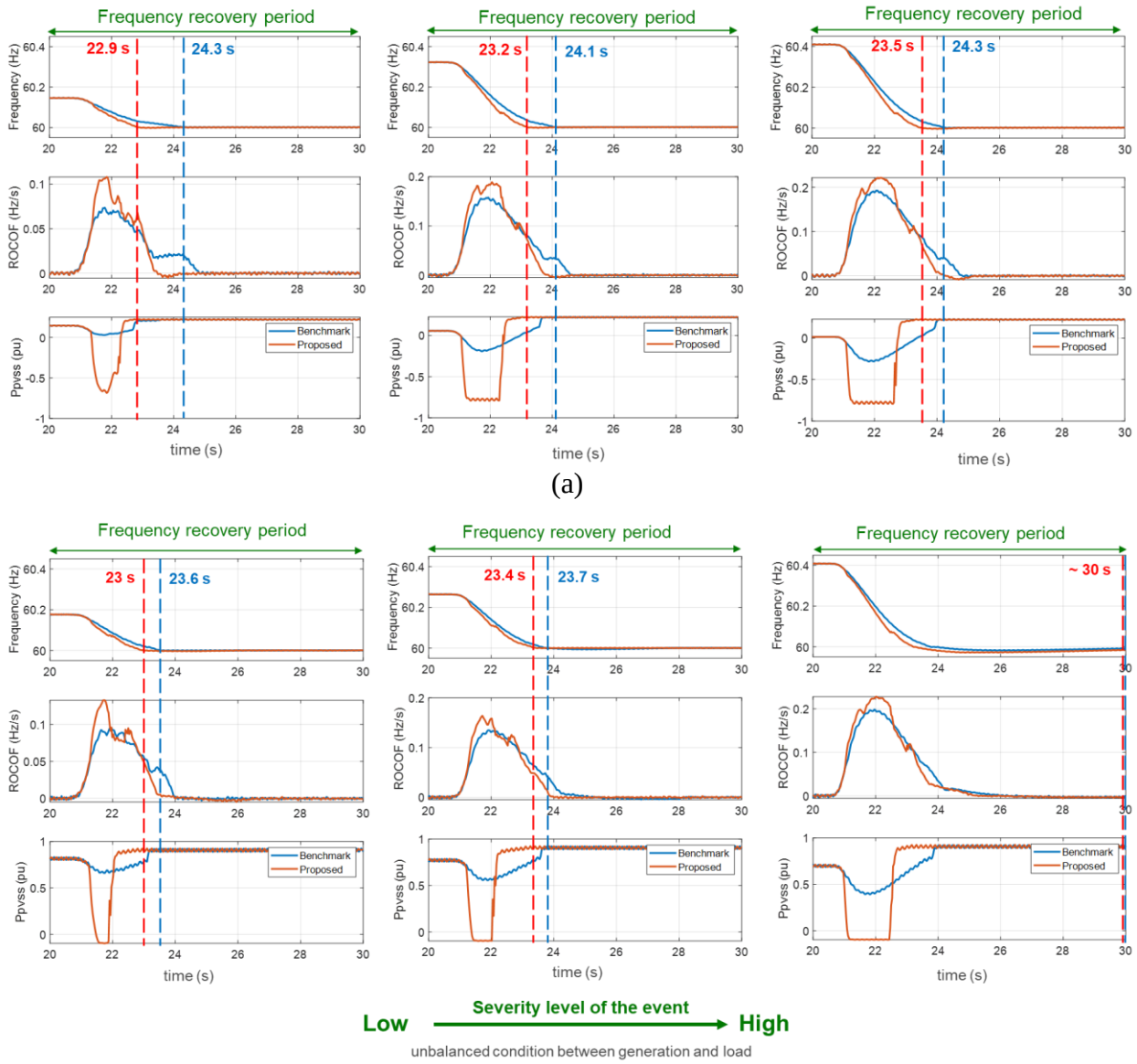

Figure 7.11: The frequency recovery time of the over-frequency event based on the benchmark control [118] and the proposed control at different PV operations (a) 12.5 kW and (b) 50 kW.

The test scenarios based on different PVSS operations at several event severities confirm that the frequency can return to its normal operation quicker using the proposed control rather than the benchmark control because the PVSS provides more power support during the recovery period.

7.3.3 Impact of SC's SOC on Fast Frequency Support provided by PVSS

The SC has a limited energy capacity; thus, its services will be interrupted when the SC's SOC reaches its voltage or SOC limits during the event. This section demonstrates the impact of the SC's SOC on fast frequency support provision.

Both under-frequency and over-frequency test scenarios are conducted to illustrate the impact of SC's SOC on the performance of providing frequency support by using the proposed controls presented in previous sections. The comparison between the case with sufficient SC capacity and the case with insufficient SC capacity is provided and discussed below.

For the under-frequency event scenarios, the PV operates at 25 kW before the event happens at ~6 s, as depicted in Figure 7.12. The SC injects active power to provide inertia and frequency support to slow down the ROCOF and regulate the system's frequency. The inertia support of the case with insufficient SC is interrupted when the SC's SOC reaches its lower limit. When SC can no longer provide active power, it results in higher ROCOF and a reduction in frequency regulation performance compared to the case with sufficient SC's SOC. Also, the frequency of the case with insufficient SC's SOC takes longer to return to its nominal operation because the SC cannot provide the active power to support the recovery period based on the proposed control. Even though the PVSS can remain connected to the grid and maintain the PV operation at 25 kW after the SC is out of capacity, the performance of the services in terms of inertia support, frequency regulation, and fast frequency recovery are reduced due to the SC reaches its capacity during the support.

Figure 7.13 demonstrates the over-frequency event that happens at ~ 6 s when the PV operates at 12.5 kW, and the SC will absorb active power during the event. The SC of the case with insufficient SC capacity cannot continue to absorb active power during the event starting from ~6.2 s, resulting in increased ROCOF and reduced frequency regulation performance. In this case,

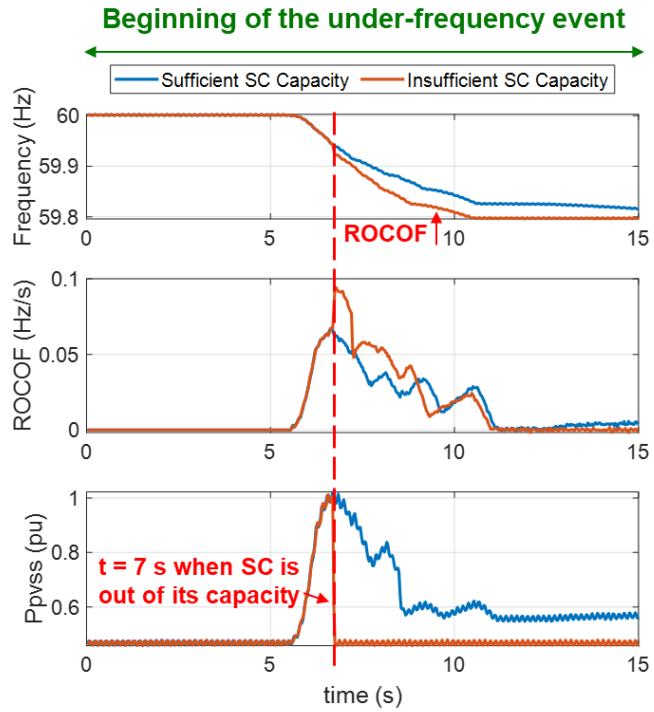

(a)

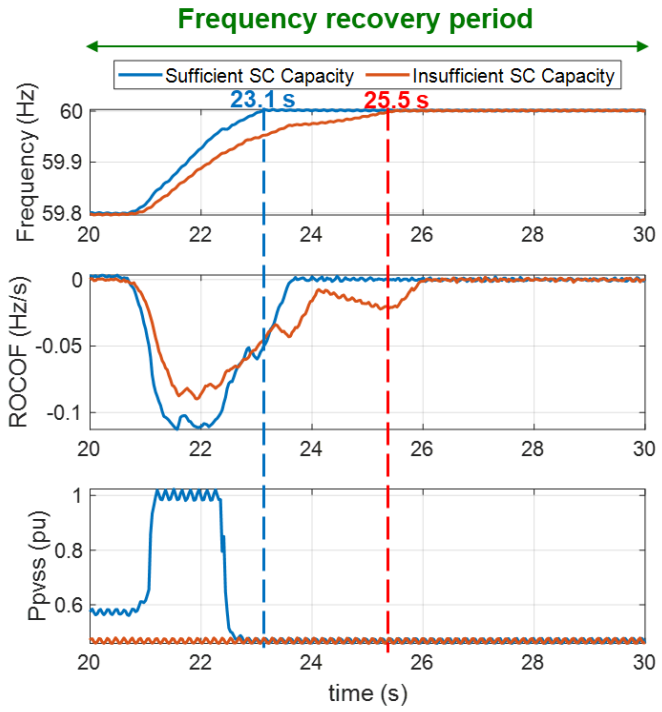

(b)

Figure 7.12: Impact of the SC's SOC on the performance of fast frequency support during the under-frequency event at (a) the beginning of the event and (b) the recovery period.

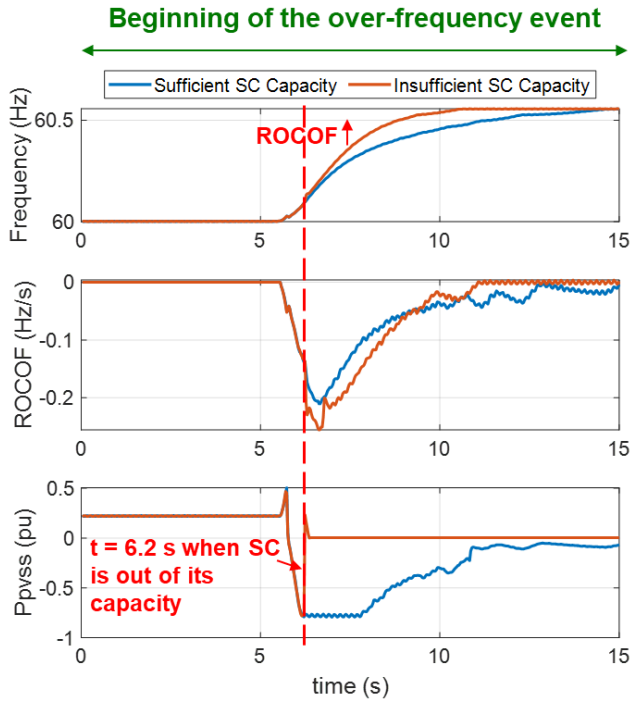

(a)

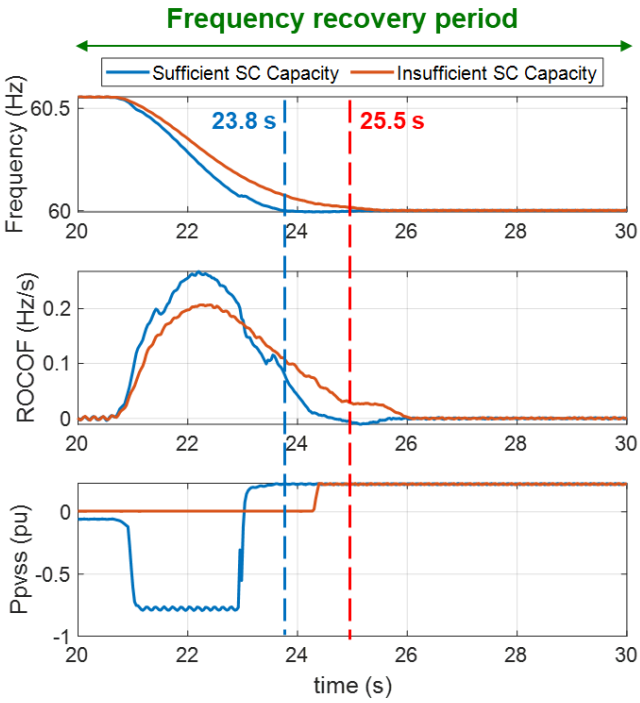

(b)

Figure 7.13: Impact of the SC's SOC on the performance of fast frequency support during the over-frequency event at (a) the beginning of the event and (b) the recovery period.

the PV needs to curtail its power generation to provide frequency support and remain connected to the grid during the event. The provision performance in terms of inertia emulation, frequency regulation, and frequency recovery is reduced compared to the case with sufficient SC capacity.

7.4 Conclusion

This chapter presents fast frequency support focusing on an inertia emulation provided by PVSS. The inertia emulation control can be effectively achieved with less power oscillations by implementing the k_{iner} adjustment. In addition, the study proposes the control of PVSS to provide fast frequency recovery support without causing a delay in the recovery period.

The experiments are conducted to verify the effectiveness of the proposed control for both under-frequency and over-frequency scenarios. The performance of the proposed control is also verified under different PVSS operations and event's severity. The proposed control can provide a better fast frequency recovery service compared to the benchmark control. The impact of the SC's SOC on the performance of the proposed control is demonstrated. Since the SC's energy capacity is limited, the performance in providing fast frequency support is greatly impacted when the SC does not have sufficient capacity for the event.

Chapter 8
Conclusion and Future Work

8.1 Summary

This dissertation studies PVSS dynamics under grid support scenarios including voltage support, frequency support, and fault ride-through operations. In Chapter 3, the development of the PVSS emulator on HTB is presented. The SC model adopted in the HTB emulator is selected for its capacity to accurately represent SC dynamics during transient and long-term events with moderate computational requirements.

The accuracy of the emulator is verified through comparison with results from the simulation model under short-term grid support events. These experiments are conducted on the HTB platform, where VSCs are used to emulate each subsystem under test including synchronous generator, load, and PVSS. The experimental results align with the results from the simulation under the same test scenarios. This can ensure that the developed HTB emulator can accurately represent the PVSS dynamics under different power system scenarios. The developed HTB emulator can accommodate different test systems, both standalone and in hybrid configurations with other types of energy storage technologies. This extends the testing capabilities to represent systems with SC applications in the HTB.

SC's availability is an important factor in ensuring PV system stability during severe LVRT operations when the PV system stability is vulnerable. Since SC has limited energy capacity, the SC's SOC management is studied to ensure its capacity to support the PV system during LVRT operations in Chapter 4. The SOC reservation control is proposed to ensure that the SC has sufficient capacity to support the PV system during LVRT operations. The proposed control calculates the SC capacity according to current PV operations and the LVRT requirements following the IEEE-1547 standard. This approach ensures that the SC will have sufficient capacity to support the PV system during LVRT operations. Thus, the SC capacity can be efficiently utilized compared to the traditional reserved control at fixed reserved SC capacity.

This study also proposed the SC's SOC management to consider the SC thermal capacity to adjust the SC current during the management. This approach enables a shorter management time compared to the control without adjusting the SC current based on its thermal capability. The proposed control can maximize SC thermal capability while ensuring the safe operations of SC. Grid voltage conditions are considered to adjust the reference power during SOC management to prevent worsening grid conditions. Thus, safe operations of both systems can be ensured.

Chapter 5 explores the reactive power allocation of DERs based on the TE approach when considering the limitations of their locations and the cost of providing reactive power support. The study incorporates the impact of DER's location on voltage improvement at the target location in the DER's supply curve, utilizing the voltage sensitivity factor. Consequently, reactive power dispatch based on the TE approach can be done more efficiently compared to the method that does not consider a DER's location.

The effectiveness of the modified DER's supply curve is verified by conducting simulation verification on the IEEE 123-node test feeder. Results show that when DERs dispatch their reactive power based on the modified DER's supply curve, the voltage at the target location can be adjusted accordingly. The modified DER's supply curve prioritizes DERs with greater impact on voltage with a lower cost of providing reactive power to provide reactive power support. Additionally, power loss analysis is performed to ensure no significant change in the system's losses when dispatching reactive power based on the proposed method.

Due to the challenge presented by the standard IEEE1547.9-2022 revision [50] in LVRT operations of grid-connected energy storage systems, it is recommended that the grid-connected energy storage systems should be able to provide LVRT operations based on Category III. The PVSS will have to reserve more SC's capacity to ensure that the SC can provide LVRT services longer than Category II, as presented in Chapter 4. The proposed reserve SOC control might not be feasible under the updated requirements. Thus, the LQR regulator-based controller is proposed in Chapter 6 to address a control mode switching of PVSS when SC is fully charged during fault. The proposed control can reduce the transient DC-link overvoltage during the control mode transition, ensuring the PVSS stability under severe LVRT operations.

Regarding the work presented in Chapter 3 for fast frequency support provided by the PVSS, the study is extended in Chapter 7. Inertia emulation is the focus of this chapter. The

adaptive inertia emulation control is adopted to change the inertia coefficient according to the duration of the frequency event and the event's ROCOF. The control is modified from what has been previously proposed in the literature to include the ability to provide fast-frequency recovery service to the system. The proposed control can help the frequency return to its normal operation quickly, improving the overall fast frequency support provided by the PVSS.

8.2 Contributions

The contributions of this dissertation are summarized as follows:

- Development of a PVSS emulator on the HTB platform to demonstrate its dynamics under grid support scenarios. The emulator accuracy to represent the PVSS dynamics is confirmed through comparison with simulation results from Simulink under similar scenarios.
- Investigate PVSS dynamics under short-term grid ancillary services including voltage support, fast frequency support, and LVRT operations.
- Development of SOC management control considering LVRT operations to ensure the SC's ability to provide support according to the IEEE-1547 standard requirements. The proposed method considers grid conditions and PVSS operations to ensure the safe operations of both systems while maximizing the PVSS capacity to provide support to the system.
- Propose reactive power allocation of DERs when providing voltage support based on the TE approach. The proposed method considers the cost of providing reactive power support and DERs' locations in the system to efficiently achieve reactive power dispatch based on the TE approach.
- Development of a LQR based controller to reduce the transient of DC-link overvoltage during control mode switching when the SC reaches its SOC limit during LVRT operation.
- Investigate the PVSS dynamics based on the adjustment of inertia coefficient during fast frequency support event. The revision of the control is proposed to provide fast

frequency recovery service to the system. The proposed control is validated on the HTB to evaluate its performance under different conditions of the grid and the PVSS.

8.3 Future Works

8.3.1 Development of Hybrid SC Model on HTB

Hybrid supercapacitor battery is another SC technology gaining more attention in electric vehicles and grid applications [119]. This hybrid supercapacitor has a higher energy capacity than the EDLC type while maintaining the high-power capability of the EDLC type. However, adopting the hybrid type is still limited due to the high cost and technology maturity [120]. With the advancement of hybrid SC technology, its cost will become competitive with other SC technologies, as can be seen by the increasing availability of commercial hybrid SC products nowadays. Since the hybrid SC has different characteristics from the EDLC types, the EDLC model cannot represent the hybrid SC dynamics due to the differences in RC time constant and different SOC characteristics [121].

The development of the hybrid SC emulator, in addition to the SC model (EDLC type) developed in this work, can be useful for future studies on the HTB related to EVs and power grid applications.

8.3.2 Grid Support Services Considering SC's SOC

Based on the IEEE1547.9-2022 revision [50] for energy storage systems, it can be seen that most of the grid support requirements are extended from the IEEE 1547-2018 requirement [18] in terms of longer support time, higher level of support, and extended support at higher severity of the event. Because the SC has a limited energy capacity, the SC might not be able to support the event for a long time. So, the SC's SOC might need to be considered to adjust the support power to the grid to ensure that the PVSS can comply with the IEEE-1547 requirements. Another consideration is to design the SC control based on the type of the grid event. For example, the SC can provide pulse power to the system, so it is suitable for providing maximum inertia support to help reduce ROCOF during the event. However, it might not be able to support regulating the grid frequency for a long time. The support event type is essential to determining

which event the SC can most contribute to when considering its limited capacity. Future work can be done to demonstrate the control of SC based on the priority of the event in which it needs to participate.

References

[1] Y. Lin *et al.*, "Research roadmap on grid-forming inverters," National Renewable Energy Laboratory, Tech. Report. NREL/TP-5D00-73476, 2020.

[2] U.S. Energy Information Administration, "EIA - Annual energy outlook 2023," Sept. 2023. [Online]. Available: https://www.eia.gov/outlooks/aeo/

[3] A. Anzalchi and A. Sarwat, "Overview of technical specifications for grid-connected photovoltaic systems," *Energy Conversion and Management*, vol. 152, pp. 312–327, Nov. 2017.

[4] North American Electric Reliability Corporation (NERC), "An introduction to inverter-based resources on the bulk power system," Sept. 2023. [Online]. Available: https://www.nerc.com/pa/ Documents/2023_NERC_Guide_Inverter-Based-Resources.pdf

[5] U.S. Department of Energy, "Technology strategy assessment -methodology," Sept. 2023. [Online]. Available: https://www.energy.gov/oe/storage-innovations-2030

[6] G. Navarro, J. Torres, M. Blanco, J. Nájera, M. Santos-Herran, and M. Lafoz, "Present and future of supercapacitor technology applied to powertrains, renewable generation and grid connection applications," *Energies*, vol. 14, no. 11, 2021.

[7] M. E. Sahin, F. Blaabjerg, and A. Sangwongwanich, "A comprehensive review on supercapacitor applications and developments," *Energies*, vol. 15, no. 3, p. 674, Jan. 2022.

[8] N. Palla and V. Seshadri Sravan Kumar, "Coordinated control of PV-ultracapacitor system for enhanced operation under variable solar irradiance and short-term voltage dips," *IEEE Access*, vol. 8, pp. 211809–211819, 2020.

[9] A. M. Gross et al., "Energy management in converter-interfaced renewable energy sources through ultracapacitors for provision of ancillary services," *International Conference on Smart Energy Systems and Technologies (SEST)*, Vaasa, Finland, 2021.

[10] D. Somayajula and M. L. Crow, "An ultracapacitor integrated power conditioner for intermittency smoothing and improving power quality of distribution grid," *IEEE Transactions on Sustainable Energy*, vol. 5, no. 4, pp. 1145-1155, Oct. 2014.

[11] F. Naseri, S. Karimi, E. Farjah, and E. Schaltz, "Supercapacitor management system: a comprehensive review of modeling, estimation, balancing, and protection techniques," *Renewable and Sustainable Energy Reviews*, vol. 155, Mar. 2022.

[12] U.S. Department of Energy, “Technology strategy assessment- supercapacitors,” September 2023. [Online]. Available: https://www.energy.gov/oe/storage-innovations-2030

[13] K. N. D. Malamaki, D. Gkontoras, and C. S. Demoulias, “Ramp-rate limitation of distributed renewable energy sources via supercapacitors as preventive action towards frequency disturbances,” *International Conference on Energy Transition in the Mediterranean Area*, Thessaloniki, Greece, 2022.

[14] S. Karpana, E. Batzelis, S. Maiti, and C. Chakraborty, “PV-supercapacitor cascaded topology for primary frequency responses and dynamic inertia emulation,” *Energies*, vol. 14, no. 24, Dec. 2021.

[15] P. Kritprajun *et al.*, “Development of a converter-based supercapacitor system emulator for PV applications,” *IEEE Energy Conversion Congress and Exposition (ECCE)*, Nashville, TN, USA, 2023.

[16] H. Miniguano, A. Barrado, C. Fernández, P. Zumel, and A. Lázaro, “A general parameter identification procedure used for the comparative study of supercapacitors models,” *Energies*, vol. 12, no. 9, 2019.

[17] M. E. Sahin, F. Blaabjerg and A. Sangwongwanich, “Modelling of supercapacitors based on simplified equivalent circuit,” *CPSS Transactions on Power Electronics and Applications*, vol. 6, no. 1, pp. 31-39, March 2021.

[18] “IEEE Standard for Interconnection and Interoperability of Distributed Energy Resources with Associated Electric Power Systems Interfaces,” IEEE Std 1547-2018 (Revision of IEEE Std 1547-2003), pp.1-138, 6 April 2018.

[19] I. Hamdan, A. Maghraby, and O. Noureldeen, “Stability improvement and control of grid-connected photovoltaic system during faults using supercapacitor,” *SN Applied Sciences*, vol. 1, no. 12, pp. 1–19, 2019.

[20] B. R. Naidu, P. Bajpai, and C. Chakraborty, “Energy storage unit for dynamic voltage support in distribution networks,” *IEEE International Conference on Power Systems (ICPS)*, Kharagpur, India, 2021.

[21] M. J. E. Alam, A. Somani, R. B. Melton, and T. E. McDermott, “Transactive approach for engaging distribution network assets for voltage management in southern California Edison distribution feeders,” Pacific Northwest National Laboratory, Tech. Report. PNNL-27650, 2018.

[22] J. Dong et al., “Integrating transactive energy into reliability evaluation for a self-healing distribution system with microgrid,” *IEEE Transactions on Sustainable Energy*, vol. 13, no. 1, pp. 122-134, Jan. 2022.

[23] B. P. Bhattarai et al., “Enhancing distribution system resiliency through a novel transactive energy systems framework,” *IEEE Power & Energy Society General Meeting (PESGM),* Atlanta, GA, USA, 2019.

[24] P. Kritprajun et al., “Reactive power allocation of PV inverters for voltage support in power systems based on transactive energy approach,” *IEEE Energy Conversion Congress and Exposition (ECCE),* Vancouver, BC, Canada, 2021.

[25] R. T. Yadlapalli, R. K. R. Alla, R. Kandipati, and A. Kotapati, “Supercapacitors for energy storage: progress, applications and challenges,” in *Journal of Energy Storage*, vol. 49, May 2022.

[26] J. Rocabert, R. Capó-Misut, R. S. Muñoz-Aguilar, J. I. Candela and P. Rodriguez, “Control of energy storage system integrating electrochemical batteries and supercapacitors for grid-connected applications,” *IEEE Transactions on Industry Applications*, vol. 55, no. 2, pp. 1853-1862, 2019.

[27] S. Liu, L. Wei, and H. Wang, “Review on reliability of supercapacitors in energy storage applications,” *Applied Energy*, vol. 278, 2020.

[28] Q. Hassan, M. Jaszczur, A. M. Abdulateef, J. Abdulateef, A. Hasan, and A. Mohamad, “An analysis of photovoltaic/supercapacitor energy system for improving self-consumption and self-sufficiency,” *Energy Reports*, vol. 8, pp. 680–695, 2022.

[29] D. Benavides, P. Arévalo, J. A. Aguado, and F. Jurado, “Experimental validation of a novel power smoothing method for on-grid photovoltaic systems using supercapacitors,” *International Journal of Electrical Power & Energy Systems*, vol. 149, July 2023.

[30] L. G. González, R. Chacon, B. Delgado, D. Benavides, and J. Espinoza, “Study of energy compensation techniques in photovoltaic solar systems with the use of supercapacitors in low-voltage networks,” *Energies*, vol. 13, no. 15, p. 3755, Jul. 2020.

[31] K. N. D. Malamaki, G. C. Kryonidis and C. S. Demoulias, “Comparative evaluation of ramp-rate limitation control strategies employing supercapacitors,” *IEEE 21st Mediterranean Electrotechnical Conference,* 2022.

[32] L. R. Visser, E. M. B. Schuurmans, T. A. AlSkaif, H. A. Fidder, A. M. van Voorden, and

W. G. J. H. M. van Sark, “Regulation strategies for mitigating voltage fluctuations induced by photovoltaic solar systems in an urban low voltage grid,” *International Journal of Electrical Power & Energy Systems*, vol. 137, May 2022.

[33] G. C. Kryonidis et al., “Use of ultracapacitor for provision of inertial response in virtual synchronous generator: design and experimental validation,” *Electrical Power Systems Research*, vol. 223, Oct. 2023.

[34] R. K. Sarojini and P. Kaliannan, “Inertia emulation through supercapacitor for a weak grid,” *IEEE Access*, vol. 9, pp. 30793-30802, 2021.

[35] J. Kim *et al*., “Supercapacitor to provide ancillary services with control coordination,” *IEEE Transactions on Industry Applications*, vol. 55, no. 5, pp. 5119-5127, 2019.

[36] N. B. G. Brinkel et al., “Impact of rapid PV fluctuations on power quality in the low-voltage grid and mitigation strategies using electric vehicles,” *International Journal of Electrical Power & Energy Systems*, vol. 118, June 2020.

[37] K. N. D. Malamaki et al., “Ramp-rate limitation control of distributed renewable energy sources via supercapacitors,” *IEEE Transactions on Industry Applications*, vol. 58, no. 6, pp. 7581–7594, 2022.

[38] G. Wang, M. Ciobotaru, and V. G. Agelidis, “Power smoothing of large solar PV plant using hybrid energy storage,” *IEEE Transactions on Sustainable Energy*, vol. 5, no. 3, pp. 834–842, July 2014.

[39] G. C. Kryonidis, A. I. Nousdilis, K. D. Pippi and T. A. Papadopoulos, “Impact of power smoothing techniques on the long-term performance of battery energy storage systems,” *International Universities Power Engineering Conference (UPEC)*, 2021.

[40] M. Talha, S. R. S. Raihan, and N. A. Rahim, “A grid-tied PV inverter with sag-severity-independent low-voltage ride through, reactive power support, and islanding protection,” *Journal of Modern Power Systems and Clean Energy*, vol. 9, no. 6, pp. 1300–1311, November 2021.

[41] V. L. Srinivas, B. Singh, and S. Mishra, “Fault ride-through strategy for two-stage grid-connected photovoltaic system enabling load compensation capabilities,” *IEEE Transactions on Industrial Electronics*, vol. 66, no. 11, pp. 8913–8924, Nov. 2019.

[42] Y. Zhu, H. Wen, G. Chu, Y. Hu, X. Li and J. Ma, “High-performance photovoltaic constant power generation control with rapid maximum power point estimation,” *IEEE Transactions*

on Industry Applications, vol. 57, no. 1, pp. 714-729, 2021.

[43] P. Kritprajun et al., "State of charge management for grid-connected PV with supercapacitor system considering LVRT operation," *IEEE Energy Conversion Congress and Exposition*, Nashville, TN, USA, 2023.

[44] M. C. Argyrou, "Hybrid battery-supercapacitor mathematical modeling for PV application using MATLAB/Simulink," *International Universities Power Engineering Conference (UPEC)*, 2018.

[45] L. Kong, J. Yu, and G. Cai, "Modeling, control and simulation of a photovoltaic /hydrogen/ supercapacitor hybrid power generation system for grid-connected applications," *International Journal of Hydrogen Energy*, vol. 44, no. 46, pp. 25129–25144, 2019.

[46] S. Pezzolato, "Modeling and model validation of supercapacitors for real-time simulations." M. S. thesis, University of Bologna, 2019.

[47] M. Krpan, I. Kuzle, A. Radovanovic, and J. V. Milanovic, "Modelling of supercapacitor banks for power system dynamics studies," *IEEE Transactions on Power Systems*, vol. 36, no. 5, pp. 3987–3996, 2021.

[48] M. Ergin Sahin and F. Blaabjerg, "A hybrid PV-battery/ supercapacitor system and a basic active power control proposal in MATLAB/Simulink," *Electronics*, vol. 9, no. 1, p. 129, Jan. 2020.

[49] NERC, "Fast frequency response concepts and bulk power system reliability needs," June 2023. [Online]. Available: https://www.nerc.com/comm/PC/InverterBased Resource Performance Task Force.

[50] "IEEE Guide for Using IEEE Std 1547 for Interconnection of Energy Storage Distributed Energy Resources with Electric Power Systems," in IEEE Std 1547.9-2022, pp.1-87, 5 Aug. 2022.

[51] J. Giraldez, M. Emmanuel, A. Hoke, and S. Suryanarayanan, "Impacts of voltage-based grid-support functions on energy production of PV customers." *IEEE Power & Energy Society General Meeting*, Atlanta, GA, USA, 2019.

[52] L. M. Tolbert et al., "Reconfigurable real-time power grid emulator for systems with high penetration of renewables," *IEEE Open Access Journal of Power and Energy*, vol. 7, pp. 489-500, 2020.

[53] J. Sun, "Data center power system emulation and GaN-based high-efficiency rectifier with

reactive power regulation." PhD dissertation, University of Tennessee, 2022.

[54] Y. Ma, "Virtual synchronous generator operation of full converter wind turbine – control and testing in a hardware based emulation platform." PhD dissertation, University of Tennessee, 2019.

[55] Y. Ma, L. Yang, J. Wang, F. Wang, and L. M. Tolbert, "Emulating full-converter wind turbine by a single converter in a multiple converter based emulation system," *IEEE Applied Power Electronics Conference and Exposition*, Fort Worth, TX, USA, 2014, pp. 3042-3047.

[56] L. Yang et al., "Three-phase power converter-based real-time synchronous generator emulation," *IEEE Transactions on Power Electronics*, vol. 32, no. 2, pp. 1651-1665, Feb. 2017.

[57] J. Wang, L. Yang, C. Blalock, and L. M. Tolbert, "Flywheel energy storage emulation using reconfigurable hardware test-bed of power converters," *IEEE Electrical Energy Storage Applications and Technologies*, Oct. 2013.

[58] J. D. Boles, Y. Ma, J. Wang, D. Osipov, L. M. Tolbert and F. Wang, "Converter-based emulation of battery energy storage systems (BESS) for grid applications," *IEEE Transactions on Industry Applications*, vol. 55, no. 4, pp. 4020-4032, 2019.

[59] J. Wang et al., "Static and dynamic power system load emulation in converter-based reconfigurable power grid emulator," *IEEE Energy Conversion Congress and Exposition*, Pittsburgh, PA, USA, 2014.

[60] J. Sun, S. Wang, J. Wang and L. M. Tolbert, "Dynamic model and converter-based emulator of a data center power distribution system," *IEEE Transactions on Power Electronics*, vol. 37, no. 7, pp. 8420-8432, July 2022.

[61] S. Wang, Y. Ma, J. Wang, L. M. Tolbert and F. Wang, "Variable speed drive connected motor load emulator for a multi-converter-based hardware testbed system," *IEEE Open Journal of Industry Applications*, vol. 2, pp. 337-346, 2021.

[62] G. Rancilio, A. Rossi, C. D. Profio, M. Alborghetti, A. Galliani, and M. Merlo, "Grid-scale BESS for ancillary services provision: SoC restoration strategies," *Applied Sciences*, vol. 10, no. 12, p. 4121, Jun. 2020.

[63] P. Iurilli, C. Brivio, and M. Merlo, "SoC management strategies in battery energy storage system providing primary control reserve," *Sustainable Energy, Grids and Networks*, vol. 19, Sep. 2019.

[64] C. Jamroen, “The effect of SoC management on economic performance for battery energy storage system in providing voltage regulation in distribution networks,” *Electric Power System Research,* vol. 211, Oct. 2022.

[65] A. M. Gross et al., “Energy management in converter-interfaced renewable energy sources through ultracapacitors for provision of ancillary services,” *Sustainable Energy, Grids and Networks,* Dec. 2022.

[66] Z. Tan, X. Li, L. He, Y. Li, and J. Huang, “Primary frequency control with BESS considering adaptive SoC recovery,” International Journal Electrical Power & Energy Systems, vol. 117, May 2020.

[67] B. Gundogdu, D. T. Gladwin, and D. A. Stone, “Battery SOC management strategy for enhanced frequency response and day-ahead energy scheduling of BESS for energy arbitrage,” *Annual Conference of the IEEE Industrial Electronics Society*, 2017.

[68] Maxwell Technologies, “Product Guide Maxwell Technologies: BOOSTCAP Ultracapacitor,”2009. [Online]. Available: https://maxwell.com/products/ultracapacitors/downloads/

[69] C. Jamroen, S. Sirisukprasert, and N. Hatti, “A study on SOC management of energy storage system for voltage regulation application in distribution network,” *International Renewable Energy Congress (IREC)*, Tunisia, 2020.

[70] S. Y. Yu, H. J. Kim, J. H. Kim, and B. M. Han, “SoC-based output voltage control for BESS with a lithium-ion battery in a stand-alone DC microgrid,” *Energies*, vol. 9, no. 11, p. 924, Nov. 2016.

[71] Eaton, “Application Guidelines,” [Online]. Available: https://www.eaton.com/content/dam/eaton/products/electronic-components/resources/technical/eaton-supercapacitor-application-guidelines.pdf

[72] Maxwell Technologies, “2.7V 3000F ultracapacitor cell,” BCAP3000 P270 K04/05 datasheet, 2022. [Online]. Available: https://maxwell.com/wp-content/uploads/2022/11/3003279-EN.3_DS_2.7V-3000F-Cell-BCAP3000-P270.pdf

[73] I. Zupan, V. Sunde, Z. Ban, and D. Kruselj, “Algorithm with temperature-dependent maximum charging current of a supercapacitor module in a tram regenerative braking system,” in *Journal of Energy Storage*, vol. 36, 2021.

[74] T. J. Tengku Hashim, A. Mohamed, and H. Shareef, “A review on voltage control methods

for active distribution networks," Przegląd Elektrotechniczny, pp. 304–312, 2012.

[75] R. Kabiri, D. G. Holmes, B. P. McGrath, and L. G. Meegahapola, "LV grid voltage regulation using transformer electronic tap changing, with PV inverter reactive power injection," *IEEE Journal of Emerging and Selected Topics in Power Electronics*, vol. 3, no. 4, pp. 1182-1192, Dec. 2015.

[76] O. Ceylan, A. Dimitrovski, M. Starke, and K. Tomsovic, "A novel approach for voltage control in electrical power distribution systems," *IEEE Power & Energy Society General Meeting*, 2018.

[77] K. P. Schneider et al., "A distributed power system control architecture for improved distribution system resiliency," *IEEE Access*, vol. 7, pp. 9957–9970, 2019.

[78] J. Haack et al., "VOLTTRON™: Using distributed control and sensing to integrate buildings and the grid," *IEEE 3rd World Forum on Internet of Things*, 2016.

[79] F. Ding et al., "Voltage support study of smart PV inverters on a high-photovoltaic penetration utility distribution feeder," *IEEE 43rd Photovoltaic Specialists Conference (PVSC)*, 2016, pp. 1375–1380.

[80] S. Kundu, S. Backhaus, and I. A. Hiskens, "Distributed control of reactive power from photovoltaic inverters," *IEEE International Symposium on Circuits and Systems (ISCAS)*, 2013, pp. 249–252.

[81] Y. Liu et al., "Modeling of marginal cost for PV inverter ancillary services considering inverter aging under transactive energy framework," *IEEE Power & Energy Society General Meeting*, 2020.

[82] S. Vlahinic, D. Frankovic, V. Komen, and A. Antonic, "Reactive power compensation with PV inverters for system loss reduction," *Energies*, vol. 12, no. 21, p. 4062, Oct. 2019.

[83] P. Saha, S. Dey, and M. Khanra, "Accurate estimation of state-of-charge of supercapacitor under uncertain leakage and open circuit voltage map," *Journal of Power Sources*, vol. 434, Sep. 2019.

[84] M. G. Villalva, J. R. Gazoli and E. R. Filho, "Modeling and circuit-based simulation of photovoltaic arrays," *Brazilian Power Electronics Conference*, Bonito-Mato Grosso do Sul, Brazil, 2009, pp. 1244-1254.

[85] MathWorks, "Implement PV array modules," June 2023. [Online]. Available: https://www.mathworks.com/help/sps/powersys/ref/pvarray.html

[86] Mathwork, “400-kW grid-connected PV farm (average model),” June 2023. [Online]. Available:https://www.mathworks.com/help/sps/ug/400-kw-grid-connected-pv-farm-average-model.html

[87] W. Wang, A. Beddard, M. Barnes, and O. Marjanovic, “Analysis of active power control for VSC–HVDC,” *IEEE Transactions on Power Delivery*, vol. 29, no. 4, pp. 1978-1988, Aug. 2014.

[88] J. D. Boles, “Battery energy storage emulation for power system applications.” Master’s Thesis, University of Tennessee, Knoxville, 2017.

[89] S. Wang, “Modeling and control of power electronics interfaced load for transmission power network analysis.” PhD dissertation, University of Tennessee, 2021.

[90] G. De Carne, A. Morandi, and S. Karrari, “Supercapacitor modeling for real-time simulation applications,” *IEEE Journal of Emerging and Selected Topics in Industrial Electronics*, vol. 3, no. 3, pp. 509–518, 2022.

[91] J. M. Miller, “Ultracapacitor modeling,” *Ultracapacitor Applications*, The Institution of Engineering and Technology, 2011, pp. 1–364.

[92] B. Pozo, J. Garate, S. Ferreiro, I. Fernandez, and E. Fernandez de Gorostiza, “Supercapacitor electro-mathematical and machine learning modelling for low power applications,” *Electronics*, vol. 7, no. 4, p. 44, Mar. 2018.

[93] V. Lystianingrum, B. Hredzak, V. G. Agelidis and V. S. Djanali, “On estimating instantaneous temperature of a supercapacitor string using an observer based on experimentally validated lumped thermal model,” *IEEE Transactions on Energy Conversion*, vol. 30, no. 4, pp. 1438-1448, Dec. 2015.

[94] S. Hamedi, T. Ghanbari, Z. Hosseini, E. Moshksar, “Self-discharge estimation of supercapacitor modules at different ventilation levels,” *Journal of Energy Storage*, vol. 52, 2022.

[95] X. Lin, H. Fu, H.E. Perez, J.B. Siege, A.G. Stefanopoulou, Y. Ding, M.P. Castanier, “Parameterization and observability analysis of scalable battery clusters for onboard thermal management,” *IFP Energies nouvelles International Conference*, 2013, pp. 165–178.

[96] A. Hijazi, P. Kreczanik, E. Bideaux, P. Venet, G. Clerc, and M. Di Loreto, “Thermal network model of supercapacitors stack,” *IEEE Transactions on Industrial Electronics*, vol.

59, no. 2, pp. 979-987, Feb. 2012.

[97] J. Wang, "Versatile three-phase power electronics converter based real-time load emulators." PhD dissertation, University of Tennessee, 2015.

[98] S. Hmam, J. C. Olivier, S. Bourguet, and L. Loron, "A multirate simulation method for large timescale systems applied for lifetime simulations," *IEEE Vehicle Power and Propulsion Conference (VPPC),* Montreal, QC, Canada, 2015.

[99] L. Wang, M. Li, and Z. Chen, "An energy management strategy for hybrid energy storage systems coordinate with state of thermal and power," *Control Engineering Practice*, vol. 122, May 2022.

[100] C. Tufon, A. Isemonger, B. Kirby, J. Kueck, and Fangxing Li, "A tariff for reactive power," *IEEE/PES Power Systems Conference and Exposition*, Seattle, WA, USA, 2009.

[101] R. O'Neill et al., "Principles for efficient and reliable reactive power supply and consumption," Department of Energy, Federal Energy Regulatory Commission, USA, FR Doc. E5-679, 2005.

[102] M. Alam, R. Melton, A. Somani, and T. McDermott, "Transactive approach for engaging distribution network assets for voltage management in southern California Edison distribution feeders," Pacific Northwest National Laboratory (PNNL), Richland, WA, USA, PNNL-27650, 2018.

[103] A. Safayet, P. Fajri, and I. Husain, "Reactive power management for overvoltage prevention at high PV penetration in a low-voltage distribution system," *IEEE Transactions on Industry Applications*, vol. 53, no. 6, pp. 5786–5794, 2017.

[104] X. Zhu *et al.*, "Voltage-load sensitivity matrix based demand response for voltage control in high solar penetration distribution feeders," *IEEE Power and Energy Society General Meeting*, 2018.

[105] R. Aghatehrani and R. Kavasseri, "Reactive power management of a DFIG wind system in microgrids based on voltage sensitivity analysis," *IEEE Transactions on Sustainable Energy*, vol. 2, no. 4, pp. 451–458, 2011.

[106] S. Leksawat *et al.*, "Decoupled voltage sensitivity analysis for decentralized smart grid operation," *International Symposium on Power Electronics, Electric Drives, Automation and Motion*, pp. 1184–1189, 2018.

[107] P. Kritprajun *et al.*, "VOLTTRON™ agent development for enabling reactive power

support of non-utility DERs by integrating transactive energy approach," *IEEE Power & Energy Society General Meeting (PESGM)*, Canada, 2020.

[108] H. Retty and J. S. Thorp, "Phasor measurement based voltage sensitivities for contingency analysis," *IEEE Power and Energy Society General Meeting*, September 2015.

[109] F. Tamp and P. Ciufo, "A sensitivity analysis toolkit for the simplification of MV distribution network voltage management," *IEEE Transactions on Smart Grid*, vol. 5, no. 2, pp. 559–568, 2014.

[110] J. Zhao, D. Shi, R. Sharma, and C. Wang, "Microgrid reactive power management during and subsequent to islanding process," *IEEE PES T&D Conference and Exposition*, USA, 2014.

[111] The California Energy Commission (CEC), "Inverter performance test summaries," June 2021. [Online]. Available: https://www.gosolarcalifornia.ca.gov/

[112] IEEE PES AMPS DSAS Test Feeder Working Group, "Test feeders," June 2021. [Online]. Available: https://site.ieee.org/pes-testfeeders/resources/

[113] D. Das, G. Gurrala, and U. Jayachandra Shenoy, "Linear quadratic regulator-based bumpless transfer in microgrids," *IEEE Trans. Smart Grid*, vol. 9, no. 1, pp. 416–425, Jan. 2018.

[114] M. Ganjian-Aboukheili, M. Shahabi, Q. Shafiee, and J. M. Guerrero, "Linear quadratic regulator based smooth transition between microgrid operation modes," *IEEE Trans. Smart Grid*, vol. 12, no. 6, Nov. 2021.

[115] K. J. Astrom and R. M. Murray, Feedback Systems: An introduction for scientists and engineers. New Jersey: Princeton University Press, 2008.

[116] F. Yang, L. Yang, and X. Ma, "An advanced control strategy of PV system for low-voltage ride-through capability enhancement," *Sol. Energy*, vol. 109, pp. 24-35, 2014.

[117] Y. Tan *et al.*, "Enhanced frequency regulation using multilevel energy storage in remote area power supply systems," *IEEE Transactions on Power Systems*, vol. 34, no. 1, pp. 163–170, Jan. 2019.

[118] S. Karrari, H. R. Baghaee, G. D. Carne, M. Noe, and J. Geisbuesch, "Adaptive inertia emulation control for highspeed flywheel energy storage systems," *IET Generation, Transmission & Distribution*, vol. 14, no. 22, pp. 5047–5059, Nov. 2020.

[119] J. Zhang, M. Gu, and X. Chen, "Supercapacitors for renewable energy applications: A

review," *Micro and Nano Engineering*, vol. 21, Dec. 2023.

[120] M. Catelani *et al*., "Experimental characterization of hybrid supercapacitor under different operating conditions using EIS measurements," *IEEE Transactions on Instrumentation and Measurement*, vol. 73, pp. 1-10, 2024.

[121] F. Corti *et al.*, "Time-domain circuit modelling for hybrid supercapacitors," *Energies*, vol. 14, no. 20, 2021.

Vita

Paychuda Kritprajun received the B.S. degree in electrical engineering from the King Mongkut's Institute of Technology Ladkrabang, Thailand, in 2014, and the M.S. degree in 2020 in electrical engineering from the University of Tennessee, Knoxville, TN, USA, where she is currently working toward the Ph.D. degree. She was a Design Engineer with Nissan Motor Asia Pacific Co., Ltd., Thailand, in 2014 and an Electrical Engineer with Provincial Electricity Authority (PEA), Thailand, during 2015–2018. Her research interests include energy storage systems, PV systems, renewable energy integration, and microgrids.